# CONVECTIVE HEAT TRANSFER SCALING AT THE WALL OF CIRCULATING FLUIDIZED BED RISERS

A Dissertation
Presented to the Faculty of the Graduate School
of Cornell University
in Partial Fulfillment of the Requirements for the Degree of
Doctor of Philosophy

by
Anna Elizabeth Griffith
May 2000

# CONVECTIVE HEAT TRANSFER SCALING AT THE WALL OF CIRCULATING FLUIDIZED BED RISERS

Anna Elizabeth Griffith, Ph.D.
Cornell University 2000

In this study, we examine the convective heat transfer scaling of moderately pressurized Circulating Fluidized Beds (CFB) using a single cold laboratory facility. By recycling fluidization gas mixtures of adjustable density, the experiments simulate the hydrodynamics of a combustor burning coal under a pressure of 0.64 MPa. While matching the hydrodynamics in the upper riser using Glicksman's (1993) reduced set of dimensionless numbers, we vary thermal properties of the flow and measure the effect on the convective heat transfer coefficient at the wall.

In CFB flows, the suspension partly condenses into denser clusters separated from the wall by a thin gas film of order the mean particle diameter (Glicksman, 1997). The clusters generally dominate the convective heat exchange with the wall because of their relatively high solid volume fractions and heat capacity. Accordingly, Lints and Glicksman (1993) suggested that the rate of heat transfer to the wall scales with the mean time spent by individual clusters there.

For this reason, we focus on the hydrodynamics of the cluster motion at the wall. We present a scaling of cluster velocity based on a comparison of measurements from other investigators. A novel thermal marking technique records the residence length of clusters at the wall and leads to a suggested scaling of cluster residence length.

A unique, non-intrusive probe positioned at the wall of our facility measures simultaneously the solid concentration and instantaneous heat transfer coefficient. The heat transfer sensor has a 25 ms response that is at least twice as rapid as those described by previous investigators. The fraction of the wall covered by clusters and the cluster solid volume fraction are also extracted from solid concentration measurements. Guard heaters reduce conduction losses from the probe and assist thermal development of the flow, allowing a measurement of convective heat transfer coefficient that is more representative of large surface-area combustors. Finally, we present a scaling of the Nusselt Number as a function of relevant thermal and hydrodynamic parameters of the flow.

# BIOGRAPHICAL SKETCH

The author graduated from Gaston High School in Oregon, then attended Wellesley College to earn her B.A. in Physics. While at Wellesley, she studied Russian language, anthropology and math, while taking mechanical engineering and math classes at MIT. An undergraduate research experience in the Fluid Mechanics Lab of the Mechanical Engineering Department at MIT under Professor Harri Kytömaa impressed her and opened her eyes to the possibilities of using engineering to solve real-world problems.

She then sought a practical research problem for her Ph.D. She began graduate studies at Cornell in 1994, in fluid mechanics, heat transfer, multiphase flows, and electrical engineering. The heat transfer scaling for CFBs project allowed her to develop her experimental tools and gain experience with heat transfer problems.

Upon graduation, she will work at Intel Corporation, in Phoenix, Arizona, focusing on heat dissipation problems for their next-generation chips.

*For my mom,*

*whose hard work has always been an inspiration to me.*

# ACKNOWLEDGMENTS

I would first like to thank my advisor, Prof. Michel Y. Louge, for providing expert insight into the art of conducting experiments. I am grateful to him for guiding me through developing useful methods for measurement, analysis, and writing.

I owe much thanks to Prof. Kenneth Torrance for his encouragement and his technical input. His personable nature and gift for communicating ideas added to my overall experience.

Genuine appreciation is extended to Prof. Clifford Pollock, whom I admire for the ability to impart physical intuition for waveguides to those of us previously lacking EE backgrounds.

The funding for my studies has been generously provided by a National Science Foundation Graduate Fellowship, number GER-9253848. Additional support from a Cornell Sage Fellowship is also appreciated.

I would like to acknowledge the timely and useful input of Vincent Perna, who helped to make my text readable and consistent. Also, my mother's contributions to portions of the text were invaluable and much appreciated.

Thanks are extended to Dr. Vincent Bricout, Stéphane Martin-Letellier and Steve Keast for contributing to the experimental work.

Two undergraduates who participated in my project showed exceptional promise as future researchers or teachers: Margaret Middleton, for her precise work with my signal analysis, and Samuel

Vonderheide, for his truly professional quality in all of the drawings leading up to the final form of Figure 4.1.

I would like to say thanks to those kind people who got me started on the right foot at Cornell: Dr. Gorti Sarma, Dr. Vivek Bhatt, and Dr. Tom Dreeben. And to those who made my stay pleasurable: Wendy Foels, Tina Jayaweera and Mark McDonald, Manoel Nogueira, Prof. Van derMeulen, Brenda Irving-Bryant, Laurie Patten, Nanette Peterson, Rick Schmidt and Ed Jordan, and the most helpful shop guys that I will definitely miss at Intel: Tom, Paul, George and Leo. (Paul, I owe you one.)

To those people who comprised my home away from home, my officemates: Keith, Dan, Doug, Mike, Jitendra and Bill. I will miss all of you. Hopefully the real world won't have too much effect on you guys after graduation! But I'm sure I'll miss the insanity. Let's stay in touch and meet for mini-reunions!

To MC for his continual friendship, support and encouragement.

To my entire family for being patient with me during this time.

A special thanks to Jane and Wayne, whose happy home is my favorite place to visit. The continuous support and inspiration provided by my mom and Jane & Wayne made my academic achievement possible.

# TABLE OF CONTENTS

# LIST OF TABLES

# LIST OF FIGURES

# LIST OF ABBREVIATIONS

| | |
|---|---|
| ACFB | Circulating Fluidized Bed operating near atmospheric pressure |
| ASTM | American Society for Testing and Materials |
| CFB | Circulating Fluidized Bed |
| FCC | Fluid Catalytic Cracking |
| PCFB | Circulating Fluidized Bed operating under pressurized conditions |
| PDF | Probability Density Function |
| PSD | Particle Size Distribution of solid inventory |
| S/N | signal to noise ratio |
| SS | Stainless Steel |
| TCD | Thermal Conductivity Detector |

# LIST OF SYMBOLS

| | |
|---|---|
| $A$ | exposed surface area of the heat transfer probe face ($m^2$) |
| $A_p$ | surface area of a single particle in the flow ($m^2$) |
| $Ar$ | Archimedes Number = $\rho_s \rho d^3 g/\mu^2$ |
| $Bi$ | Biot number = $hd/k_s$ |
| $C$ | capacitance between the ground and sensing surface (F) |
| $C_D$ | drag coefficient for a single spherical particle |
| $C_0$ | capacitance between the ground and sensing surface in air (F) |
| $c_p$ | specific heat of the solid material (J / (kg K)) |
| $c_f$ | specific heat of the gas mixture (J / (kg K)) |
| $d$ | hydrodynamic diameter (m) |
| $d^*$ | diameter for correlation by Haider and Levenspiel |
| $d_i$ | mean diameter in sieve i (m) |
| $d_p$ | mean Sauter diameter (m) |
| $d_{sph}$ | sphere diameter (m) |
| $E$ | Young's modulus for the solid material (Pa) |
| $E_0$ | output voltage from anemometer bridge circuit (V) |
| $E_w$ | voltage across heat transfer probe (V) |
| $F$ | 1-D flux of clusters arriving at the wall ( 1/ (m s)) |
| $F_D$ | drag force per unit volume of suspension exerted by the gas on the solids ($N/m^3$) |
| $f$ | fraction of heated clusters measured at the probe |

| | |
|---|---|
| $f_h$ | fraction of the wall covered by clusters |
| Fr | Froude Number = $U_0/(gd)^{1/2}$ |
| $f_r$ | PDF of residence lengths of clusters |
| G | adjustable amplifier gain |
| g | gravity ($m/s^2$) |
| $G_s$ | solid flux |
| h | heat transfer coefficient at the wall of the CFB ($W/(m^2K)$) |
| H | riser height (m) |
| $\hat{h}$ | measured ’instrument estimate’ of heat transfer coefficient ($W/(m^2K)$) |
| $\overline{h}$ | measured, time-averaged ’instrument estimate’ of heat transfer coefficient ($W/(m^2K)$) |
| $h_g$ | dilute phase heat transfer coefficient ($W/(m^2K)$) |
| $h_H$ | time-mean heat transfer coefficient for a cluster at the CFB wall ($W/(m^2K)$) |
| $h_{overall}$ | heat transfer coefficient for the continuum model ($W/(m^2K)$) |
| $h_{pc}$ | heat transfer coefficient for particle convection model ($W/(m^2K)$) |
| $h_w$ | heat transfer coefficient associated with conduction through the gas gap ($W/(m^2K)$) |
| I | electrical current through the heat transfer probe (A) |
| k | thermal conductivity of the gas (W/mK) |
| K | amplifier gain |
| $K_0$ | modified Bessel function |
| $K_1$ | modified Bessel function |

| | |
|---|---|
| $k_a$ | thermal conductivity of Aluminum riser (W/(mK)) |
| $k_D$ | thermal conductivity of the Delrin lip (W/(mK)) |
| $k_e$ | effective thermal conductivity of the emulsion at the wall (W/(mK)) |
| $K_{eff}$ | effective dielectric constant of the suspension |
| $K_h$ | dielectric constant of the host fluid |
| $K_p$ | dielectric constant of the solid |
| $k_s$ | thermal conductivity of the solid material (W/(mK)) |
| L | ratio of riser diameter to particle diameter |
| $\ell$ | residence length of clusters (random variable) (m) |
| $L_0$ | nominal spacing between the thermocouple sensor and the lower edge of the heaters (m) |
| $L_{eff}$ | effective inductance of heat transfer probe (H) |
| $L_v$ | variable inductance in anemometer bridge circuit (H) |
| M | Solid Loading = $G_s/\rho U_0$ |
| $M_1$ | radial coordinate for Bessel function |
| $M_2$ | constant in the correlation by Gelperin and Einstein |
| $Nu_d$ | Nusselt Number based on particle diameter =hd/k |
| P | electrical power supplied to the probe (W) |
| Pr | Prandtl number of gas = $\mu c_f/k$ |
| q | power dissipated by modified hot wire sensor (W) |
| $Q_s$ | capacitance system constant |
| $q_w$ | power supplied to the guard heaters (W) |
| R | ratio of solid to gas density |

| | |
|---|---|
| $R$ | resistance of sensor (modified hot wire coil) ($\Omega$) |
| $R_0$ | resistance of sensor (modified hot wire coil) at 0 C ($\Omega$) |
| $R_D$ | thermal resistance of the Delrin cylinder |
| $R_1$ | resistor 1 in anemometer bridge circuit ($\Omega$) |
| $R_2$ | resistor 2 in anemometer bridge circuit ($\Omega$) |
| $R_3$ | resistor 3 in anemometer bridge circuit ($\Omega$) |
| $R_b$ | coil resistance evaluated at the suspension temperature ($\Omega$) |
| $R_c$ | heat transfer probe's cable resistance ($\Omega$) |
| $Re$ | Reynolds Number based on CFB diameter = $\rho U_0 D/\mu$ |
| $Re_d$ | Reynolds number based on slip velocity and hydrodynamic particle diameter = $\rho U_{slip} d/\mu$ |
| $Re_s$ | Reynolds number based on slip velocity and mean Sauter diameter = $\rho U_{slip} d_p/\mu$ |
| $R_f$ | thermal resistance of the riser wall |
| $R_f$ | fin resistance |
| $r_i$ | inner radius of the Delrin lip (m) |
| $r_o$ | outer radius of the Delrin lip (m) |
| $R_x$ | thermal resistance through the coil base and probe stem |
| $T$ | heat transfer probe face temperature, equal to coil temperature (°C) |
| $t$ | time (s) |
| $T_b$ | suspension temperature (°C) |
| $T_0$ | reference temperature (0 °C) |
| $T_p$ | particle temperature (°C) |

| | |
|---|---|
| $T_w$ | temperature of the CFB wall (°C) |
| $u^*$ | velocity for correlation by Haider and Levenspiel |
| $U_0$ | superficial gas velocity in riser<br>= (volumetric flow rate of gas)/(cross-sectional area of riser) (m/s) |
| $U_{cl}$ | particulate cluster velocity near the CFB wall (m/s) |
| $U_t$ | terminal velocity of a single particle in the gas (m/s) |
| $V$ | capacitance sensor amplitude voltage (V) |
| $v_r$ | relative velocity of particles at collision impact (m/s) |
| $V_0$ | capacitance sensor amplitude voltage in air (V) |
| $x$ | percentage by mole of $SF_6/CO_2$ in $SF_6/CO_2/He$ mixture |
| $x_i$ | weight fraction in sieve i |
| $z$ | vertical coordinate along axis of riser, pointing up (m) |
| $\beta$ | constant for guard heaters |
| $\Gamma$ | constant with units of length (m) |
| $\delta$ | gap thickness between wall and cluster made dimensionless by particle diameter |
| $\Delta$ | coil thickness along probe axis (m) |
| $\Delta_c$ | $3(1-\sigma_p)^2/2E$ |
| $\Delta h$ | axial distance between solid flux measurement points along the riser (m) |
| $\varepsilon$ | voidage fraction of the suspension |
| $\varepsilon_f$ | fin effectiveness |
| $\lambda$ | residence length of cluster traveling near the wall (m) |

| | |
|---|---|
| $T_w$ | temperature of the CFB wall (°C) |
| $u^*$ | velocity for correlation by Haider and Levenspiel |
| $U_0$ | superficial gas velocity in riser<br>= (volumetric flow rate of gas)/(cross-sectional area of riser) (m/s) |
| $U_{cl}$ | particulate cluster velocity near the CFB wall (m/s) |
| $U_t$ | terminal velocity of a single particle in the gas (m/s) |
| $V$ | capacitance sensor amplitude voltage (V) |
| $v_r$ | relative velocity of particles at collision impact (m/s) |
| $V_0$ | capacitance sensor amplitude voltage in air (V) |
| $x$ | percentage by mole of $SF_6/CO_2$ in $SF_6/CO_2/He$ mixture |
| $x_i$ | weight fraction in sieve i |
| $z$ | vertical coordinate along axis of riser, pointing up (m) |
| $\beta$ | constant for guard heaters |
| $\Gamma$ | constant with units of length (m) |
| $\delta$ | gap thickness between wall and cluster made dimensionless by particle diameter |
| $\Delta$ | coil thickness along probe axis (m) |
| $\Delta_c$ | $3(1-\sigma_p)^2/2E$ |
| $\Delta h$ | axial distance between solid flux measurement points along the riser (m) |
| $\varepsilon$ | voidage fraction of the suspension |
| $\varepsilon_f$ | fin effectiveness |
| $\lambda$ | residence length of cluster traveling near the wall (m) |

| | |
|---|---|
| $\mu$ | gas viscosity ($Ns/m^2$) |
| $\nu$ | solid volume fraction of the suspension |
| $\overline{\upsilon}$ | cross-sectionally averaged solid fraction of the suspension |
| $\overline{\upsilon}_w$ | time-averaged local solid fraction measured at the wall |
| $\nu_c$ | average solid volume fraction of the cluster |
| $\rho$ | gas density ($kg/m^3$) |
| $\rho_s$ | solid density ($kg/m^3$) |
| $\rho_{susp}$ | cross-sectionally averaged suspension density at a given elevation ($kg/m^3$) |
| $\sigma$ | temperature coefficient of resistance for Platinum (1/ °C) |
| $\sigma_p$ | Poisson's ratio for the solid material |
| $\tau_c$ | average residence time of a cluster at the wall, averaged over number of clusters (s) |
| $\tau_{coll}$ | estimated collision time (s) |
| $\tau_e$ | thermal equilibration time for conduction through the area of contact between solids (s) |
| $\tau_p$ | cooling time of a single particle conducting heat through a gas gap at the CFB wall (s) |
| $\phi$ | particle sphericity |

# CHAPTER ONE:
# INTRODUCTION

## *1.1 Introduction to Circulating Fluidized Beds*

Fluidization of solid fuel for efficient combustion and reaction processes has been used for most of this century. It consists of entraining fuel particles with a flowing gas, thus improving contact between the fuel and oxidizer. Figure 1.1 illustrates the levitating effect caused by progressively increasing gas velocity through a bed of particles. As the gas flow rate increases, a dynamic segregation of particles causes the bed to appear to move as a fluid. Once the gas velocity is increased past that for the slugging regime, there is no longer a clear delineation of the top of the bed. The suspension is not static, but in fact circulates with a relatively dilute ascending core, and a significant downflow of recirculating particles near the wall.

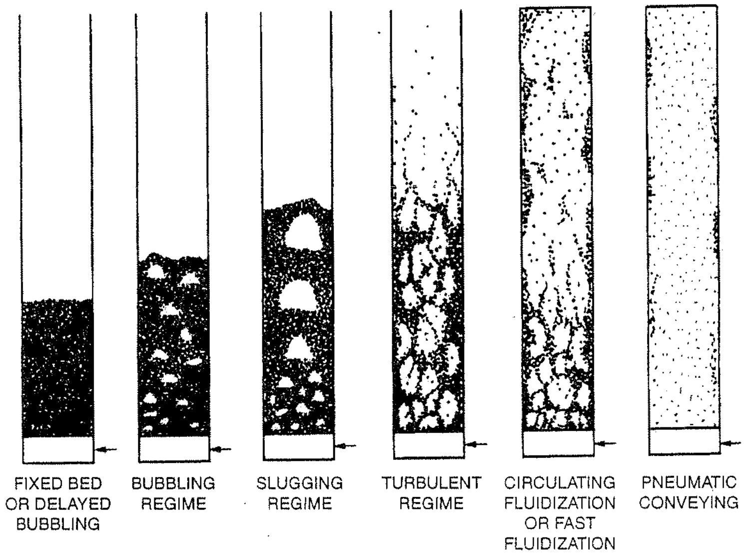

Figure 1.1. Regimes of fluidization (Grace, 1986).

The circulating fluidization regime helps to promote gas-solid mixing, while particle motion enhances the turbulent fluctuations of the gas. A common purpose of exothermic industrial processes that involve gases and solid particles is to transfer heat efficiently from the reaction to the vessel walls. Circulating fluidization facilities are an efficient combustion method for utility-scale atmospheric pressure units (Brereton, 1997). Circulating Fluidized Bed (CFB) reactors have been used in the last three decades (Brereton, 1997) for Fluid Catalytic Cracking (FCC) processes in petroleum refineries and for CFB combustors used to burn coal to generate electrical power. But the construction of industrial CFB facilities is expensive and can increase rapidly with the required combustor diameter. This project focuses on developing methods for predicting convective heat transfer rates from the suspension to the wall of the CFB. In this thesis, we will describe scaling laws for heat transfer, experimental support of these models, and novel instrumentation.

### *1.1.1 CFB Combustors in Power Generations Systems*

Figure 1.2 shows a power generation system that uses a typical CFB combustor as a boiler to produce steam. Coal and limestone are fed into the base of the combustor where they are fluidized by air. As the primary means of generating steam to drive turbines, heat from the burning fuel is transferred to the waterwalls of the combustor.

Two additional heat transfer paths are typically employed to increase the power obtained from the cycle. Before showing the actual facility configurations, however, we review the associated thermodynamic cycle descriptions.

Thermodynamic cycles of the water as the working fluid are shown in Figures 1.3 (a) and (b) on temperature-specific entropy axes. Figure 1.3 shows the ideal Rankine cycle with superheat and reheat, respectively. Entropy is produced from irreversibilities in real processes. Following a procedure similar to the ideal Rankine cycle analysis (Bejan, 1997), for this basic qualitative description, we treat the flows through the turbine and compressor as isentropic, so that the compressor and turbine steps are represented in Figure 1.3 as the left and right vertical lines, respectively.

The first additional path for transferring heat to the steam is to utilize the heat from exiting gases. Hot flue gases leaving the combustor are separated from coal particles in a hot cyclone and then continue to a superheater. The superheater provides a surface for heat transfer from the hot exiting gas to the steam. This heat transfer may be as much as one quarter of the heat obtained directly from the boiler walls (Leon and McCoy, 1986). In this way, the superheater increases the net power obtained in the steam cycle.

To further increase the extracted power from the cycle, another heat transfer surface is employed to heat the steam. Figure 1.4 shows a configuration with a Fluidized Bed Heat Exchanger that transfers heat from the hot particles leaving the cyclone to its embedded steam tubes. This process serves to "reheat" the steam in preparation for a pass through a second turbine, as shown in Figure 1.3(b). Thus, heat from the CFB combustion process is utilized to generate steam in power plants.

A recent trend in coal combustion has been to run CFBs under pressure. Pressurized Circulating Fluidized Beds (PCFBs) operate at elevated temperatures (1200 K) and under pressures on the order of 10 atmospheres, to keep the overall process efficiency high. By coupling the combustor to a gas turbine, the PCFB system has a greater process efficiency and produces relatively clean electricity for a lower cost than conventional boilers.

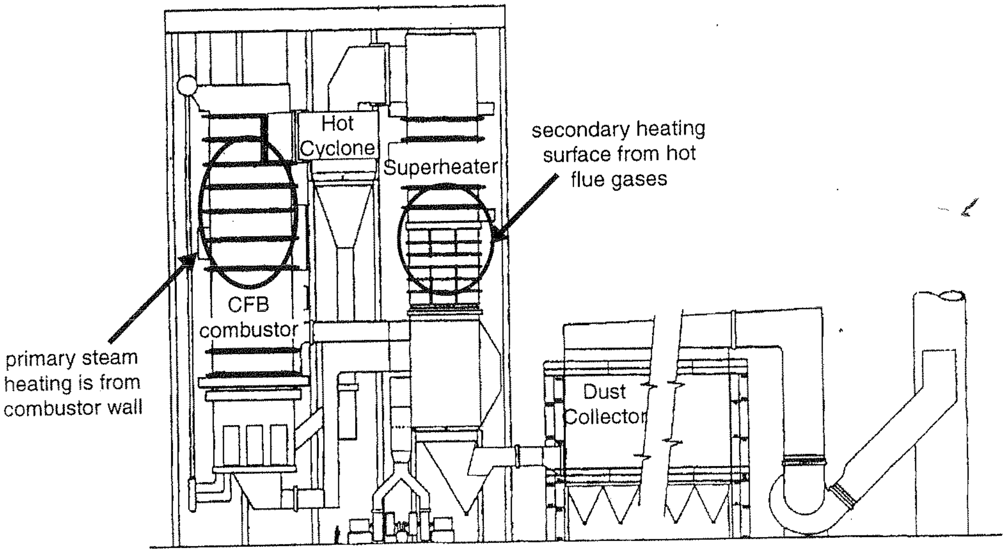

Figure 1.2. Components of a utility size CFB combustion boiler. (Nova Scotia Power Corporation, 150 MW (e) single reheat turbine generator, 1986).

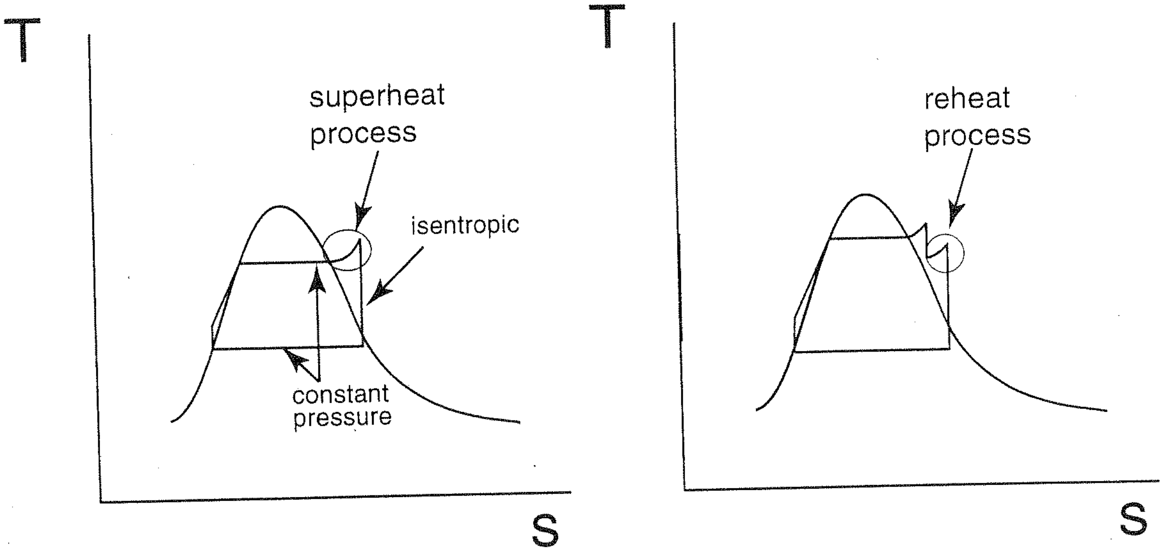

Figure 1.3. Temperature versus specific entropy diagrams for steam power cycles with superheat (a) and reheat (b).

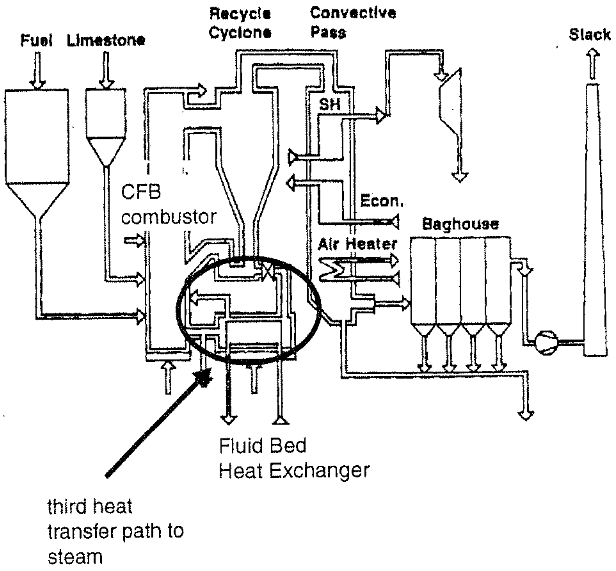

Figure 1.4. Steam generator process flow diagram with optional Fluid Bed Heat Exchanger as a "reheat surface" for the steam (Lurgi/CE, 1986).

The primary means of extracting power from these facilities is by heat transfer from within the combustor to the waterwalls. In this study, we focus on improving methods for predicting convective heat transfer rates from the suspension to the waterwalls, see Section 1.3 for details. This should help to reduce costs by providing better estimates of required combustor diameters.

### *1.1.2 Background*

In CFB combustors, heat flows from the hot suspension to the waterwalls. The convective heat transfer rate q can be written as

$$q = hA(T_b - T_w) , \tag{1.1}$$

where h is the convective heat transfer coefficient, A is the wall surface area and $T_b$ and $T_w$ are the bed suspension and wall temperatures, respectively. The coefficient h is a convenient engineering quantity that relates the heat flux to the driving temperature difference.

Many investigators had measured heat transfer coefficients at the wall of CFB risers. However, comparisons of heat transfer coefficients among researchers revealed differences that at first could not be reconciled. The most profound differences were between two classes of measurements: industrial plants versus small scale models. Industrial plants typically had extensive heated surface areas and large bed diameters whereas laboratory models used point sensors and small bed diameters. These differences led to a search for the underlying mechanisms that affect the heat transfer rates. From subsequent experiments it was found that there were at least three factors strongly influencing the magnitude of the heat transfer coefficient:

- bed diameter,
- sensor size or heated surface size, and
- material combinations and operating conditions.

Scaling laws are required to extrapolate heat transfer coefficients measured in a small-scale model to those in an industrial-size facility. To derive such scaling laws, scientists have focused on two aspects of CFB heat transfer (Lints and Glicksman, 1993).

The first examines the convection process alone (Fang et al., 1995; Wu et al., 1989), while the second studies radiation effects (Wu et al., 1989b). Although at high temperatures the combined effect of convection and radiation heat transfer is not simply a linear addition of these two modes, this decomposition of the problem has been widely accepted as a necessary first step. In this context, one purpose of the present study is to investigate the scaling of convective heat transfer at the CFB wall, see Section 1.3.

### *1.1.3 Hydrodynamic Scaling*

Extensive hydrodynamic scaling has been used and proven by several investigators (Glicksman, 1984; Glicksman et al., 1991; Chang and Louge, 1992). Scaling, as referred to in this thesis, aims to achieve similarity of the fluid dynamic properties, including those that are readily measurable such as axial static pressure profiles and radial solid concentration profiles.

In order to compare the hydrodynamics between facilities of differing physical dimensions, studies have shown (Chang and Louge, 1992) that it is necessary first to non-dimensionalize the equations governing the flow parameters. The latter include gas and solid densities, gravity, gas viscosity, particle and bed diameter, and the operating conditions gas velocity and solid flux. This process yields five dimensionless numbers that completely characterize the hydrodynamics of facilities of any size. For example, the ratio of bed to particle diameter is a measure of the scale of the facility. The development of these scaling laws and the pertinent literature review is described in detail in Chapter Two. In this study, we employ these scaling laws to maintain the hydrodynamics fixed among heat transfer experiments with varying solids, gases and operating conditions.

## *1.2 CFB Convective Heat Transfer Literature Review*

In the bubbling bed flow regime, the suspension is in direct contact with the water-cooled walls. In this case, Mickley and Fairbanks (1955) modeled the heat transfer to particle clusters at the wall as a transient diffusion process into a homogeneous semi-infinite medium. They calculated a time-averaged value of the heat transfer coefficient to characterize the heat transfer rate to the wall.

The flow structure in CFBs is much more complex than it is in the fixed or bubbling regimes. Incoming particles are fluidized by upflowing gases in the core and eventually carried out of the top of the riser. Effects such as pressure gradients and/or turbulent velocity fluctuations cause most of the particles to aggregate into clusters. These cluster formations reduce the drag force on individual particles, as described by the correlation for drag coefficient by Foscolo and Gibilaro (1984). Temporal and spatial fluctuations in velocity and solid volume fraction often accompany the ejection of clusters to the wall, where they fall a given distance, often within one particle diameter of the wall, until they travel back to the core. The portion of the riser wall that is not covered by clusters is in contact with a relatively dilute flow of particles. In an actual CFB combustor, heat is generated inside the riser and transported by relatively hot particulate clusters into the thermal boundary layer at the wall.

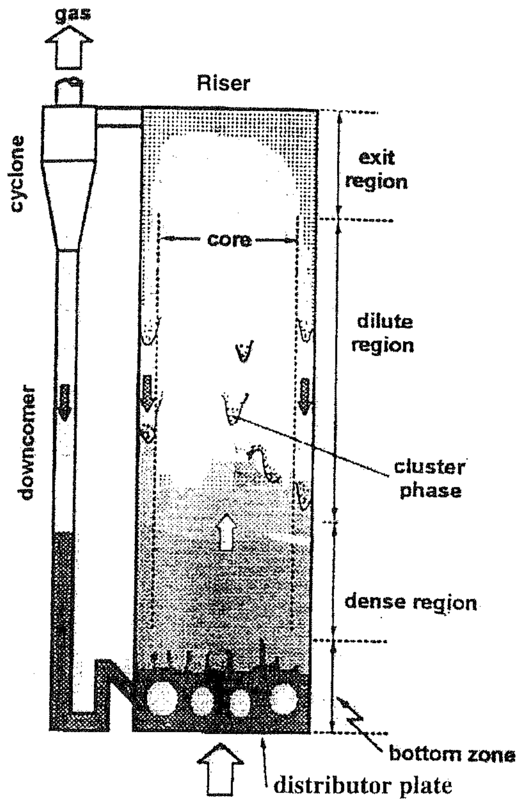

Figure 1.5. Typical flow structure in a CFB combustor.

Another important aspect of CFB heat transfer is related to the development of thermal boundary layers at the wall. Because most of their wall surface is in contact with a thermally fully developed boundary layer, industrial facilities exhibit a constant heat transfer coefficient as a function of riser elevation. In contrast, laboratory facilities must provide a heated length sufficient for thermal boundary layer development. One way to do this is to wrap the riser wall with heaters. This technique allows for a measurement of thermally fully developed heat transfer coefficient at the wall.

Among investigators that are currently engaged in CFB heat transfer research (Noymer, 1997; Kobro and Brereton, 1986; Basu and

Nag, 1987; Wu et al., 1987; Glicksman, 1997; Wu et al., 1989; Bi et al. 1991), it is generally agreed that:

- heat transfer decreases for larger active heat transfer surface areas,
- it increases with increasing cross-sectionally averaged solid fraction, and
- it increases with decreasing particle diameter.

However, this qualitative understanding does not provide a scaling for convective heat transfer rates.

Glicksman (1997; Lints and Glicksman, 1993) has emphasized the importance of a particle convection heat transfer process in CFBs. In this process, hot particulate clusters from the core carry heat to the walls by self-diffusion and then transfer their heat through a thin gas layer to the wall. Figure 1.6 illustrates the concept of heat transfer by particle convection. Two important time scales for this process are the residence time of the cluster at the wall, $\tau_c$, and the time for a particle to cool at the wall, $\tau_p$. Then the ratio of these parameters is a measure of the propensity for clusters to transfer their heat to the wall.

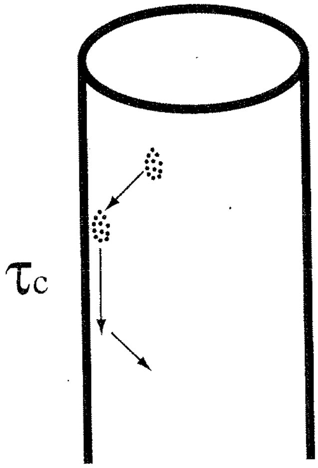

Figure 1.6. Diagram of particle convection heat transfer with the cluster residence time at the wall given by $\tau_c$.

However, the complexity of the flow structure at the CFB wall (see Figure 1.5), requires a more sophisticated model. Lints and Glicksman (1993) proposed a phenomenological model incorporating the effect of the dynamic structure into the heat transfer modeling. Their model uses five parameters, the first three of which they fit empirically in terms of the cross-sectional average solid fraction, $\overline{\upsilon}$. The first is the fraction of the wall covered by clusters, $f_h$. The second is the dimensionless gas layer thickness, $\delta$, based on particle diameter. The third is the cluster solid volume fraction, $\nu_c$. The fourth is the residence time of a cluster at the wall $\tau_c$, which is the ratio of the residence length $\lambda$ and the cluster velocity $U_{cl}$. Wu et al. (1991) correlated $\lambda$ as a function of $\overline{\upsilon}$, and the cluster velocity is usually about 1 m/s according to a recent review by Glicksman (1997). The final parameter is the dilute phase heat transfer coefficient at the wall, $h_g$, which is often approximated by single phase correlations.

Lints and Glicksman (1993) proposed a mechanistic model to predict convective heat transfer rates based on these five parameters. However, using this model is difficult since the five parameters have not been scaled versus independent variables (Glicksman, 1997). In a recent review, Glicksman (1997) emphasized that although many heat transfer rates have been measured in laboratory-scale plants, it is still unclear how the heat transfer rate to the walls increases with reactor diameter in actual facilities.

The correlations for these parameters are useful for existing facilities where the cross-sectionally averaged solid concentration $\overline{\upsilon}$ can be measured directly. However, these correlations do not shed light on what the heat transfer rates will be for new facilities, or on the relation between small-scale models and full-scale plants.

Currently, investigators are seeking a dimensionless number for the heat transfer scaling. Once the geometry, hydrodynamics and new dimensionless heat transfer number are matched, full similarity between the laboratory model and industrial facility will be achieved.

### *1.3 Project Objectives*

Our project is concerned with scaling convective heat transfer rates from the suspension to the CFB wall and with developing useful instrumentation. Its objectives were:

- to develop a predictive model of the convective heat transfer coefficient at the wall by seeking scalings for the input parameters of the phenomenological model by Lints and

Glicksman (1993), keeping in mind that dependences on independent parameters of the flow are particularly useful;

- to use Cornell's CFB facility with its unique capability for recirculating fluidization gases to maintain the hydrodynamics fixed using proven scaling laws, while varying thermal parameters of the flow and measuring the resulting heat transfer coefficient;
- to conduct a literature review of CFB measurements and find a scaling for phenomena relevant to convective heat transfer at the wall;
- to calibrate and use a new combination probe to measure simultaneously and non-invasively the heat transfer coefficient and solid volume fraction at the wall, with a technique incorporating
  - increased accuracy of the solid volume fraction measurement due to capacitive guarding,
  - constant temperature operation of the heat transfer sensor that provides a faster response for the time-dependent heat transfer coefficient measurement,
  - accounting of conduction losses from the input power to the probe, providing a means for more accurate measurement of the convective heat transfer coefficient than previous measurements, and
  - guard heaters allowing the measurement of a thermally developed convective heat transfer coefficient at the wall,

and reducing the thermal inertia of the sensor and power losses from the heat transfer probe due to conduction;

- to develop a new procedure for measuring the residence length of clusters at the wall, including the construction of a thermocouple-capacitance probe, the development of a technique for operation of this system during CFB experiments, and the derivation of a new analysis for the extraction of the cluster residence length from the data; and
- to seek dependencies of the heat transfer coefficient on independent and measured dynamic properties of the flow.

### *1.3.1 Outline of the Thesis*

Chapter Two includes a new scaling of cluster velocity at the CFB wall based on published results of recent measurements. Chapter Three describes our scaled-down CFB facility at Cornell and the strategy of experiments used in this study.

Chapter Four describes a new diagnostic for non-invasive, instantaneous local measurements of the convective heat transfer coefficient and solid fraction at the wall. Because our method employs over one meter of manually controlled guard heaters at the wall to create a constant temperature wall section, it eliminates artificially high values of the heat transfer coefficient due to thermally undeveloped flow. The use of guard heaters also minimizes conduction losses from the probe. The constant temperature wall section helps to reduce thermal inertia of the sensor. Finally, careful accounting of the conduction losses from the instrument provides a heat transfer coefficient that is representative of convective heat transfer only.

Chapter Four also describes a new technique for the measurement of the residence length of clusters at the wall. We use a thermal marking concept similar to that employed by Noymer (1997). However, in our study, we develop a new analysis procedure that includes a Probability Distribution Function representative of the cluster residence length at the wall. Our results yield a new scaling of cluster residence length as a function of independent parameters.

Chapter Five presents measurements of the local, dimensionless convective heat transfer coefficient as a function of dynamic and thermal properties of the flow. In Chapter Six we conclude that the heat transfer coefficient at the wall should indeed be made dimensionless by particle diameter. We find a central dependence of the dimensionless convective heat transfer coefficient at the CFB wall on our measured and scaled values of the fractional wall coverage multiplied by the square root of the product of the cluster solid fraction and the ratio of time constants.

# CHAPTER TWO:
# SCALING

In the previous chapter, we introduced the principle of circulating fluidized beds (CFBs), provided background information and a brief literature review on the subject, and stated the objectives of the present research. We now proceed to describe scalings of the hydrodynamics (Section 2.1) and to expand the literature review and discuss current methods for predicting the convective heat transfer coefficient.

While the scale-up of fluidized beds from a laboratory model or a prototype to a commercial unit is relatively well understood (Yates, 1996), the scaling of CFBs is more complex in part because of the variety of possible operating regimes (Geldart and Rhodes, 1986). Also, most scale-up studies have been conducted for CFBs operating near atmospheric pressure (ACFBs).

The expense of building a new CFB facility increases rapidly with combustor diameter. Since the required rate of heat transfer to the waterwalls dictates the size of a new combustor, improved understanding of heat transfer scaling reduces the uncertainty in required diameter, thereby minimizing over-engineering and the total cost.

For gas-solid suspensions, as with single-phase flows, convective heat transfer depends on fluid dynamic motion. So fluid dynamic scaling - matching the gas-solid motion - is a prerequisite for proper heat transfer scaling. In this chapter we describe current fluid dynamic scaling for CFB risers and then propose models for convective heat transfer scaling.

## *2.1 Hydrodynamic Scaling*

The hydrodynamics of a pilot plant and its full-scale industrial counterpart are similar if, in addition to conserving bed geometry ratios and the dimensionless Particle Size Distribution, the five dimensionless parameters mentioned in Section 1.1.2 are matched. This set of five parameters, known as the full set, provides an exact scaling (Chang, 1991), but is constraining since it requires the construction of a new laboratory model each time an industrial unit is to be studied.

Glicksman et al. (1993) derived a reduced set of four dimensionless parameters, referred to here as the reduced scaling laws. These allow greater flexibility for the scale-up of laboratory units to industrial CFBs. They studied the balance of weight and drag on a single particle and obtained, serendipitously, the same set of parameters in both the viscous and inertial limits. Bricout (2000) validated this reduced set in the intermediate regime by comparing dimensionless radial and axial profiles of solid volume fraction.

### *2.1.1 Full Set of Dimensionless Numbers*

Anderson and Jackson (1967) first presented the governing equations of the two-fluid model for solid suspensions in the absence of interparticle forces or electrostatics. The time-averaged momentum balance for the gas is

$$\rho\varepsilon \frac{Du_i}{Dt} = \frac{\partial}{\partial x_j}\left(\tau_{ij}\right) - \varepsilon \frac{\partial p}{\partial x_i} - \rho\varepsilon g_i - F_i, \tag{2.1}$$

where $\varepsilon$ is the voidage fraction, $\rho$ is the gas density, $\tau_{ij}$ is the gas stress tensor, p is the gas pressure, $F_i$ is the volumetric drag force exerted by the gas on the solids, $g_i$ is the gravity component along the interstitial gas velocity $u_i$ or the solid velocity $v_i$, and D/Dt is the substantive derivative $\partial/\partial t + u_i \partial/\partial x_i$.

The time-averaged momentum balance for the solid is

$$\rho_s(1-\varepsilon)\frac{Dv_i}{Dt} = (1-\varepsilon)\rho_s g_i - (1-\varepsilon)\frac{\partial p}{\partial x_i} + \frac{\partial}{\partial x_j} S_{ij} + F_i, \tag{2.2}$$

where $S_{ij}$ is the solid phase stress tensor and (1-$\varepsilon$) is the solid volume fraction.

Note that we have employed the mean Sauter diameter, $d_p$, as a measure of the average particle size, such that

$$d_p = \frac{1}{\sum_i^n \frac{x_i}{d_i}}, \tag{2.3}$$

and $x_i$ and $d_i$ are the weight fractions and mean diameters of particles in sieve i, respectively. The mean Sauter diameter is the diameter of an equivalent-volume sphere.

Since particles in CFBs are rarely spheres, we define a measure of particle shape, the sphericity $\phi$, as the ratio of the surface area of a sphere to the surface area of an equivalent volume particle. The sphericity appears naturally in Ergun's correlation for a packed bed of particles (Kunii and Levenspiel, 1984),

$$\frac{\Delta p}{L} = 150\frac{(1-\varepsilon)^2}{\varepsilon^3}\frac{\mu U_0}{(\varphi d_p)^2} + 1.75\frac{1-\varepsilon}{\varepsilon^3}\frac{\rho U_0{}^2}{\varphi d_p}, \tag{2.4}$$

through its product $\phi d_p$ with the mean diameter $d_p$. The governing equations for the suspension, Equations 2.1 and 2.2, can then be written based on an expression for the drag force per unit volume given by

$$F_D = C_D|\gamma_s|\gamma_s\frac{3\rho}{4d_s}(1-\varepsilon)f(\varepsilon), \tag{2.5}$$

where $\gamma_S$ is the average slip velocity vector between the gas and a particle and $f(\varepsilon)$ is a correction of the drag coefficient $C_D$ on a single particle that accounts for the presence of neighboring particles (see for instance Foscolo and Gibilaro (1984)).

Chang and Louge (1992) sought a hydrodynamic diameter of the form $d=\phi^{\alpha}d_p$, where $\alpha$ is an exponent to be determined. They incorporated Haider and Levenspiel's (1989) expression for single particle drag on non-spherical particles,

$$C_D \approx \frac{24}{Re_s}\left[1+\left(8.17e^{-4.07\varphi}\right)Re_s^{(0.096+0.56\varphi)}\right]+\frac{74Re_s e^{-5.07\varphi}}{Re_s+5.38e^{6.21\varphi}}, \qquad (2.6)$$

where $Re_s$ is based on $\gamma_s$ and $d_p$, to obtain the values of $\alpha$ that create an equivalent drag coefficient, $C_D$, as functions of the particle Reynolds number based on hydrodynamic diameter, $Re_d$, the Archimedes number $Ar = \rho_s \rho d^3 g/\mu^2$, and the sphericity $\phi$. They found that for typical particle Reynolds numbers in CFB flows between $3 \leq Re_d \leq 150$, making $\alpha$ equal to 1 would introduce a mismatch of the drag coefficient less than 17% for $\phi \geq 0.69$. Thus, for simplicity, they adopted $\alpha = 1$ and $d = \phi d_p$ for the similarity analysis.

Dimensional analysis based on CFB hydrodynamic reference parameters yields the dimensionless numbers characterizing the flow. The eight CFB reference parameters are: bed diameter D, hydrodynamic particle diameter d, solid density $\rho_s$, gas density $\rho$, gravitational acceleration g, gas viscosity $\mu$, superficial gas velocity $U_0$ and solids flux $G_s$. The superficial gas velocity is defined as the volumetric flow rate of the gas divided by the cross-sectional area of the riser. This is a convenient measure of gas velocity since it is independent of the presence of particles in the flow. (The measurement of the solids flux is described later in Section 3.2.3.)

Chang and Louge (1992) adopted the hydrodynamic diameter $d = \phi d_p$ and proposed the following five dimensionless groups to characterize CFB hydrodynamics for spherical or non-spherical particles:

$$Fr=U_0/(gd)^{1/2}, \tag{2.7}$$

$$M=G_s/\rho U_0 , \tag{2.8}$$

$$Ar=\rho_s\rho d^3g/\mu^2 , \tag{2.9}$$

$$R=\rho_s/\rho \text{ , and} \tag{2.10}$$

$$L=D/d, \tag{2.11}$$

where the Froude number is a measure of the gas velocity, the solids loading M is the ratio of solids to gas flux, the Archimedes number combines material and gas properties and gives a measure of the buoyancy in the flow, R is the solid to gas density ratio, and L is the ratio of length scales of the flow given by the ratio of bed to particle diameter.

Other dimensionally correct groupings are equally valid. With a set of five dimensionless numbers, a matched bed geometry, and a matched Particle Size Distribution (PSD), the scaling will be exact so long as effects such as interparticle forces or gas density variations due to pressure fluctuations are negligible.

The full set of dimensionless numbers is constraining, however. To achieve a full set match with a laboratory model that uses air, first the material density is chosen to match R. Next, the particle size is chosen to match Ar, and the bed diameter to match L. But then a new laboratory facility must be built to model each industrial plant of varying diameter. This led investigators to seek a reduced form of the scaling.

### *2.1.2 Reduced Set of Dimensionless Numbers*

To derive a simplified set of scaling parameters, Glicksman (1993) considered the forces on a single particle in a CFB flow, and focused on the drag force. This term can be written simply in either the viscous or inertial limit of particle Reynolds number. The drag force per unit volume of suspension in the viscous limit is

$$F_D = \frac{18\mu}{d^2} u_{slip} (1-\varepsilon), \qquad (2.12)$$

where $u_{slip}$ is the average slip velocity between the gas and solid phases. In the inertial limit, the volumetric drag force is

$$F_D = \frac{3\rho}{4d} C_D u_{slip}{}^2 (1-\varepsilon), \qquad (2.13)$$

where $C_D$ is approximately constant.

Glicksman further considered the relation between the terminal velocity of an individual particle and the drag force. Although the terminal velocity does not account for the presence of near particle neighbors, it is related to $C_D$ in the inertial limit and $\mu$ in the viscous limit. With this in mind, Glicksman (1993) substituted $U_t$ into the expressions for $F_D$, then non-dimensionalized the gas and solid momentum equations by D, $U_0$ and $\rho U_0{}^2$ for length, velocity and pressure scales, respectively. Fortuitously, Glicksman's manipulation yielded the following dimensionless numbers in either limit:

$$R=\rho_s/\rho, \tag{2.14}$$

$$Fr^2/L=U_0^2/gD, \text{ and} \tag{2.15}$$

$$U_0/U_t. \tag{2.16}$$

To capture the solid recirculation rate, Louge (1987) introduced the solids loading M. Glicksman (1993) then showed that a more natural grouping involves

$$M/R=G_s/\rho_s U_0, \tag{2.17}$$

This result provides a reduced set for matching the hydrodynamics for the case of either the viscous or the inertial limit.

Note that $U_t$ is implicitly a function of Archimedes number and sphericity, $\phi$, through correlations by Haider and Levenspiel (1989). They recommend

$$U_t=\frac{u*}{\left[\frac{\rho^2}{g\mu(\rho_s-\rho)}\right]^{1/3}}, \tag{2.18}$$

where

$$u^* = \left[ \left( \frac{18}{d^{*2}} \right) + \frac{(2.3348 - 1.7439\varphi.}{\left( d^{*0.5} \right)} \right]^{-1} \qquad (2.19)$$

and

$$d^* = d \left[ \frac{g\rho(\rho_s - \rho)}{\mu^2} \right]^{1/3} \qquad (2.20)$$

for particles with sphericity in the range $0.5 \leq \phi \leq 1$; for spheres,

$$u^* = \left[ \left( \frac{18}{d^{*2}} \right)^{0.824} + \left( \frac{0.321}{d^*} \right)^{0.412} \right]^{(-1.214)}. \qquad (2.21)$$

Although Haider and Levenspiel (1989) considered monodisperse particles, we extend their formulation to a polydisperse system. To do so, the hydrodynamic diameter d replaces the mean Sauter diameter $d_p$.

Bricout (2000) tested the validity of the reduced set in the intermediate regime, in the approximate range $20 < Re_s < 70$. To do so, he considered two gas-solid mixtures with matched parameters of the reduced set, but different Archimedes numbers and otherwise identical full set.

Bricout (2000) demonstrated hydrodynamic similarity between runs by obtaining similar dimensionless axial static pressure profiles and dimensionless radial solid concentration profiles. The magnitude of his density ratio, R=600, made his measurements relevant to the pressurized CFB regime. In fact, Bricout demonstrated the validity of

Glicksman's reduced scaling at all but one set of operating conditions. The exception concerned the lowest Fr and M with plastic material ($Fr^2/L = 2.7$, $M/R = 0.0015$, $R = 600$, $U_0/U_t = 5.43$), where the profile of radial concentration and longitudinal pressure differed despite the matching of the reduced set, likely because of a pressure recovery effect associated with wall shear forces aligned with the flow.

In short, the new "reduced set" differs from the full scaling set in that three groups, Ar, L, and Fr are replaced by two groups, $Fr^2/L$ and $U_0/U_t$. Henceforth, hydrodynamic similarity based on matching the four dimensionless numbers in Equations 2.14-2.17 will be called "reduced set similarity".

## *2.2 Convective Heat Transfer Scaling*

Because in forced convection the heat flux and energy equations are linear in the temperature of both phases, convective heat transfer rates can be evaluated for any convenient temperature difference between the wall and the suspension. Thus, if the dimensionless numbers characterizing the fluid dynamics and convective heat transfer are appropriately matched, a warm probe immersed in a cold unit can simulate convection in an industrial facility. In the absence of radiation, the convective heat transfer coefficient h, measured in $W/m^2K$, can be written as

$$q = h\,A\,(T - T_b) \qquad (2.23)$$

where q is the heat transfer rate, measured in Watts, A is the effective surface area, measured in $m^2$, and T and $T_b$ are the temperatures of the probe face and the suspension, measured in Kelvin, respectively.

In this study our aim is to identify the scaling laws for the convective heat transfer coefficient based on parameters of the CFB flow. Once fluid dynamic similarity has been achieved, the question of heat transfer similarity remains. It is necessary then to determine the important dimensionless numbers that govern heat transfer rates from the suspension to the walls of CFB risers.

### *2.2.1 General Heat Transfer Scaling*

A first approach to scaling heat transfer is to list the independent physical quantities that affect heat transfer, then form them into dimensionless groups. This process yields ratios of specific heats and thermal conductivities of the gas and particles, and the Prandtl number of the gas which is a measure of the momentum to thermal diffusivity, defined as $Pr = \mu c_f/k$. However, the ratios of specific heats for the materials in typical CFBs and their scale models do not vary significantly. The Prandtl number is order 1 for gases, and for most gases it is about 0.7. Thus it is clear that these parameter combinations do not govern the physics of heat transfer at the CFB wall.

Particles that arrive at the wall undergo a transient heat transfer process before traveling back into the core. For this process, the particle Biot number defined as $Bi = hd/k$, where in this case h refers to the convection coefficient for the particle, is appropriate to characterize the relative importance of surface convection to internal conduction effects. If Bi << 1, the resistance to conduction within the solid is much less than the resistance to convection at the solid surface. As shown in Appendix A, the Biot number for the particles in our experiments is at most 0.03. Therefore, we treat the temperature of the solid at a given instant as spatially uniform. Consequently, we can employ the "lumped capacitance method" to find a representative cooling time of a particle at the wall, as outlined in Section 2.2.4.

To investigate the effect of the thermal conductivity of the solid on the heat transfer process in CFB flows, we follow the approach of Louge et al. (1993), who studied the pneumatic transport of particles massive enough to be unaffected by turbulent velocity fluctuations. They modeled a relatively dilute, hydrodynamically fully developed steady flow with particles of low Biot number. To evaluate the relative importance of particle-particle conduction during collisions, Louge et al. (1993) considered the ratio of two time scales. The first is the time for the particle temperature to equilibrate by conduction through the area of contact,

$$\tau_e \propto \frac{\rho_s^{3/5} d^2 c_p}{\Delta_c^{2/5} v_r^{4/5} k_s}, \qquad (2.24)$$

where $\Delta_c=3(1-\sigma_p^2)/(2E)$, $\sigma_p$ is Poisson's ratio, E is Young's modulus and $v_r$ is the relative velocity of the particle at impact. The other scale is the duration of a single collision, predicted by the Hertzian contact law

$$\tau_{coll} \propto \frac{\rho_s^{2/5} \Delta_c^{2/5} d}{V_r^{1/5}} . \tag{2.25}$$

When the ratio $\tau_e/\tau_{coll} >> 1$ the heat conducted during an individual particle impact is negligible. Using an estimate of the relative velocity of the particles as 2% of the superficial gas velocity and the gas and solid properties of our flow, $\tau_e/\tau_{coll}$ can be shown to be of the order of $10^7$. Then the solid conductivity of the particles should not be an important mechanism for convective heat transfer to the wall, as long as individual particle contacts are impulsive.

In summary, because the ratio of solid to gas specific heats and the Prandtl number do not vary appreciably among different suspensions, and because the solid conductivity is expected to play a minor role, the derivation of meaningful thermal dimensionless numbers cannot be accomplished without considering parameters involving gas-solid hydrodynamics. To do so, we must turn to a physical description of the thermal flow, rather than using dimensional analysis, or the Buckingham Pi-Theorem, blindly.

### *2.2.2 Hydrodynamics for Convective Heat Transfer Modeling*

Glicksman (1997) wrote a comprehensive review of heat transfer modeling for CFBs. He emphasized that bed to wall heat transfer in these facilities is strongly influenced by hydrodynamics, especially the particle and gas behavior close to the wall. His preference is toward basic models that incorporate the relevant physics instead of those with unwarranted complexity, since the latter may have increased uncertainties due to a larger number of input parameters. The first step in considering thermal exchanges at the wall is to focus on the structure of the flow in its vicinity.

The overall structure in a CFB consists of a fast, relatively dilute upflowing core of gas and particles, and a surrounding annulus where gas velocity is reduced and particles fall downward near the wall. Clusters of particles at the mean bed temperature enter the annular region near the wall. Measurements at the wall reveal rapid fluctuation of local solid volume fraction with time, indicating that particle clusters travel quickly, replaced by a relatively dilute mixture (Louge, et al., 1990; Griffith, et al., 2000).

High-speed videos of cluster motion near the wall by Rhodes (1992) reveal clusters, or swarms of particles, that travel primarily downward at the wall. Lints and Glicksman (1993b) designed an experiment to measure how far clusters travel from the CFB wall. He inserted a phonographic stylus to varying penetration depths into the suspension. By measuring the number of incident collisions with the stylus as a function of intrusion depth, he discovered that clusters generally travel within one third to one particle diameter from the wall.

In mass transfer experiments by Ebert et al. (1993), maleable, smooth napthalene panels were aligned flush with the CFB wall. After running the facility, they examined the panels under a microscope and found no visible traces of particle impacts with the napthalene surface. This suggests that particles rarely collide head-on with the CFB wall.

Although descending cluster velocities are reported in several studies, their scaling with riser conditions and suspension parameters has remained unclear. For simplicity, Lints and Glicksman (1993a) assumed that cluster velocity is a constant of about 1 m/s in order to calculate the cluster contact time with the wall, while Glicksman (1997) scaled the cluster residence time using the superficial gas velocity. Our inspection of earlier studies implies a different scaling.

Table 2.1 summarizes descending cluster velocities recorded by several authors under a wide variety of flow conditions. The data are collected primarily in the upper region of the riser where the flow is likely to be fully-developed. We exclude data recorded in the bottom acceleration zone or under unusual circumstances. For example, we do not consider the descending wall velocities of single clusters injected in an otherwise empty tube (Glicksman, 1988). Although these velocities have similar magnitudes to those observed in a more conventional riser suspension, such a flow with negligible vertical pressure gradient is not likely governed by similar physics. Perhaps as a consequence, cluster velocities in that unusual flow are relatively independent of particle size.

The cluster velocities in Table 2.1 span a range of approximately a factor of two. As Figure 2.1 indicates, they appear to scale with the square root of the particle diameter and the gravitational acceleration,

$$U_{cl} \approx 36\sqrt{gd}\,. \tag{2.26}$$

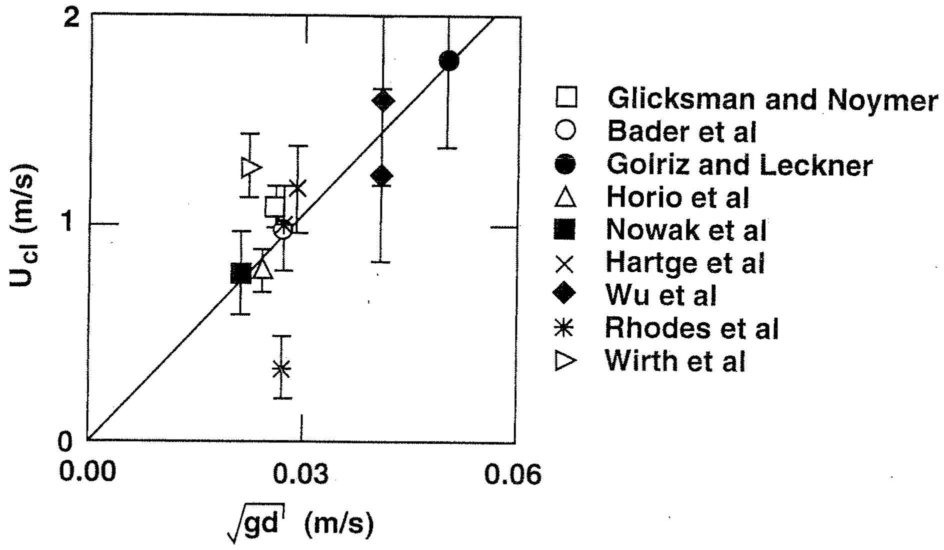

Figure 2.1. Measured cluster velocities (Griffith and Louge, 1998).

The trend of Equation 2.25 is represented as a solid line. The lowest recorded velocity is for rare, slow strands in close proximity with the wall (Rhodes et al., 1992), and thus it does not pertain to the other, faster regime of bulk downflow observed by all other authors.

Table 2.1 Descending cluster velocities at the wall, $U_{cl}$.

| Authors | Measurement technique | $U_{cl}$ (m/s) | $U_0$ (m/s) | $z/H$ | $G_s$ (kg/m$^2$ s) | $T$ (°C) | $D$ (cm) | $\rho_s$ (kg/m$^3$) | $d$ ($\mu$m) |
|---|---|---|---|---|---|---|---|---|---|
| Glicksman and Noymer (1996) | Thermal imaging | 1.1 ± 0.1 | 2.3–3.6 | 0.21 | 8–28 | 20 | 16* | 6980 | 69 |
| Bader *et al.* (1988) | Pitot tube | 1.0 ± 0.2 | 3.7 | 0.75 | 98 | 20 | 31 | 1714 | 76 |
| Golriz and Leckner (1992) | Thermocouples | 1.8 ± 0.4 | 3.6–6.7 | 0.81 | ~10 | 850 | 170* | 2600 | 260 |
| Horio *et al.* (1988) | Optical fibers | 0.8 ± 0.1 | 1.2 | 0.58 | 11.7 | 20 | 5 | 1000 | 60 |
| Nowak *et al.* (1991) | Optical fibers | 0.8 ± 0.2 | 4.0 | 0.28 | 55.7 | 20 | 21 | 2300 | 46 |
| Hartge *et al.* (1988) | Optical fibers | 1.2 ± 0.2 | 2.9 | 0.56 | 49 | 20 | 40 | 1500 | 85 |
| Wu *et al.* (1991) | Heat transfer probe | 1.6 ± 0.5 | 7.0 | 0.43 | 15-47 | 20 | 15 | 2650 | 171 |
| Wu *et al.* (1991) | Video | 1.3 ± 0.5 | 7.0 | 0.43 | 15–47 | 20 | 15 | 2650 | 171 |
| Wirth *et al.* (1991) | Video | 1.3 ± 0.2 | 1.2 1.9 | 0.73 | — | 20 | 17* | 3950 | 50 |
| Rhodes *et al.* (1992) | | | | | | | | | |
| wall strands | High-speed video | 0.3 to 0.4 | 3–5 | 0.53 | 2–80 | 20 | 31 | 2456 | 75 |
| bulk downflow | | ~1 | | | | | | | |

* Square cross-section.

This trend is remarkably robust, considering the broad variations in solid flux, superficial gas velocity, riser diameter, riser geometry and solid density among those experiments. The measurements of Glicksman and Noymer (1996) and Wu, et al. (1991) confirm that the cluster velocity is relatively insensitive to the solid flux and superficial gas velocity. The high temperature tests of Golriz and Leckner (1992) further suggest that the gas density and viscosity also fail to influence the trend.

Rhodes, Mineo and Hirama (1992) exploit the high temporal and spatial resolution of a high-speed video camera to distinguish two families of clusters. The first consists of occasional, relatively slow strands in close proximity or contact with the wall. The second is a more prominent bulk downflow slightly farther from the wall; it exhibits a faster velocity in agreement with the trends summarized in Table 2.1. Because the other authors do not distinguish between the two families, their measurements are likely dominated by the uninterrupted, faster bulk downflow. Remarkably, the downward velocity of neither class appears to be affected by the superficial gas velocity or overall solid flux. The velocity difference between the two classes may reflect the downward shearing of the particle phase at the wall. For completeness, the Table provides cluster velocities measured by Rhodes, Mineo and Hirama for both classes.

Because the cluster velocity is seemingly unaffected by overall flow conditions, it is likely that it is set by a local force balance at the wall. Its apparent insensitivity to the properties and velocity of the gas further suggests that interactions in the particle phase dominate the balance. In this case, the only parameters relevant to the velocity scaling would include the material density and mean diameter of the particles, the gravitational acceleration and, if the particles are engaged in collisional interactions, the parameters characterizing the impacts. Because in this formulation the particle material density is the only parameter involving mass, it cannot appear in the velocity scaling. In addition, because collisional parameters often belong to a relatively narrow range of values (Massah, et al, 1995; Lorenz, Tuozzolo and Louge, 1997), we expect that cluster velocities from a wide range of experiments would indeed scale as $\sqrt{gd}$.

### *2.2.3 Convective Heat Transfer Mechanisms*

Convective heat transfer in CFBs may involve two possible mechanisms of heat transfer to the wall. The first is called “gas convection”. It refers to the energy transfer associated with the motion, heat capacity, and thermal conductivity of the gas. Gas convection can be augmented by the presence of particles, if particle motion increases gas mixing. In this case, the particles act as 'turbulence promoters'. However, because large particles generally enhance turbulence while small ones suppress it (Tsuji et al., 1984; Gore and Crowe, 1989), it is more likely that single-phase turbulence, at least in the classical sense, is suppressed by the presence of particles in a CFB. In fact, the particle and velocity fluctuations in the relatively dense CFB are likely associated with cluster dynamics

(Dasgupta et al., 1997; Dasgupta et al., 1998) rather than conventional turbulence.

The other mechanism "particle convection", arises mainly from the motion and heat capacity of the particles. Here, particles store and transport heat as they move from the core of the CFB to the wall. In this case, the convection of solid particles governs heat transfer.

Ebert et al. (1993) conducted an experiment to find the relative importance of the particle and gas convective components. Since the particles transported heat but not mass, measurements of the mass transfer and heat transfer coefficients revealed the importance of the effect of particle convection. They found that the presence of the particles increased mass transfer rates (gas convection) by up to 50% and increased heat transfer rates (gas and particle convection) by an order of magnitude. This demonstrated that particle convection is the dominant mechanism of convective heat transfer to the wall of CFBs.

### *2.2.4 Discrete Particle Model*

We now present a basic conceptual model suggesting the importance of thermal and dynamic mechanisms in the particle convective process. In this model, a particle with temperature $T_p$ arriving at the wall first transfers heat by conduction through a gas layer. Here we use the lumped capacitance analysis, treating the instantaneous temperature of the particle as uniform, since, as shown in Appendix A, the Biot number is at most 0.03. A transient heat balance on a particle that conducts its heat to the wall through a gap one particle diameter thick can be written as

$$\rho_s c_p d^3 \frac{dT_p}{dt} \propto \left(\frac{k}{d}\right)\left(d^2\right)\left(T_w - T_p\right). \qquad (2.27)$$

The solution of the associated first order ODE is an exponential temperature decay with time. Then the 1/e decay time is a thermal time constant that represents the time for a particle to cool by conduction through a gas layer,

$$\tau_p \propto \frac{\rho_p c_p d^2}{k}. \qquad (2.28)$$

From this model, we expect that the total amount of heat transferred from the solid to the wall will depend on the relative magnitude of the time constant $\tau_p$ and the residence time of solids at the wall.

The corresponding ratio will then capture the dependence of the particle cooling time on particle density, specific heat, and diameter and on the thermal conductivity of the gas. It will also incorporate elements of the particle motion at the wall. In short, we anticipate that this dimensionless ratio of time scales will govern heat transfer at the wall.

### *2.2.5 Continuum Model*

In order to refine an understanding of thermal transfer at the wall, we turn to a phenomenological model proposed by Lints and Glicksman (1993). In particular, we will review its principal ingredients and discuss its corresponding assumptions. In this model, there are two parallel paths for heat transfer from the wall to the suspension. The first is convection heat transfer from the wall to the dilute phase, with an associated thermal resistance $R_g$. The second is the heat transfer from the wall through a thin gas layer and then into a cluster. We decompose this latter path into two heat transfer processes that occur in series. The first, conduction through a thin layer of gas, has a thermal resistance $R_w$. The second path, with thermal resistance $R_H$, is heat transfer into a cluster. Figure 2.2 shows a schematic of the heat flow paths and equivalent thermal resistances. Since for convection heat transfer, the thermal resistance is given by (1/hA), where h is the heat transfer coefficient and A is the area normal to heat flow, the inverse of the thermal resistance for each path is the associated conductance, h. Next we describe how we estimate the conductance for each heat transfer path.

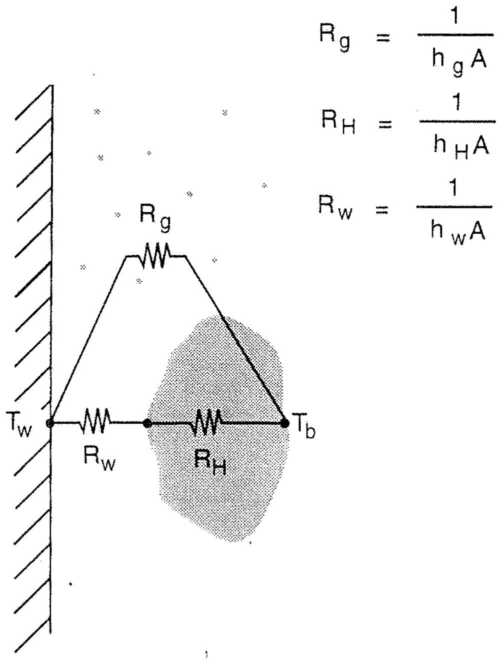

Figure 2.2 Heat flow model proposed by Lints and Glicksman (1993a), here referred to as the continuum model for convective heat flow to the CFB wall.

Before we model the heat transfer to the cluster phase, let us consider a simple but related heat transfer process. This problem is the transient heat conduction into a semi-infinite slab from a surface at constant temperature $T_s$. The slab is initially at a uniform temperature $T_i$. In this process, the heat flux at the surface is equal to $(T_s-T_i)(\rho c_p k/\pi t)^{1/2}$, where in this case $\rho$, $c_p$ and k are the density, specific heat and thermal conductivity of the slab material, respectively, and t is time.

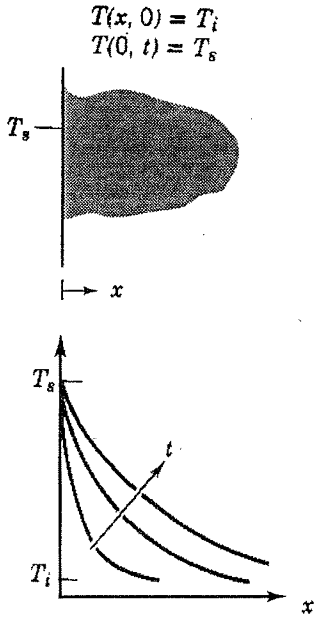

Figure 2.3. Transient heat conduction from a constant temperature surface into a semi-infinite slab (schematic is Case (1) of Figure 5.17 of Incropera and DeWitt, 1990).

In the context of bubbling beds, Mickley and Fairbanks (1955) formulated a similar model for the heat transfer between the emulsion and the wall, where the emulsion is treated as a homogeneous medium. By assuming that the emulsion thickness exceeds the thermal penetration depth, they treated the emulsion as semi-infinite in extent, and used the expression for the heat flux for the problem of transient conduction into a semi-infinite slab. Then, by employing effective thermal properties for the emulsion phase and time averaging, they derived a representative heat transfer coefficient for the emulsion in contact with the wall of the form

$$h_H = 2\sqrt{\frac{k_e \rho_s c_p \upsilon_c}{\pi \tau_c}}, \tag{2.29}$$

where $\tau_c$ is the average contact time between the emulsion and the wall, averaged over the number of emulsion packets, $k_e$ is the effective conductivity of the emulsion and $v_c$ is the average cluster solids fraction. In Appendix B, we present a summary of Mickley and Fairbanks' derivation of Equation 2.29.

Lints and Glicksman (1993a) adopted this model for CFBs, with one alteration. Since in CFB flows, clusters are actually separated from the wall by a thin gas layer, they suggested treating the heat transfer as occuring in series: first conduction through the gas layer, then followed by heat transfer into the cluster phase, as shown in Figure 2.2. For the thermal resistance $R_W$ representative of conduction through the gas layer, they defined

$$h_W = k/d\delta, \tag{2.30}$$

where $\delta$ is the dimensionless gas layer thickness. Then the total thermal resistance to heat transfer from the wall to the suspension through the gas gap and the cluster phase was $R_W + R_H$.

To determine $k_e$, Glicksman (1997) used the empirical correlation of Gelperin and Einstein (1971)

$$\frac{k_e}{k} = 1 + \frac{\upsilon_c\left(1 - \dfrac{k}{k_s}\right)}{\left(\dfrac{k}{k_s}\right) + 0.28(1-\upsilon_c)^{M_2}}, \qquad (2.31)$$

where $M_2 = 0.63\ (k_s/k)^{0.18}$. Note that for typical values of the cluster solid fraction $\nu_c$ and gas and solid conductivities in CFB's, Equation 2.31 gives an effective conductivity of the emulsion that is simply a factor of 1.5 to 2 larger than the fluid conductivity (Noymer, 1997; Glicksman 1997).

However, as mentioned in Section 2.2.1, the solid conductivity should not play a major role in heat transfer rates. Further, it is wrong to assume that the thermal conductivity of a suspension of free-flowing solid particles in a gas may be represented by an effective, purely conductive coefficient $k_e$ that ignores the local convective heat transfer associated with the crossflow around individual solid particles. For these reasons, we prefer to ignore the inclusion of $k_e$ in Equation 2.31. Instead, we replace the effective conductivity $k_e$ by the gas conductivity k.

The representative heat transfer coefficient due to the particle convection process at the wall can then be modeled as conduction through the gas layer and subsequent conduction into the cluster, yielding $R_{pc} = R_H + R_w$, or in terms of the conductances,

$$h_{pc} = \left[\frac{1}{h_H} + \frac{1}{h_w}\right]^{-1}. \qquad (2.32)$$

where $h_{pc}$ is the heat transfer coefficient due to the particle convection heat transfer at the wall.

There are two major assumptions of the continuum model. The first is to describe the heat flow by a steady circuit, according to Figure 2.2. Since clusters are continually arriving at the wall, traveling for some distance, and then returning to the core, the flow is not at steady state. However, the model uses a time-averaged value of the heat transfer coefficient for the cluster phase, $h_H$, averaged over the average residence time of the clusters. In this way, the model is adapted to fit the constantly renewed cluster deposition and transient heat transfer to the wall.

The other critical assumption in the model regards the semi-infinite extent of the cluster phase. By assuming that the thermal penetration depth into the cluster is less than the cluster thickness, we simplify the expression for the heat transfer coefficient. However, this is only valid if the cluster thickness is large enough. For a cluster with residence time of 1 second, the thermal penetration depth is 1 mm (Glicksman, 1997). Since residence times are generally one second or less (Noymer, 1997), and clusters are generally at least 20 particle diameters thick (Glicksman, 1997), this assumption should be reasonably accurate.

### 2.2.6 Gas Convection

For the CFB wall surface not in contact with clusters, Lints (1992) adopted a dilute heat transfer coefficient. He surveyed existing heat transfer measurements at low cross-sectional solid densities (< 50 kg/m$^3$) and estimated $h_g$ by extrapolating the results to zero density. He found that this dilute phase heat transfer coefficient, $h_g$, was larger than correlations for gas phase flow alone.

### *2.2.7 Overall Heat Transfer Coefficient*

In the simple view that the wall is alternately covered by clusters or a dilute phase, each contributing to the overall heat transfer in linear proportion to their respective wall coverage, the total heat transfer coefficient can be written

$$h_{overall} = f_h h_c + (1 - f_h) h_g . \tag{2.33}$$

In this way, Lints and Glicksman (1993a) derived a dependence of the overall heat transfer coefficient on the five empirical parameters listed in Section 1.2. However, these five parameters are difficult to predict a-priori for varying run conditions or facility sizes. In an effort to inform the model, we now turn to recent measurements and trends of these five parameters in bubbling beds and circulating fluidized beds.

The fraction of the wall covered by clusters, $f_h$, is an important parameter since particle convection is the dominant mechanism for heat transfer to the wall. Lints and Glicksman (1993a) compiled results from video images, impact probes, and solid fraction traces at the wall. For the solid fraction measurements, they assumed that the spatial coverage was equal to the temporal coverage, then measured $f_h$ using an arbitrary cutoff for cluster definition, namely $\nu_c \geq 5\%$. By analyzing data from seven different investigators (Rhodes et al., 1991; Lints, 1992; Louge et al., 1990; Glicksman et al., 1991; Wu, 1989; Dou, 1990; Li et al., 1991) they fit the following correlation for fractional coverage as a function of the cross-sectional solid concentration:

$$f_h = 3.5(\overline{v})^{0.37} \qquad (2.34)$$

The data generally fit the model to within 40%, but since by definition, $f_h$ is between 0 and 1, it would be helpful to have a more precise model. Also, since Lints' correlation (1993) is only a function of cross-sectional solid fraction, the information is not readily scalable to risers with different operating conditions or size.

Further, Glicksman (1997) observed that the fractional wall coverage data from larger risers ($D \geq 20$ cm) is consistently higher than from smaller risers. Thus it appears that $f_h$ may be at least a weak function of bed diameter.

The thickness of the gas layer between the clusters and the wall is important since it limits the heat transfer process from the clusters. Lints and Glicksman (1993) propose to make the gas layer thickness dimensionless with particle diameter, a method that emphasizes the local nature of the flow near the wall.

For bubbling beds, Decker and Glicksman (1981) and Glicksman et al. (1994) measured a dimensionless gap thickness, $\delta$, of about 1/6. In CFB flows, Lints and Glicksman (1993b) used an intrusive particle impact probe to measure the gap thickness to the edge of passing clusters in their 20 cm diameter riser. They found a dependence on cross-sectional solid concentration of the form

$$\delta = 0.0282(\bar{v})^{-0.59}, \tag{2.35}$$

and a slight trend of increased δ with higher superficial gas velocities.

Wirth and Sieter (1991) used γ-ray absorption to measure the gap thickness at the wall. However, their resultant gap thickness of almost 1 mm, when used in this heat transfer model, yields a heat transfer coefficient that is much smaller than values typically measured in CFBs.

Lints (1992) derived the average cluster solid volume fraction $\nu_c$ at the wall by analyzing data from his own and other investigations (Wu, 1989; Dou, 1990; Louge et al., 1990). He fit a correlation as a function of cross-sectional solid concentration:

$$\nu_c = 1.23(\bar{v})^{0.54}. \tag{2.36}$$

A study by Soong et al. (1994) found $\nu_c$ between 10 and 30%. Data from our study show cluster solid volume fractions between 1 and 25% where the values are a strong function of cross-sectional solid concentration.

Direct measurement of the residence time of clusters at the wall very quickly reach a constant velocity (Noymer, 1997), we choose to infer this quantity from the scaled average cluster velocity discussed in Section 2.2.2 and our measurement of the average residence length of clusters at the wall.

Wu et al. (1991) measured a dependence of the residence length of clusters $\lambda$ on the cross-sectional suspension density. They used a cross-correlation technique with two heat transfer probes. They correlated their results with

$$\lambda = 0.0178(\rho_{susp})^{0.596} \tag{2.37}$$

where $\lambda$ is the residence length of clusters traveling near the wall before being ejected back into the core, and $\rho_{susp}$ is the average cross-sectional density in the riser at that height.

In our study, we measure the average residence length of clusters at the wall under varying run conditions and material combinations. We also measure the residence length in experiments analogous to two different riser diameters. For a more detailed description, see Section 3.3.

It is clearly important to include the dilute phase heat transfer coefficient $h_g$ in the model. Although some investigators have treated the heat transfer surface as if it were entirely covered by clusters (Sekthira et al., 1998; Dou, 1990), Glicksman (1997) emphasizes that in dilute suspensions, $h_g$ will certainly influence the overall heat transfer coefficient.

Ebert et al. (1993) have shown that gas convection increases by up to 50% due to the presence of particles (see Section 2.2.6) and this effect of the particles will certainly raise $h_g$ above that of single phase flow. However, Lints and Glicksman (1993a) showed that single-phase correlations based on superficial gas velocity and riser diameter could be used to estimate the extrapolated $h_g$ to within 10 to 40%.

### *2.2.8 Dynamic Scaling*

The last step in finding a heat transfer scaling is to examine the dynamic process of the dominant heat transfer mechanism at the wall. Because it has been shown that clusters dominate the heat transfer to the wall, Glicksman (1994) proposed a quantity that compares the time for a cluster to cool near the CFB wall to the average residence time of clusters at the wall. This ratio of time constants characterizes the competition between the rate of cooling and the residence time at the wall.

Once the hydrodynamics are rendered similar by use of the scaling laws according to the procedure of Section 2.1, parameters such as $\overline{\upsilon}$, $f_h$, and $v_c$ should be matched. This allows us to scale the dimensionless convective heat transfer coefficient as follows.

According to the continuum model, the overall heat transfer to the wall is

$$h_{overall} = f_h h_{pc} + (1 - f_h) h_g . \tag{2.33}$$

However, because Ebert et al. (1993) measured a much smaller gas convective component than particle convective term, we have approximately

$$h_{overall} \propto f_h h_{pc}, \tag{2.38}$$

unless the suspension is very dilute. Substituting equation (2.32), we find

$$h_{overall} \propto \frac{f_h}{\dfrac{1}{h_H} + \dfrac{1}{h_w}}. \tag{2.39}$$

But Glicksman (1997) uses correlations for $v_c$, $\delta$, and $f_h$ to evaluate the relative magnitudes of $h_w$ and $h_H$. He finds that, as the particle diameter increases from 50 to 200 μm, the residence length increases from 1 cm to 1 m, and thus $h_w$ goes from a factor of two to an order of magnitude larger than $h_H$. Because $h_w$ gets very large compared to $h_H$, the fraction $1/h_H$ dominates the behavior of $h_{overall}$. By neglecting $1/h_w$, replacing $k_e$ by k as discussed in Section 2.2.5, and invoking Equation 2.28 for $h_H$, we find

$$h_{overall} \propto f_h \sqrt{\frac{k \rho_s c_p v_c}{\tau_c}}, \tag{2.40}$$

or, in dimensionless form,

$$\mathrm{Nu}_{\mathrm{overall}} \propto f_h \sqrt{\frac{\rho_s c_p d^2 \nu_c}{\tau_c k}}\,. \qquad (2.41)$$

If we assume that $\nu_c$ and $f_h$ have the same value for hydrodynamically matched runs, we find

$$\mathrm{Nu}_d \propto \sqrt{\frac{\rho_s c_p d^2 U_{cl}}{k\lambda}} \propto \sqrt{\frac{\tau_p}{\tau_c}}\,. \qquad (2.42)$$

where $\lambda/U_{cl}$ is a characteristic scale for particle cluster residence time at the wall. Our experiments will determine to what degree these approximations have any merit.

# CHAPTER THREE:
# EXPERIMENTAL SET-UP AND PROCEDURE

This chapter presents the Cornell CFB facility, its operating procedures and our plan of experiments. Our objective is to investigate the relation between the heat transfer coefficient at the wall and the thermal parameters of the flow, while maintaining similar hydrodynamics in the upper riser.

## *3.1 The Experimental CFB Facility*

The Circulating Fluidized Bed facility at Cornell (Figure 3.1) is a scaled-down model of larger industrial CFB combustors. It is a closed loop consisting of a Roots centrifugal blower, two cyclones, a 1.25 $m^3$ Torit (TD 573) filter baghouse with Ultra Web II cartridges, a tank acting as a pressure buffer and connecting pipes. The closed loop allows recirculation of both the gas mixture and the particles. The facility was built and initially tested by Hongder Chang (1991). Because it operates near ambient temperature, we employ a heated probe surrounded by guard heaters to investigate convective heat transfer rates from the wall to the flow.

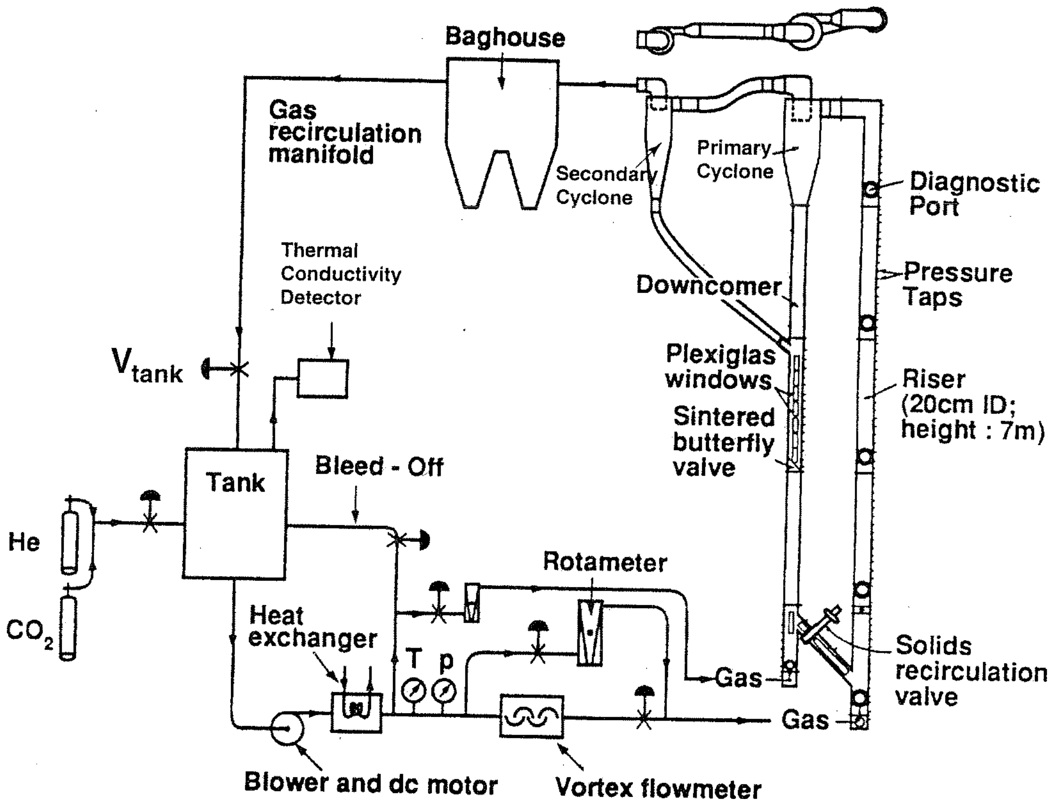

Figure 3.1. Schematic of the CFB facility at Cornell.

The blower forces gas into the riser section, where it fluidizes the particles, carrying them upwards. Eventually, the solids are carried out of the top of the riser into the primary cyclone, which separates the particles from the gas using centrifigal forces and gravity. The bulk of the solids travel down the downcomer pipe, before being recycled into the base of the riser section.

### *3.1.1 The Riser Section*

The riser is a 7-meter tall aluminum pipe of 19.7 cm ID and 0.15 cm wall thickness. As gas approaches the base of the riser, it changes direction by 90 degrees, then travels through the stainless steel mesh distributor plate before flowing upwards. Chang (1991) provides detail of the distributor design. At the top of the riser, a 90 degree elbow directs the flow into the primary cyclone.

### *3.1.2 The Cyclones*

Cyclones are passive devices utilizing centrifigal forces and gravity to separate particles from the gas stream. At the exit of the riser, two cyclones are connected in series to capture nearly all particles and return them to the downcomer. The cyclones are made of 14 gauge mild steel, and were designed by Chang (1991) according to Stairmand's rules. Bricout (2000) characterized their efficiencies under various run conditions analogous to pressurized fluidization.

### *3.1.3 The Downcomer*

The downcomer section is a 14.7 cm ID aluminum pipe that stores and supplies particles, while creating an adequate pressure head to recirculate solids back to the base of the riser. During operation, particles stored in the downcomer fall downward against a slight countercurrent gas flow that is just large enough to keep the particles fluidized.

At the midsection of the downcomer, a sintered butterfly valve is used during measurements of the solid flux. Plexiglass windows located along the downcomer allow the operator to check that the solids are flowing, to measure the overall solid flux from the solid accumulation time (Section 3.2.3), and to allow a visual check of electrostatic charging which, in extreme cases, may cause particles to adhere to the windows. To limit the electrostatic charging, we occasionally add small amounts of quaternary ammonium salt (Larostat 519) and we ground the facility (Chang and Louge, 1992). For experiments with glass beads, we typically employ 0.2% Larostat powder by solid inventory mass, and for plastic grit, we use 0.5% by mass.

### *3.1.4 The Heat Exchanger*

Because the gas mixture is compressed in the blower, its temperature increases. To maintain the riser inlet gas at a constant near-ambient temperature, we manually adjust the flow rate of cold water through a countercurrent heat exchanger (Xchanger model C-175-6) located just downstream of the blower until the desired temperature is recorded by a thermometer inserted in the flow. The actual bed temperature is recorded by a thermocouple located about 1 m below the probe, that is inserted 1" into the flow.

### *3.2 CFB Diagnostics*

This section describes the sets of systems and instruments to measure gas and solid flow rates in the CFB, and to verify fluid dynamic similarity among distinct experimental runs.

#### *3.2.1 Pressure Profile Measurement*

The CFB riser is equipped with 35 pressure ports to measure the static pressure profile along the axis. The ports are evenly spaced – every 15 cm in the bottom half of the riser, and every 30 cm in the top half. To prevent blockage of the taps by particles, fine wire meshes are soldered over the entrance to each line.

The 35 pressure taps are connected to a scanning valve (Scanivalve J-9) using PVC tubing. A Hewlett Packard-UX computer uses an RS-232 serial interface to control the valve, sequentially exposing each line to a single calibrated pressure transducer. The pressure data acquisition process takes about 15 minutes. This single-transducer method eliminates possible differences in the systematic error for the pressure measurements at different elevations.

#### *3.2.2 Superficial Gas Velocity Measurement*

We measure the gas flow rate upstream of the riser with a Foxboro vortex flow meter, model E83W. To account for density differences, we assume that the gas temperature is constant, and we multiply the measured flow rate by the ratio of static pressures upstream and downstream of the distributor plate. We then calculate the superficial gas velocity $U_0$ by dividing the resulting flow rate by the cross-sectional area of the riser. Because the relative pressure loss through the riser and the temperature rise associated with the wall heaters are small, the superficial gas velocity is nearly constant along the entire riser elevation.

### *3.2.3 Solids Flux Measurement*

After the facility reaches hydrodynamic steady state, we measure the superficial gas velocity and solids flux through the riser. The latter is found by shutting the butterfly valve in the downcomer and measuring the time necessary for solids to accumulate 16.5 cm above the valve in the downcomer. Then, a relation incorporating the packing properties of the solids is employed:

$$G_S=\rho_S(1-\varepsilon)\Delta h/\Delta t, \tag{3.1}$$

where $\rho_S$ is the solid density, $\Delta h = 16.5$ cm, and $\Delta t$ is measured with a stopwatch. In this expression, the solid fraction at loose packing is $(1-\varepsilon) = 53.1\%$ for plastic grit and 62.4% for glass spheres.

### *3.2.4 Gas Mixture Composition*

We use a Thermal Conductivity Detector (TCD) to test the gas composition before and after taking data. Since mixtures containing sulfur hexafluoride ($SF_6$) would dissociate when exposed to the 400 °C sensor element of the TCD, we use an alternate method for those gases. The gas composition measurement for these runs is a static pressure measurement. We use a relative pressure gauge (Baratron model 223B pressure transducer with resolution of 0.01 torr) to measure the pressure difference at the top and bottom of the riser, allowing us to ascertain the gas density, and in this way determine the composition. Bricout (2000) gives a detailed description of this procedure.

### *3.3 Strategy of experiments*

The principle of our experiments is to maintain hydrodynamic similarity in the upper riser of our facility while conducting heat transfer measurements with gas and solid materials of differing thermal properties. Because we did not know a priori the cluster wall residence length, we could only prescribe the product $\tau_p U_{cl}$ entering the ratio of time constants, while speculating at the outset that the residence length $\lambda$ varied with the particle diameter. We then verified this scaling of the residence length $\lambda$. This approach allowed us to examine the relation between the ratio of time constants ($\tau_p U_{cl}/\lambda$) and the heat transfer coefficient.

Table 3.1 summarizes the experimental mixtures and assigns a number to each of them. Across experiments 1-3, we match the hydrodynamics using the reduced set scaling laws, as explained in Chapter Two. In experiments 1 and 2, we hold the product $\tau_p U_{cl}$ constant, while in experiment 3, we vary this number by a factor of 2.2. In each experiment we measure the residence length. By measuring the heat transfer coefficient for all runs, we examine the change in dimensionless heat transfer coefficient caused by a variation of the ratio of time constants, the repeatability (in the matched $\tau_p U_{cl}$ case) and the effects of the operating conditions.

Table 3.1 Plan of experiments.

| Experiment Number | hydrodynamic diameter (μm) | solid material | gas composition (by mole) |
|---|---|---|---|
| 1 | 102 | glass | 50% $CO_2$, 50% air |
| 2 | 104 | plastic | 67% air, 33% He |
| 3 | 107 | glass | 60% He, 16% $SF_6$, and 24% $CO_2$ |
| 4 | 64 | glass | 50% $CO_2$, 50% air |

In experiment 4, we investigate the scaling of the residence length by varying the particle diameter. Because with available materials a change of more than about 10% in the particle diameter causes a mismatch in the reduced set numbers, we employ the full set to match the hydrodynamics instead. Consequently, experiment 4 is matched to experiment 2 through the full set of dimensionless parameters, except the ratio of bed to particle diameter L, which is increased by about 39%. This method follows the approach of Chang and Louge (1992), who investigated the effect of scale-up in otherwise matched risers.

### *3.3.1 Choice of Solid Material and Gas*

We choose the solid materials, particle sizes, and gas composition of the first three experiments to match the reduced set of dimensionless numbers. To vary the solid material, we use glass and plastic powders, of densities 2530 and 1440 kg/m$^3$, respectively. To hold the ratio of solid to gas density, R, constant, the gas densities must vary: we use a 'light' gas mixture with the plastic and a 'heavy' gas mixture with the glass, as shown in Table 3.2.

Because the matching of the group Fr$^2$/L requires the matching of $U_0$, the matching of $U_0/U_t$ requires in turn that we match $U_t$. To do this, we seek particle diameters and gas viscosities that produce identical terminal velocities according to Haider and Levenspiel.

Table 3.2. Gas, solid, suspension and dynamic properties of the mixtures. The first three material sets are matched by the reduced scaling laws. The 64 μm glass particle set is matched to the 104 μm plastic inventory set via the full scaling laws, except for the dimensionless number L.

| Solids | plastic | glass | glass | glass |
|---|---|---|---|---|
| d (μm) | 104 | 107 | 102 | 64 |
| $\rho_s$ (kg/m$^3$) | 1440 | 2530 | 2530 | 2530 |
| Gas<br>(by mole) | 66.9 % air<br>33.1 % He | 60.1 % He<br>16.1 % SF6<br>23.8 % $CO_2$ | 50.4 % air<br>49.6 % $CO_2$ | 50.4 % air<br>49.6 % $CO_2$ |
| $\rho$ (kg/m$^3$) | 0.86 | 1.51 | 1.51 | 1.51 |
| $\mu$ (Pa · s) | $1.91 \times 10^{-5}$ | $1.81 \times 10^{-5}$ | $1.61 \times 10^{-5}$ | $1.61 \times 10^{-5}$ |
| k (W/mK) | 0.048 | 0.052 | 0.020 | 0.020 |
| R | 1678 | 1675 | 1675 | 1675 |
| $u_t$ (m/s) | 0.56 | 0.56 | 0.56 | 0.26 |
| $U_{cl}$ (m/s) | 1.15 | 1.17 | 1.14 | 0.90 |
| $\tau_p$ (s) | 0.474 | 0.449 | 1.053 | 0.408 |
| L | 1902 | 1840 | 1930 | 3100 |
| Ar | 37 | 140 | 153 | 37 |

Notice that for all runs, the density ratio, R, is near 1675. This corresponds to a coal combustor pressurized to 0.64 MPa, as described in the scale-up rules of Chang and Louge (1992).

### *3.3.2 Choice of Operating Conditions for the Reduced Set Runs*

To obtain reduced hydrodynamic similarity, four parameters must be matched. Two numbers are based on material properties, and the other two incorporate operational conditions. They are

$$R \text{ and } \frac{U_0}{U_t}, \qquad \frac{Fr^2}{L} \text{ and } \frac{M}{R},$$

where the first pair fixes gas and solid properties and the second fixes operational conditions. Note that because matching $Fr^2/L$ determines the superficial velocity $U_0$, then the matching of $U_0/U_t$ fixes the terminal velocity $U_t$, which incorporates material properties. Values of the reduced set for experiments 1-3 are shown in Table 3.3.

Table 3.3. Variation of operating conditions for runs matched via the reduced set.

| R | $U_0/U_t$ | $Fr^2/L$ | M/R | designation |
|---|---|---|---|---|
| 1676 | 5.8 | 5.5 | 0.0015 | "low Fr, low M" |
| 1676 | 5.8 | 5.5 | 0.0060 | "low Fr, high M" |
| 1676 | 8.6 | 12.1 | 0.0060 | "high Fr, high M" |

Table 3.4 Variation of operational conditions for runs matched via the full set (experiments 2 and 4 from Table 3.1). Plastic and glass runs have L=1902 and 3102, respectively.

| Fr | M | R | Ar |
|---|---|---|---|
| 101 | 2.5 | 1677 | 37 |
| 101 | 10.1 | 1677 | 37 |
| 151 | 10.1 | 1677 | 37 |

### *3.3.3 Preparation of Solids*

Because matching size distributions of particles is necessary for hydrodynamic similarity, the plastic and glass inventories are prepared with identical Particle Size Distributions (PSDs), so that they are typical of those in generic CFB combustors (Figure 3.2).

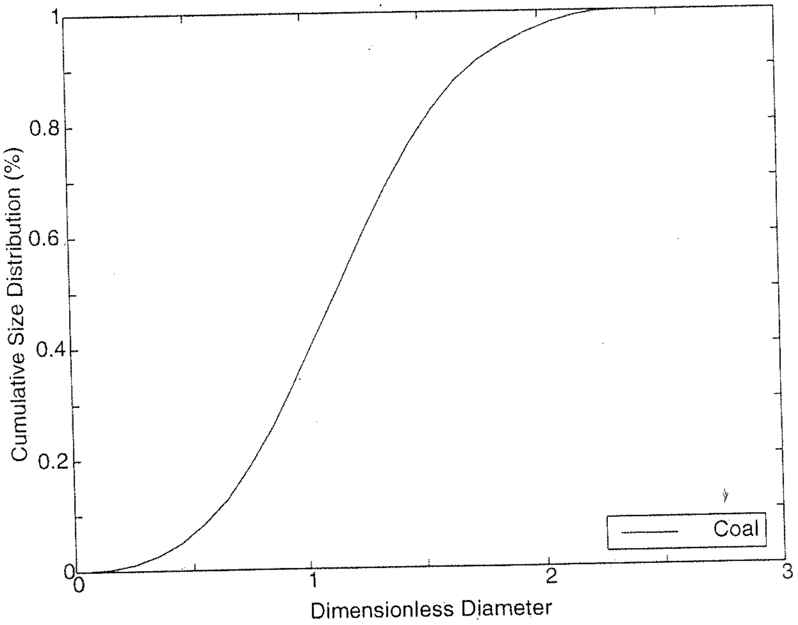

Figure. 3.2. Generic cumulative size distribution of coal in a CFB combustor.

The plastic material is a granular plastic grit manufactured by Composition Materials under the product name PG-100 X-hard. Chang (1991) conducted optical measurements to characterize its sphericity. He found $\phi = 0.69$.

The first step to achieve the desired PSD is to sort the particles by size according to the ASTM standard size categories, using a Ro-Tap siever. Table 3.5 presents the mesh opening sizes and average diameters of particles caught in each sieve, d and $d_i$, respectively.

Table 3.5. ASTM size categories and corresponding diameters.

| i | mesh # | d (μm) | $d_i$ (μm) |
|---|---|---|---|
| - | - | 425 | - |
| 16 | 45 | 355 | 390.0 |
| 15 | 50 | 300 | 327.5 |
| 14 | 60 | 250 | 275.0 |
| 13 | 70 | 212 | 231.0 |
| 12 | 80 | 180 | 196.0 |
| 11 | 100 | 150 | 165.0 |
| 10 | 120 | 125 | 137.5 |
| 9 | 140 | 106 | 115.5 |
| 8 | 170 | 90 | 98.0 |
| 7 | 200 | 75 | 82.5 |
| 6 | 230 | 63 | 69.0 |
| 5 | 270 | 53 | 58.0 |
| 4 | 325 | 45 | 49.0 |
| 3 | 400 | 38 | 41.5 |
| 2 | 500 | 25 | 31.5 |
| 1 | bottom | 0 | 12.5 |

We sort all of the plastic with the Ro-Tap siever in batch sizes of about a pound. A sieve-time of 30 minutes is sufficient to separate the particles by size. Careful cleaning of the mesh-screens of the Ro-

Tap siever ensures that the screens do not become blocked, or "blinded".

Then the prescribed PSD with $d_p$ = 150.0 μm, d = 103.5 μm is achieved by mixing the correct weight of each size category to complete the 100 lb inventory. Figure 3.3 shows the final cumulative size distributions for the glass and plastic inventories used in the experiments.

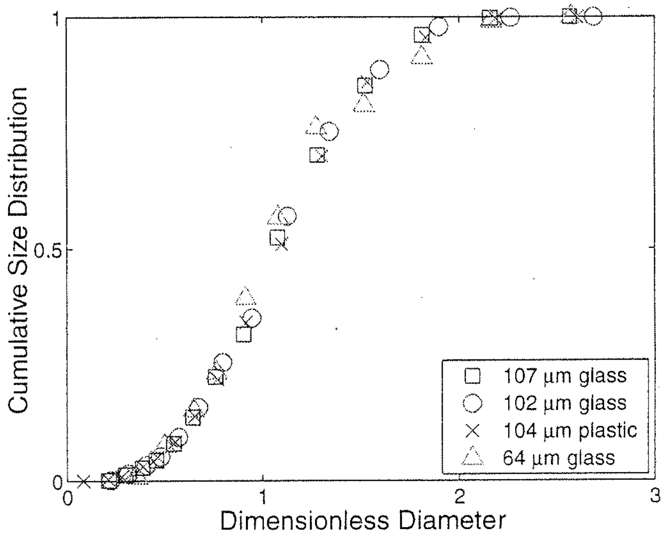

Figure. 3.3. Cumulative size distributions of the glass and plastic inventories.

The glass inventories are prepared in a manner similar to the plastics. The difference is that the glass spheres quickly block the Ro-Tap screens. For this reason, the pre-sized batches commercially available from Potters Industries Inc. (under the names Spheriglass® 1922, 2024, 2227, 2530, and 2900) were stirred, sampled, and spot-checked for size distribution. We found the batch sizes to be in excellent agreement with Chang's (1991) characterization. Then, we used the optimization procedure outlined by Chang (1991) to mix these pre-sized batches into a properly proportioned 95.8 pound inventory with the correct PSD and desired mean Sauter diameter $d_p$ = 102.0 μm.

To prepare the second batch, a 17.6 lb addition was mixed with the 102 μm glass inventory, creating a 113 pound inventory with $d_p$ = 107.0 μm. The third glass inventory was prepared in a manner similar to the 102 μm inventory, and had a mean Sauter diameter of 63.5 μm and a total weight of 95 lbs, as shown in Figure 3.3.

### *3.3.4 Preparation of Gases*

The air/He and air/$CO_2$ mixtures were produced as described by Chang (1991). Because the volume of the facility is 3.35 $m^3$, the facility was first purged with dry air for at least 10 hours at a rate of 0.5 cubic feet per minute (cfm), until the measured thermal conductivity of the gas was equal to that of dry air. Second, the valve labeled $V_{tank}$ was closed, and the gases were introduced in the desired proportions into the tank side of the CFB, using rotameters, while a vacuum pump (GAST model # 0822) removed the old gas mix from the other end of the CFB loop, that is, the other side of the $V_{tank}$ valve.

The gas was then mixed by opening the valve labeled $V_{tank}$ and running the CFB for at least 10 minutes. Finally, a sample of the mix was drawn into a sample gas bottle, and the thermal conductivity of the mix was measured using the TCD to ensure its composition.

The $SF_6/CO_2$/He mix was introduced into the facility in the same way: a bottle of $SF_6/CO_2$ (molar composition 40.4% $SF_6$, 59.6% $CO_2$) was introduced through one rotameter, while He was added through another rotameter. However, the TCD could not be used to check the composition of the gas in the CFB, since its 400 °C element would break down the $SF_6$ and produce toxic fumes. Instead, a hydrostatic pressure measurement using a relative pressure transducer, the Baratron gauge, was employed to check mixture composition, as described by Bricout (2000). In this procedure, the pressure difference between the gas in the riser and ambient was measured, both at the top and bottom of the riser column. Then, the gas density was calculated, and finally the concentration was determined, given a known combination of species. In this case, we used x % of $SF_6/CO_2$ mix and (1-x)% of the He, where x is the quantity to be inferred in the differential pressure measurement.

# CHAPTER FOUR:

# HYDRODYNAMIC AND HEAT TRANSFER PROBES

This Chapter presents the wall probes, amplifiers and data analyses for the measurements of simultaneous, time-dependent solid fraction and heat transfer coefficient, and the thermal marking experiment to measure cluster residence length.

A non-invasive combination probe (described in Section 4.1) is used to simultaneously measure solid fraction and heat transfer coefficient at the wall. The probe consists of a guarded capacitance sensor and a modified hot wire. The former uses an off-the-shelf capacitance amplifier, while the latter uses a constant-temperature hot wire anemometer controller.

In a separate measurement, a thermal marking technique is used to 'tag' passing clusters with heat, then a probe located downstream measures the fraction of heated clusters. This provides a measure of the average distance that clusters travel at the wall before they are ejected back into the core of the CFB. The downstream measurement is achieved by a very fine, slightly intrusive thermocouple located at the center of a non-invasive wall capacitance sensor (described in Section 4.2). The thermocouple signal is then conditioned by a rapid thermocouple amplifier (described in Section 4.2).

### *4.1 The Combination Probes*

We describe an instrument for local, instantaneous, non-invasive, simultaneous measurements of solid volume fraction and convective heat transfer at the wall of a CFB. The instrument combines a small platinum coil and a guarded capacitance sensor. The capacitance sensor records instantaneous solid volume fraction in the near vicinity of the wall. The coil is maintained at constant temperature by a rapid anemometer bridge circuit. The vessel is wrapped in electric heaters to avoid artificially high rates associated with developing thermal boundary layers, and to minimize conduction losses from the coil. Using a model capturing these losses, convective heat transfer rates are inferred from the power input to the coil.

In a recent review of instrumentation for circulating fluidization, Louge (1997) surveyed the principal techniques for measuring local heat flux. These belong to three principal categories. In the simplest and most common, a constant power P is supplied to the probe. If conduction losses are negligible and heating only occurs at the probe face, then measurements of the probe face temperature T and the suspension temperature $T_b$ yield the heat transfer coefficient h,

$$P = h\,A\,(T - T_b)\,, \tag{4.1}$$

where A is the exposed surface area of the probe. This technique was employed, for example, by Ebert et al. (1993) in circulating fluidized beds. Because thermal inertia limits potential excursions in T, this method is not satisfactory in suspensions where h exhibits wide and rapid variations.

The second method maintains the face temperature constant. Here, h is obtained from the power supplied to the probe. In principle, the heat transfer coefficient at constant flux differs from that evaluated at constant temperature. However, it appears that the difference diminishes with increasing solids loading (Louge et al., 1993). The probes often consist of a small platinum element, the resistance of which is a linear function of temperature. By controlling the resistance, temperature is kept constant. Wu et al. (1989) implemented this method with computer feedback control in a cold circulating fluidized bed, achieving an actual instrument response time of 45 ms. Renganathan and Turton (1989) reviewed the use of thin film heat gauges in fluidization.

The third method infers heat flux from thermocouple measurements located at regular intervals in an insulated cartridge perpendicular to the vessel wall. One end of the cartridge is mounted flush with the wall, while the other end is exposed to a hot source or cold sink. Although its thermal inertia prevents instantaneous measurements, this method is particularly convenient in industrial units (Basu and Nag, 1987).

In relatively dense vertical suspensions of fine solids, the flow consists of an ascending dilute core surrounded by a descending annulus near the wall. In the annulus, the suspension partly condenses into denser clusters separated from the wall by a thin gas film of the order of the mean particle diameter (Glicksman, 1997). Because of their relatively high solid volume fractions, the clusters generally govern the convective heat exchange with the wall. Thus, for proper interpretation, convective heat transfer should be recorded along with local solid volume fraction at a rate fast enough to capture the temporal evolution of passing clusters at typical frequencies of 1 to 20 Hz.

These measurements require several important precautions. First, the instrument should not interfere with the flow. As Lints and Glicksman (1993b) observed, protrusions as thin as one particle diameter can disturb the descending curtain of solids at the wall.

Another challenge is associated with thermal entry length. In a manner reminiscent of the growth of thermal boundary layers in single-phase fluid flow, Burki et al. (1993) showed that the wall heat transfer rate is larger at the leading and trailing edges of a heated wall surface. Therefore, small probes record abnormally high heat transfer rates (Glicksman, 1988, 1997), unless they are surrounded by guard heaters maintained at the same temperature or heat flux (Wu, 1989).

A final difficulty is associated with conductive energy losses from the instrument to the surrounding wall, which can lead to the overestimation of convective heat transfer rates. Guard heaters can mitigate these losses by keeping the wall temperature near that of the probe, a task made easier with constant temperature sensors.

In Section 4.1.1, we describe a non-invasive instrument designed to address all of these difficulties. It combines a capacitance sensor recording instantaneous solid volume fraction with a small platinum coil maintained at constant temperature by a rapid anemometer bridge circuit. Guard heaters wrapped around the vessel minimize effects of conduction losses and thermal entry length. In addition, the use of the constant temperature coil allows us to record the remaining conduction losses through independent calibrations that do not involve gas solid suspensions.

Although previous authors have described instruments combining capacitance and heat flux measurements, their designs and procedures had important limitations. Dou et al. (1992) combined a constant flux probe with a small parallel plate capacitance instrument recording solid volume fraction. However, the capacitance probe was invasive and separated from the heat sensor by 5 cm. The response times of the capacitance probe and the thermopile recording the surface temperature were 2 and 85 ms, respectively. Although Dou et al. (1992) employed guard heaters, they did not quantify the conduction losses. Lockhart et al. (1995) recorded heat flux and solid volume fractions near vertical membrane tubes on the wall of a circulating fluidized bed. Although the heat transfer surfaces were carefully mounted flush with the wall, the needle capacitance probes were invasive.

We begin with a description of the combined instrument. After outlining a strategy for recording and mitigating conduction energy losses, we show how the control system yields measurements of instantaneous heat transfer coefficients. Finally, we present typical results evaluating the response of this instrument.

### *4.1.1 Combined Instrument*

The combined instrument is sketched in Figure 4.1. A prototype version was designed and tested by Mohd. Yusof (1992). It incorporates a small platinum coil beneath the ground surface of a non-invasive capacitance probe. The latter infers the volume fraction of solids near the wall from a local measurement of the effective dielectric constant of the suspension.

Acree-Riley and Louge (1989) and Louge et al. (1996, 1997) described several capacitor designs operating upon the same principle. The probes consist of three conductors, namely the sensor, guard and ground surfaces. The processing electronics record the capacitance between the sensor and ground by supplying a 16 kHz oscillating current of constant amplitude to the sensor. Using an independent control circuit, it also maintains the guard and sensor voltages equal. Because the guard surrounds the sensor conductor everywhere except at the probe surface, its presence nearly eliminates all stray and cable capacitances.

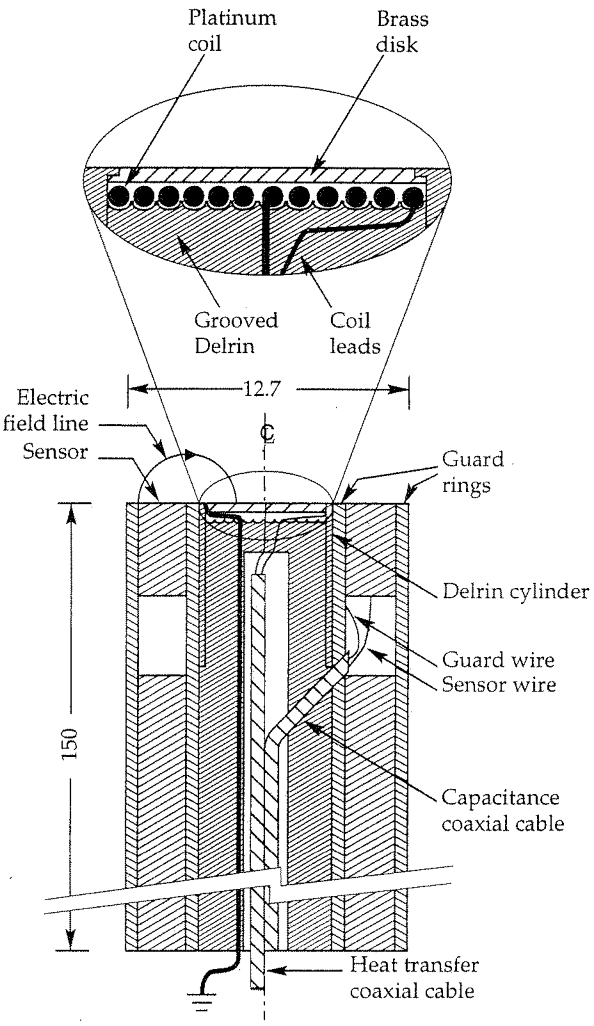

Figure 4.1. Principle of the wall capacitance and heat transfer probes. Dimensions are in mm. For the clarity of the expanded view, the brass disk connection to ground has been omitted and the dimensions are not to scale.

The output V of the electronics is the rectified guard voltage, which can follow variations of the solid volume fraction as rapid as 3 kHz. Because it is proportional to the sensor's amplitude voltage, the output is related to the capacitance C between the ground and sensing surfaces by

$$V = Q_S/GC, \tag{4.2}$$

where $Q_S$ is a system constant and G is an adjustable gain. From this equation, the effective dielectric constant of the suspension, $K_{eff}$, is obtained by forming the ratio of $V_0$ and V, the respective outputs in air and in the gas-solid mixture,

$$K_{eff} = C/C_0 = V_0/V. \tag{4.3}$$

From this accurate determination of the effective dielectric constant, the local solid volume fraction is inferred from the dielectric behavior of the suspension (Louge and Opie, 1990). For most powders with negligible conductivity, the model of Böttcher (1945) accurately captures $K_{eff}$ as a function of the solid volume fraction ν,

$$\frac{K_{eff} - K_h}{3K_{eff}} = \nu \, \frac{K_p - K_h}{K_p + 2K_{eff}}, \tag{4.4}$$

where $K_h$ and $K_p$ are, respectively, the dielectric constant of the host fluid and the particles. For a powder of unknown properties, it is generally sufficient to estimate $K_p$ from a single measurement of $K_{eff}$ at a known packing, and to interpolate $K_{eff}$ to other volume fractions using Equation 4.4.

In the instrument of Figure 4.1, the guard is located at the periphery of the probe, while the sensor is a narrow annulus of inner and outer diameters of 7.35 and 11.70 mm. By maintaining the conductive vessel wall at the guard voltage, the sensor then sheds semi-toroidal electric field lines toward the ground surface, a thin disk located at the center of the instrument. In this configuration, the sensor has a capacitance of approximately 75 femtoFarad with the ground. Its measurement volume, which is bounded by the outermost field lines emanating from the sensor, extends approximately 2 mm away from the probe face. The capacitance instrument has a resolution in solid volume fraction better than 1% (Louge et al., 1990).

In this instrument, we achieve simultaneous measurements of heat flux using a flat coil of 5.70 mm diameter located beneath a protective circular brass disk of 23 μm thickness that is also acting as a ground surface for the capacitance probe. The coil is formed by winding a 17 cm teflon-coated platinum wire of 76 μm diameter onto a thin flat helicoidal groove machined on the face of a Delrin cylinder concentric with the probe axis. The 0.28 mm thickness of the plastic cylinder and its small lip located at the coil's periphery minimize conduction between the coil and the surrounding probe. The coil is bonded to the plastic cylinder using a fast-drying superglue. The coil is then covered by conductive silicone grease and the brass disk. Because the disk has high conductivity and its periphery is insulated from the surrounding capacitance probe by a plastic cylinder, the convective heat transfer surface A is effectively equal to the disk surface area of 28.3 mm$^2$.

A hot wire anemometer bridge circuit (TSI 1750) maintains the wire at a fixed temperature by controlling its resistance

$$R = R_0 [ 1 + \sigma(T - T_0) ] , \tag{4.5}$$

where $\sigma = 3.85\text{x}10^{-3}$ °C$^{-1}$, $R_0 = 3.42\ \Omega$ and $T_0 = 0$ °C is the reference temperature. The coil is connected to the bridge with a coaxial cable of resistance $R_c = 0.209\ \Omega$. We measured $R_0$ and $R_c$ by recording the overall resistance of the probe immersed in an oven at temperatures in the range $40 \leq T \leq 110$ °C.

The probe was inserted halfway up the riser at an elevation 2.9 m above the distributor plate. Thermal guarding was achieved by wrapping the wall horizontally with 11 Watlow flexible strip heaters to elevations 24 cm above and 55 cm below the probe. The wall temperature beneath the 11 heaters was monitored with 17 independent thermocouples and manually maintained at a time-average temperature equal to that of the coil with an accuracy of ± 2 °C. To refine the spatial resolution of the heaters, 2 strips of 2.4 cm width were located immediately above and below the probe, while other strips of 4.8, 9.6, and 12 cm width constituted the rest of the thermal guard. Free convection losses were mitigated by fiberglass insulation wrapped around the strips over a vertical distance of 1.1 m.

### *4.1.2 Conduction Losses*

We model the thermal energy balance of the coil using the thermal resistance analysis sketched in Figure 4.2. In this simple steady treatment, the hot coil at temperature T dissipates the power q remaining after the total electrical power P supplied to the instrument is reduced by Joule heating in the input cable,

$$q = R\,I^2 = P - R_c\,I^2\,, \tag{4.6}$$

where I is the electrical current. We assume that the coil and its protective brass plate have a uniform temperature T. The coil loses heat by convection to the suspension and by conduction. The latter may include conduction to the colder probe stem through the wires and the probe base, as well as conduction sideways through the plastic cylinder to the surrounding wall. The wall conducts heat away from the probe, driven by forced convection in the riser.

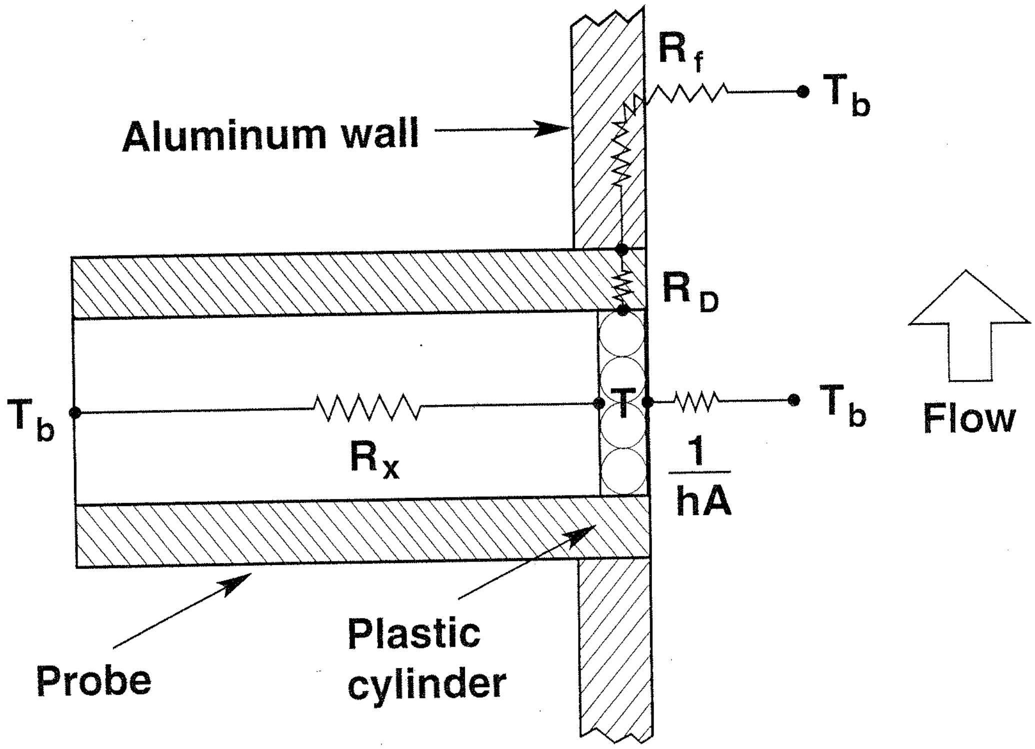

Figure 4.2. Steady lumped-parameter model of the coil heat losses. Dimensions are not to-scale with the coil and plastic cylinder enlarged. Concentric metal surfaces of the capacitance probe have been omitted for clarity.

When guard heaters are used, the power $q_W$ supplied to the heaters is adjusted so that the surrounding wall temperature $T_W$ is held equal to the coil temperature T. Then the total power to the coil, q, is transferred by convection to the flow through the sensor area A and by conduction to the probe stem,

$$q = (T - T_b)[hA + \frac{1}{R_x}], \tag{4.7}$$

where $R_x$ is the thermal resistance through the coil base and the probe stem.

In the absence of guard heaters, $q_W = 0$, the heat flow proceeds in parallel along three paths: namely, convection through the sensor face, conduction to the probe base, and conduction through the plastic cylinder followed by fin conduction through the metal wall,

$$q = (T - T_b)[hA + \frac{1}{R_x} + \frac{1}{R_D + R_f}], \tag{4.8}$$

where $R_D$ and $R_f$ are, respectively, the thermal resistances of the Delrin cylinder and the riser wall.

We estimate the thermal resistance of the plastic cylinder using a one-dimensional radial heat flow model from the coil to the surrounding cylindrical surfaces. It is

$$R_D \approx \frac{\ln(\frac{r_o}{r_i})}{2\pi k_D \Delta}, \tag{4.9}$$

where $r_i$ and $r_o$ are the inner and outer radii of the lip, $k_D$ is the thermal conductivity of the Delrin lip, and $\Delta$ is the coil thickness along the probe axis. With $r_i = 2.90$ mm, $r_o = 3.18$ mm, $k_D = 0.23$ W/mK and $\Delta = 76$ μm, we find $R_D = 841$ K/W. Note that the effective value of $R_D$ is recorded in the calibration experiments described later.

We treat the riser wall as a thin, plane, annular, axisymmetric, infinite fin of resistance

$$R_f = \frac{1}{\varepsilon_f h 2\pi \Delta r_o}. \tag{4.10}$$

Its effectiveness is

$$\varepsilon_f = \sqrt{\frac{k_a}{h\Delta}}\left(\frac{K_1(M_1)}{K_0(M_1)}\right), \tag{4.11}$$

where $K_1$ and $K_0$ are modified Bessel Functions and $M_1 = r_o (h/k_a\Delta)^{1/2}$. For this aluminum alloy wall with conductivity $k_a = 170$ W/mK, we find that $R_f$ is at least a factor of 25 lower than $R_D$, for any practical value of the convection coefficient greater than 10 $W/m^2K$, which represents a conservative lower bound for gas-solid suspensions. Thus we neglect $R_f$.

This analysis suggests a simple way to evaluate the magnitude of conduction losses. In this method, a flow of clear gas is passed through the riser at successively larger pipe Reynolds numbers Re. Because the flow is turbulent, the corresponding heat transfer rate scales as $Re^{4/5}Pr^{1/3}$ and, combining Equations 4.5 through 4.8,

$$q = \frac{P}{\left(1 + \frac{R_c}{R_0[1+\sigma(T-T_0)]}\right)} = (T - T_b)\left[\frac{kRe^{4/5}Pr^{1/3}A}{\Gamma} + \left(\frac{1}{R_x} + \beta\frac{1}{R_D}\right)\right] \tag{4.12}$$

where the shorthand notation $\beta$ is zero with guard heaters and one otherwise, $\Gamma$ is a constant having units of length, k is the thermal conductivity of the gas and Pr is its Prandtl number. Then, as Figure 4.3 illustrates, plots of P versus $Re^{4/5}$ produce straight lines of intercept equal to the conduction losses. As expected, these are proportional to the temperature difference $(T-T_b)$. Because the coil operates at constant temperature, the losses can then be subtracted directly from subsequent measurements of q in gas-solid suspensions.

Figure 4.3 also shows that guard heaters reduce these losses by nearly a factor of three. However, a weakness of our present thermal guarding system is that the constant electrical power $q_W$ manually supplied to the heaters does not follow instantaneous variations in the convective flux, which may ultimately cause fluctuations in the probe output. A measure of these fluctuations is apparent from the small scatter found in Figure 4.3 when guard heaters are employed. An onerous solution to this difficulty would be to subdivide the heaters into finer, independent, continuously adjusted constant temperature heaters of small thermal inertia.

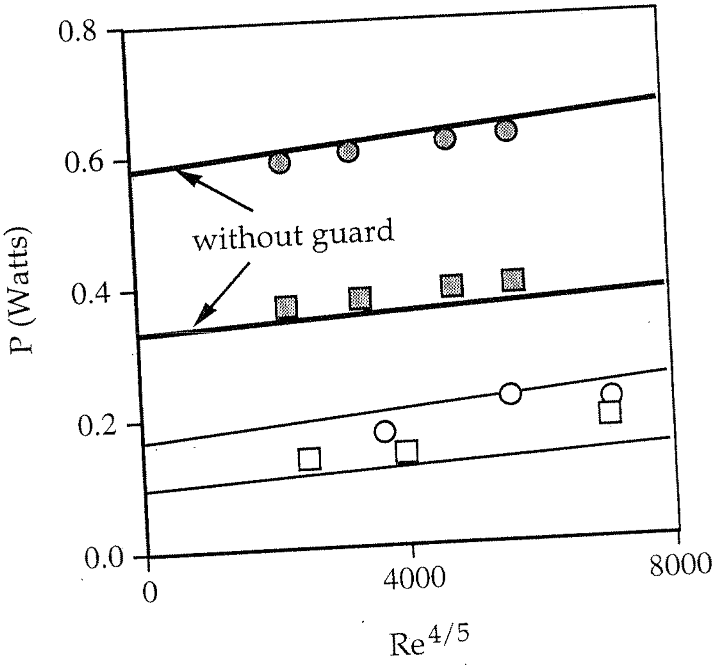

Figure 4.3. Power dissipated by the probe in a flow of ambient air (Pr = 0.712) versus Reynolds number. The squares and circles represent (T-Tb) = 23 °C and 40 °C, while open and closed symbols are obtained with and without guard heaters, respectively. Straight lines are best fits to Equation 4.12 with $\Gamma = 2.7$ m, and $1/R_X = 4.0$ mW/°C (guarded) and $(1/R_X) + (1/R_D) = 13.9$ mW/°C (unguarded wall).

### *4.1.3 Anemometer Controller Bridge*

The coil is maintained at constant temperature using the control bridge sketched in Figure 4.4. In this section, we analyze its steady and transient responses by adapting the treatment of Perry (1982) for hot-wire anemometry. There are four principal differences between our application and the latter. The first is that the resistance of the cable joining the bridge and the coil is not negligible. The second is associated with the presence of constant conduction losses for a fixed sensor temperature. The third is that, unlike anemometry where fluid velocity is inferred from the convective power lost by a thin wire using a non-linear relation, our bridge records directly the quantity of interest. The last is that the inductance of the heat transfer coil must be compensated to maintain optimum bridge stability.

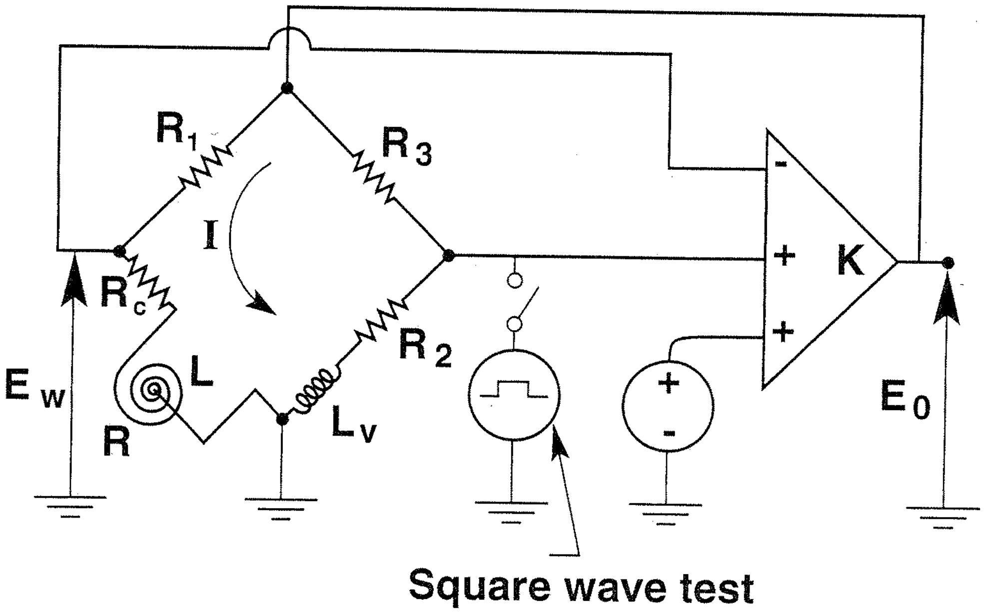

Figure 4.4. Electrical circuit of the control bridge. For the TSI model 1750 constant temperature anemometer, $R_1 = 20\ \Omega$ and $R_3 = 100\ \Omega$. The switch is closed during square wave response tests.

In this circuit, the platinum wire is connected in series with a cable of resistance $R_c$ and an effective coil inductance L (Figure 4.4). The resistor $R_2$ controls its operating temperature. To this end, we employ non-inductive resistors rated for power dissipation of 5 W; for

$(T\text{-}T_b) = 23$ °C and 40 °C, we use $R_2 = 20.98$ and 22.08 Ω, respectively. These resistors are available commercially. In the TSI 1750 controller, failure to use adequate resistances can result in significant bridge damage. To improve the temporal response of the system, an adjustable inductance $L_v$ compensates for the presence of $L_{eff}$.

We next outline how the heat transfer coefficient is derived from measured bridge voltages, taking proper account of conduction losses. The average value of the probe resistance is inferred from the voltages across the probe and the bridge,

$$\overline{R} = R_1\left(\frac{\overline{E_w}}{\overline{E_0} - \overline{E_w}}\right) - R_c, \qquad (4.13)$$

where overbars denote time averaging. Because the bridge is not balanced in general, this value of $\overline{R}$ is not necessarily equal to $R_1R_2/R_3$.

Rearranging Equation 4.12, substituting in Equation 4.6 and averaging yields

$$\overline{h} = \frac{\overline{I}^2\,\overline{R} - \left(\frac{1}{R_x} + \beta\frac{1}{R_D}\right)(T - T_b)}{A(T - T_b)}, \qquad (4.14)$$

where script quantities denote instrument "estimates" i.e., values of the heat transfer coefficient derived from direct measurements. As Figure 4.4 indicates, the time-average current through the probe is

$$\bar{I} = \frac{\bar{E}_0 - \bar{E}_w}{R_1}. \tag{4.15}$$

Substituting this into Equation 4.14, using Equation 4.13 for the time-average probe resistance, and assuming that guard heaters are used and properly balanced (β=0), we find

$$\bar{h} = \frac{\sigma R_0(\bar{E}_0 - \bar{E}_w)}{R_1{}^2 A}\,\frac{(R_1\bar{E}_w - R_c(\bar{E}_0 - \bar{E}_w))}{\left(\dfrac{R_1\bar{E}_w}{\bar{E}_0 - \bar{E}_w} - R_c - \bar{R}_b\right)} - \left(\frac{1}{R_x A}\right), \tag{4.16}$$

where $R_b$ is the coil resistance evaluated at the suspension temperature.

Like in hot-wire anemometry, the instantaneous value of the heat transfer coefficient $\hat{h}$ may be inferred from $E_0$ and $\bar{h}$. This instrument estimate thus derives from the time-dependent variations of a single voltage measurement,

$$\hat{h} = \frac{E_0{}^2\bar{R}}{(R_1 + R_c + \bar{R})^2}\,\frac{1}{A(\bar{T} - \bar{T}_b)} = \left(\frac{E_0}{\bar{E}_0}\right)^2 \frac{\bar{q}}{A(\bar{T} - \bar{T}_b)} = \bar{h}\left(\frac{E_0}{\bar{E}_0}\right)^2. \tag{4.17}$$

### *4.1.4 Tests*

In this section we discuss how the bridge is tuned for optimum performance and we present measurements under actual conditions. In the circuit of Figure 4.4, the bridge gain K and variable inductance

$L_V$ can be tuned to optimize bridge stability. To that end, we characterize the bridge response to a square wave. In this test, the bridge is perturbed by injecting a square voltage wave as shown in Figure 4.5, while the sensor is exposed to a rapid flow of clear gas. Because gas-solid suspensions are inherently unstable, the resulting signal fluctuations would make it difficult to carry out accurate square wave tests in such suspensions. In fact, the square wave must be just large enough to cause a pulse-fluctuation of $E_0$. Because our instrument exhibits a significant inductance, its response to this test resembles that of a hot film and its output has a significant dc offset. In addition, because the rapid heating and cooling induced by this test do not occur at exactly the same rate, the relaxation of the circuit to the leading and trailing edges of the square wave are not symmetrical. However, we can adjust $L_V$ and K until $E_0$ approximates the optimum response suggested by Perry (1982). Then, its relaxation time is an estimate of the system's response, as Figure 4.5 illustrates with a control resistor of 22.08 Ω.

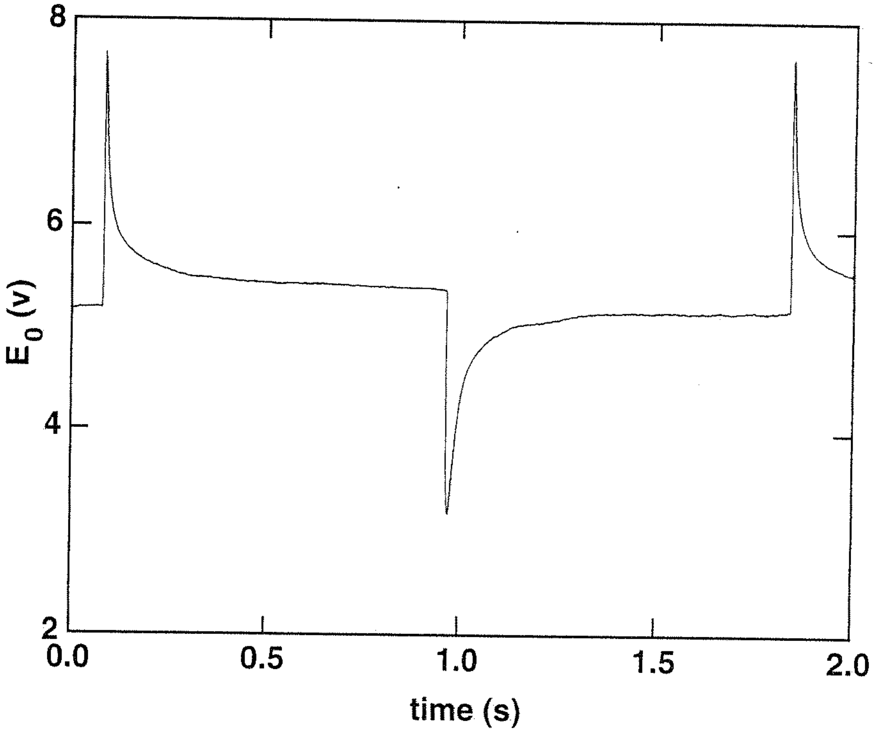

Figure 4.5. Bridge output during a square wave response test. The input square wave had an amplitude of 20 mV and a dc offset of 30 mV. The probe face was inserted flush with the inner vessel wall, while the riser was operated without solids at Re = 28,000. For this system, the time constant is approximately 20 ms.

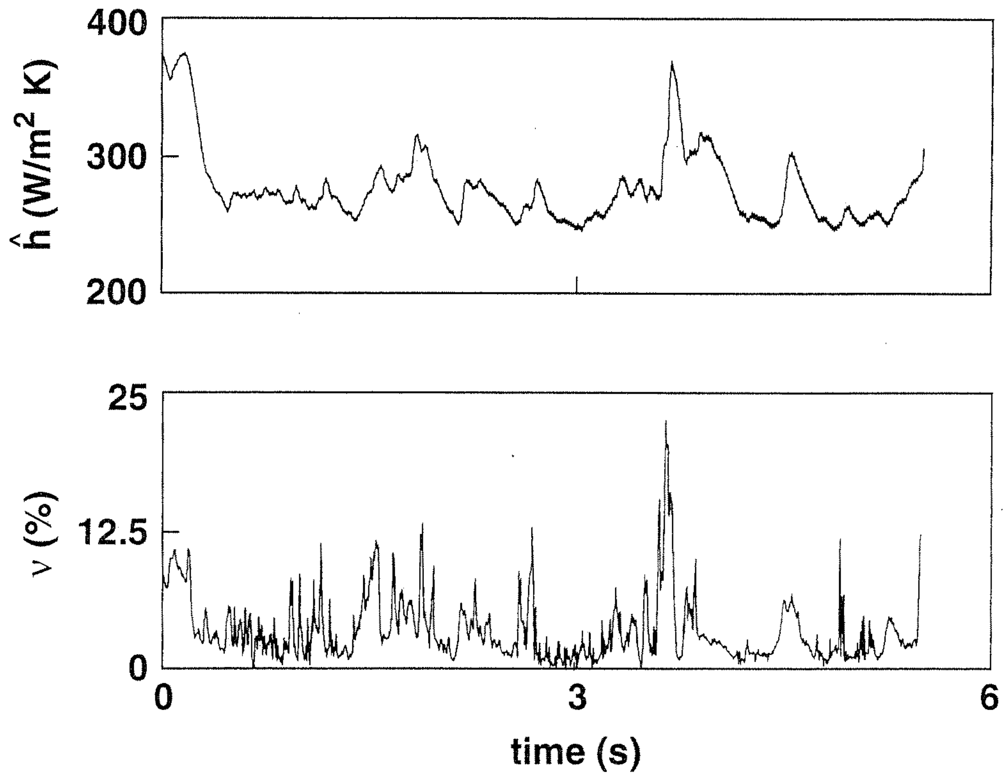

Figure 4.6. Simultaneous traces derived from the wall capacitance and heat transfer probes at a pipe Reynolds number based on superficial gas velocity of 40,200 and a loading ratio of solid and gas fluxes of 7.7.

Figure 4.6 shows a simultaneous trace of heat transfer coefficient and solid fraction recorded in the CFB facility. As expected, the simultaneous traces respond in a similar way to the passage of particle clusters, which promote a higher heat transfer coefficient through a larger volumetric heat capacity. A close comparison of the simultaneous traces reveals that $\hat{h}$ lags behind v by about 25 ms, which is consistent with results of the square wave tests.

## *4.2 The Thermal Marking System*

### *4.2.1 The Thermocouple Probe Construction*

The thermocouple probe, shown in Figure 4.7, consists of a thin thermocouple inside a 4.8 mm OD, 3.2 mm ID stainless steel (SS) tube. A ceramic 'sleeve' electrically insulates the thermocouple from the stainless steel tube. The ceramic sleeve (OD 3.0 mm, ID 1.8 mm) was first coated with thermally insulating epoxy, then inserted into the SS tube, until the end was flush with the SS tube face.

A 75 μm diameter type E (Constantan-Chromega) thermocouple was employed. This material has the advantage of yielding the highest thermoelectric emf per degree temperature difference. First the wires were threaded through the SS tube. Next, the insulation near the tips of the wires was removed, and then the wires were twisted so that the dissimilar metals were in contact once. Finally, they were spot-welded. Multiple attempts at creating a small thermocouple sensing junction confirmed that this spot-welding technique created a smaller junction than a soldering approach, where a third metal was added.

After the junction was formed, the wires were pulled back through the ceramic and SS tube until the tip of the junction protruded only 300 μm from the face of the tube. Finally, the back end of the tube assembly was sealed with a silicone adhesive (Plumber's Goop) to prevent gases from leaking out the back of the probe, and to provide strain relief for the wires.

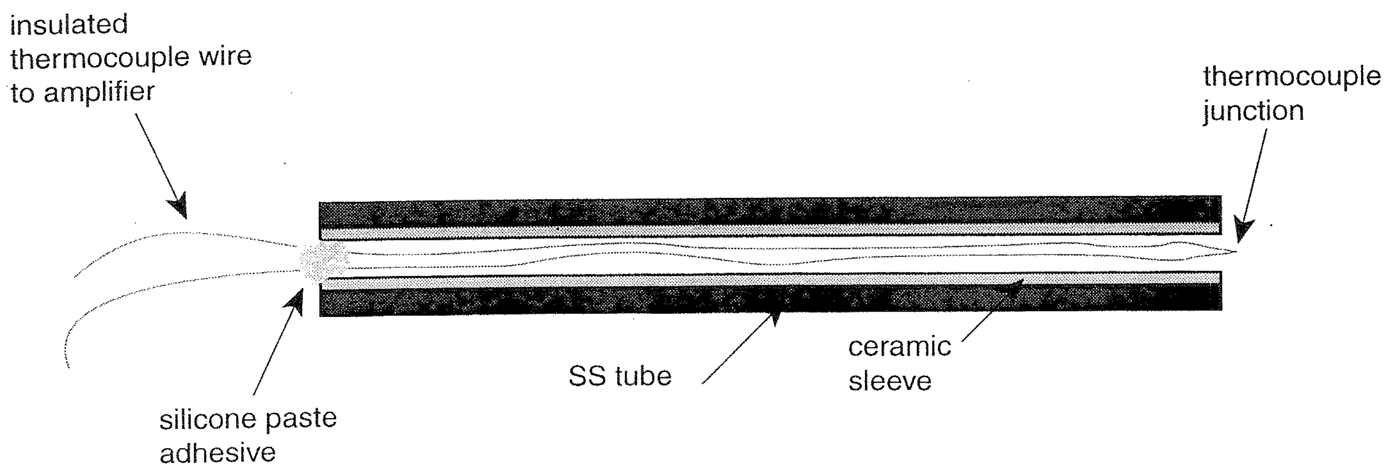

Figure 4.7. Construction details of the thermocouple probe. A layer of insulating epoxy holds the ceramic sleeve in place inside the stainless steel tube. Note that this drawing is not to scale.

### *4.2.2 The Thermocouple Amplifier*

Most off-the-shelf thermocouple amplifiers are limited by a bandwidth of about 2 Hz. Care was therefore taken to employ one fast enough to follow typical fluctuations in the CFB flow, which are generally between 0.5 to 20 Hz (Louge, 1997).

We found the monolithic IC amplifier by Analog Devices, the AD594, to have several benefits beyond other thermocouple amplifiers. See Figure 4.8 for the circuit diagram of the chip. First, it has built-in cold-junction compensation, so that an ice bath is not necessary. In addition, its differential input rejects common-mode noise voltage from the thermocouple leads. It has a frequency cutoff of 20 kHz. By adding a capacitance of 0.1 μF between pins 10 and 11, we reduced the 3 dB point to 120 Hz, thus reducing output noise above this frequency.

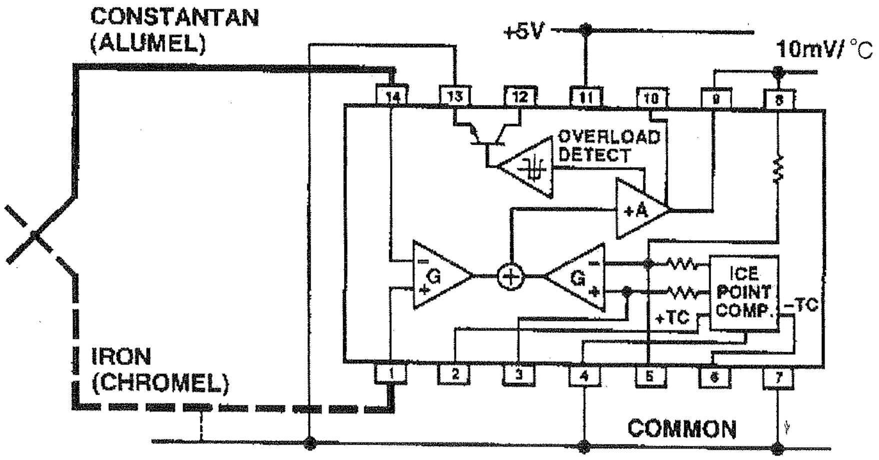

Figure 4.8. Circuit diagram of the AD594 chip by Analog Devices.

One drawback of the AD594 is that it is factory-calibrated for a type T thermocouple. Therefore, we had to use the re-calibration procedure for type E thermocouples as outlined in Analog Devices' pamphlet entitled "Monolithic Thermocouple Amplifiers with Cold Junction Compensation: AD 594/595". As a final test of the calibration, we performed an oven-calibration of the thermocouple ($30 \leq T \leq 100$ °C), with a type T thermocouple as a reference.

The AD594 allows flexibility in its power supply, accepting any DC voltage between +5 to + 30 V. With a relatively clean and steady power supply (9 V alkaline battery) and adequate shielding, this amplifier provided a good signal-to-noise ratio of between 5 and 15. We believe this to be a good S/N ratio for a time-dependent thermocouple measurement of the temperature of the passing suspension near the wall.

### *4.2.3 Requirements for the Diagnostic*

As discussed in Section 2.2.7, the cluster residence length at the wall is important for heat transfer scaling. Its measurement technique must meet the following criteria:

First, the technique should hardly disrupt the flow. This requirement will be met by our active thermal marking. In this method, clusters traveling downwards at the wall are heated, then travel below the heaters past a small thermocouple junction (inserted 300 μm, or about 3 particle diameters into the flow) that measures the suspension temperature. Because the small disruption caused by the thermocouple occurs after the residence of interest is completed, it only affects the flow minimally.

Second, the technique should record the presence of 'tagged' particles with a simple point-probe technique. This requirement will be met using a wall capacitance probe similar to that described in Section 4.1. Because this probe requires that the surrounding wall be driven with the same oscillating current as the sensor, the wall must be conductive, which precludes the presence of windows near the probe. The absence of windows also avoids the build up of electrostatic charges on the wall, which in turn make the flow more reproducible.

Finally, the marking technique should not affect the hydrodynamics of the flow. In particular, because our powders must satisfy certain density and size characteristics, the method should avoid adding any tracer particles with different properties than the bed inventory. The thermal marking experiment satisfies the above criteria, as outlined in the next section.

### *4.2.4 Set-up and Procedures*

The thermal marking experiment is relatively simple. The experimental set includes five 2.54 cm wide strip heaters wrapped around the riser, a bank of cooling water tubes located a distance $x_w$ = 5 cm below the heaters (Figure 4.9), and a detection instrument combining a capacitance probe with the thermocouple probe insert shown in Figure 4.7. The experiments are conducted in stages with different spacings $L_0$ between the heater and the detection instrument.

As outlined later, the cluster residence length is extracted from a plot of the fraction of hot, thermally marked cluster versus the spacing $L_0$.

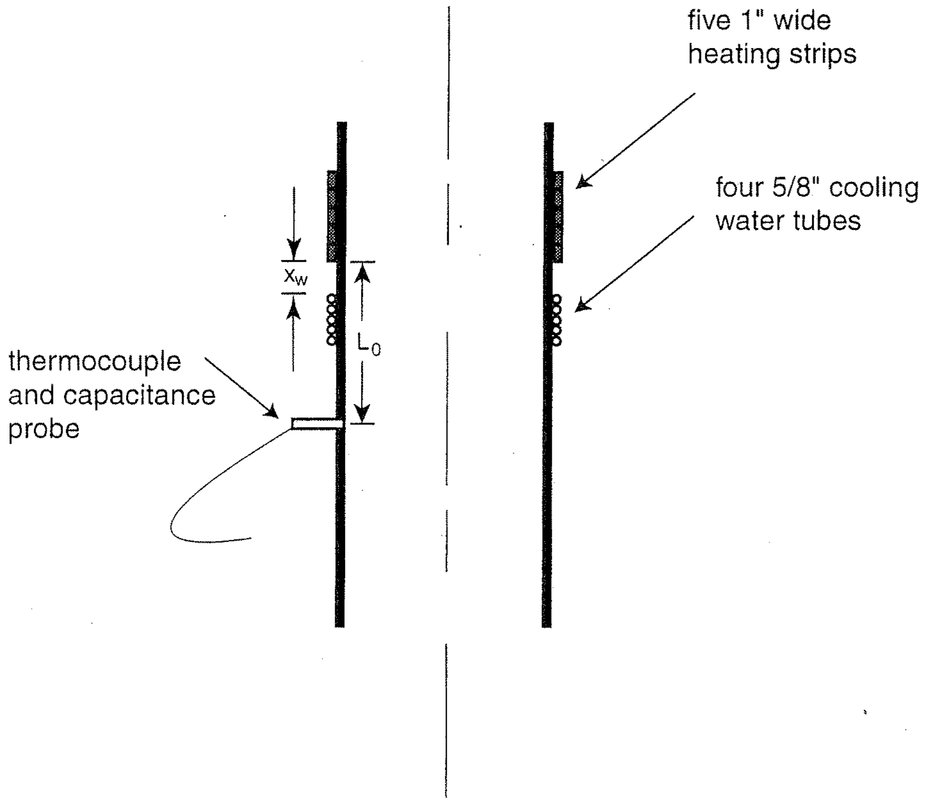

Figure 4.9. Diagram of thermal marking set-up (not to scale). Above the probe, 14 thermocouples (not shown) are attached to the outside of the riser, so that in some instances they are between the heaters and the wall.

The cooling water system consists of a submersible pump (Little Giant, 300 gph, model PE 2F34), a portable cooler, long-lasting “blue ice”, and neoprene tubing. The tubing is attached to the pump, which is placed under the water level in the cooler. The “blue ice” is added to keep the water in the cooler close to 0 °C. The tubing is wound around the riser, such that there are four ⅝" diameter coils creating a cooled strip of height approximately 2 ½". When the pump is turned on, the cold water flows through the tubing and cools the wall.

Then the heaters are turned on and their temperature is monitored using 17 type T thermocouples, each attached to the riser with Omegabond 101 thermally conductive and electrically insulating epoxy. The heater controls are adjusted until the temperature beneath the heaters is at least 90 °C.

The CFB gas flow temperature is monitored at the exit of the heat exchanger with a gauge thermometer, and also at a dimensionless riser height, z/H, of 0.3 with a type E thermocouple. Once thermal steady state is observed and the flow temperature is constant at about 15 °C, we begin to record simultaneous thermocouple and capacitance data. We acquire at least 7 traces, each 10 seconds long, at 100 Hz. The temperature profile is then recorded by hand using a multiplexer and reading from a digital voltmeter. This concludes the procedure for one stage of the thermal marking experiment, that is, for one spacing $L_0$.

The thermal marking experiment involves six successive stages at different spacings. Note that for eleven out of the twelve sets of experimental run conditions, the spacings employed ranged between 18 and 89 cm, but the first run had a minimum $L_0$ of only 10 cm. (After examining the data for the first run, we decided to increase the minimum spacing to 18 cm on future runs in order to minimize uncertainties associated with wall spacings, see discussion below.)

### *4.2.5 Data Reduction of Traces*

Two simultaneous traces are obtained from the probe at the wall. The first is the instantaneous solid fraction measured by the capacitance probe. The second is the slower measurement of thermocouple tip temperature as clusters pass in front of the probe. By analyzing the simultaneous output data from both instruments, a measure of the residence length is achieved.

Figure 4.10 is a cartoon idealizing the paths of clusters passing in front of the thermal marking apparatus. Clusters arrive at the wall and fall for a given distance before traveling back to the core. In some cases, the cluster's path crosses both the heaters and the capacitance-thermocouple probe, resulting in a measurement of a heated cluster. In other cases, the clusters arrive at the wall below the heaters, and are detected by the capacitance probe but measured as unheated by the thermocouple probe.

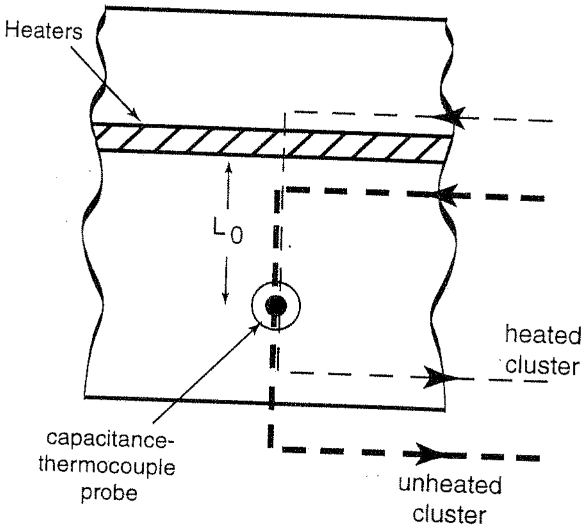

Figure 4.10. Possible cluster paths during the thermal marking experiment.

The thermal marking technique provides a means of marking the passing clusters with heat, then detecting them downstream. However, the motion and shape of real clusters may be more complex than our simple representation of Figure 4.10 suggests. For example, Figure 4.11 envisions other possible cluster paths. Because the measurement volume width of the capacitance probe is over 1 cm, while that of the thermocouple sensing junction is only about 150 μm, clusters affecting the capacitance probe may not be detected by the thermocouple sensor, thus skewing the corresponding statistics of tagged clusters.

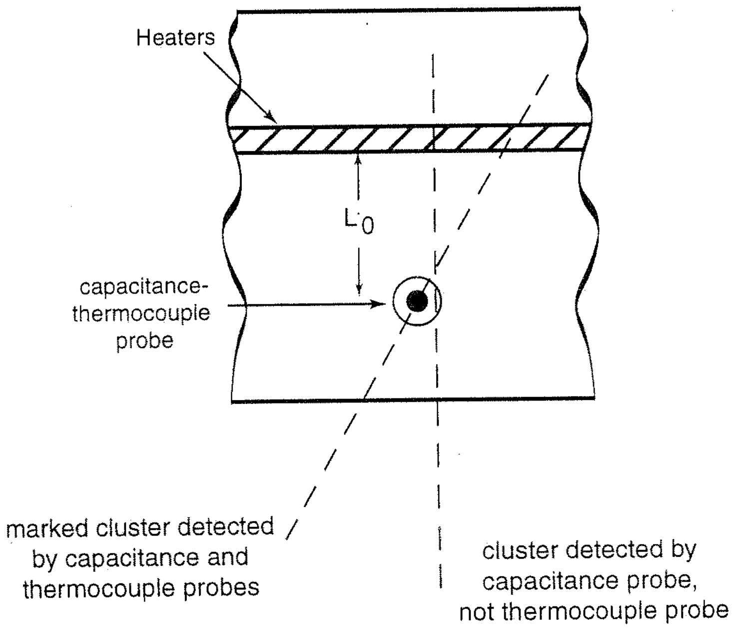

Figure 4.11. Alternative cluster paths.

Another possible difficulty is that clusters may exhibit some horizontal motion. In this case, the thermal marking experiment would measure only the vertical component of the cluster motion. Although the difference in measurement volume size of the sensors may cause occasionally uncorrelated signals, the relatively large cluster size (typically at least a millimeter wide) means that most clusters are seen by both sensors. Also, the effect occurs for all heater spacings, $L_0$, and for all run conditions, so that relative comparisons of the data are still valid.

Finally, the thermal marking technique, while simple, does not guarantee that the heat imparted to a cluster will not be entirely dissipated by the time that the cluster arrives in front of the detection thermocouple. Thus, there are practical limitations for the distance $L_0$ separating the heater and the thermocouple. However, our technique does not rely on an absolute measurement of temperature, but rather on the indication that the solids exhibit a temperature above normal. Thus, in principle, the maximum distance $L_0$ is dictated by considerations of the signal to noise ratio of the thermocouple signal.

Nonetheless, the attenuation of the tracer signal with distance makes it challenging to derive robust algorithms to analyze the data. Our original intention was to write such automatic procedures to handle the reduction of the simultaneous capacitance and thermocouple signals. Before running actual experiments, we simulated thermal signals with artificial noise and a temperature level consistent with the distance from the heater. We then normalized these to remove the corresponding effect of $L_0$ and cross-correlated the results with artificial capacitance signals. Although these simulations showed promise, a similar reduction with real temperature signals proved impractical, mainly because the complex dynamics of the facility caused the baseline temperature to drift in unexpected ways, and the noise level was higher than those anticipated in the simulations. Instead of a systematic computer analysis of signals, we chose to entrust the data reduction to the human eye.

The idea was to create precise ‘rules’ of the data analysis that allow a person to distinguish the signature of hot and cold clusters. First, the traces were divided into two categories. Those traces with spacings between the heaters and the probe that was greater than or equal to 28 cm were treated with the standard analysis. If, on the other hand, the spacing was less than 28 cm, then the trace elicited special rules for the small spacing runs. The standard and small spacing rules are detailed below, followed by Figures 4.12 and 4.13 which show typical data traces and the details of how these guidelines are implemented. Additional traces from this measurement are shown in Appendix C.

## Guidelines for Data Analysis

Notation for identifying clusters:

- Hot peak,

\+ Can't tell,

✯ Cold peak.

1. First, seek a baseline of the data. To find the baseline, look for the lowest points in the data. Our experience is that the baseline is approximately uniform among runs with the same spacing.

For standard runs, if there is one excursion lower than the others, use it as the baseline. In this case the threshold is 0.4 °C above the baseline.

For small spacing runs, if there is one excursion lower than the others, ignore it, and use the others as the baseline. The threshold is placed 0.2 °C above the baseline.

2. The time lag that temperature lags behind solids fraction is typically 0.1 to 0.3 seconds.

3. Seek peaks in the signals occuring at a rate of approximately two per second.

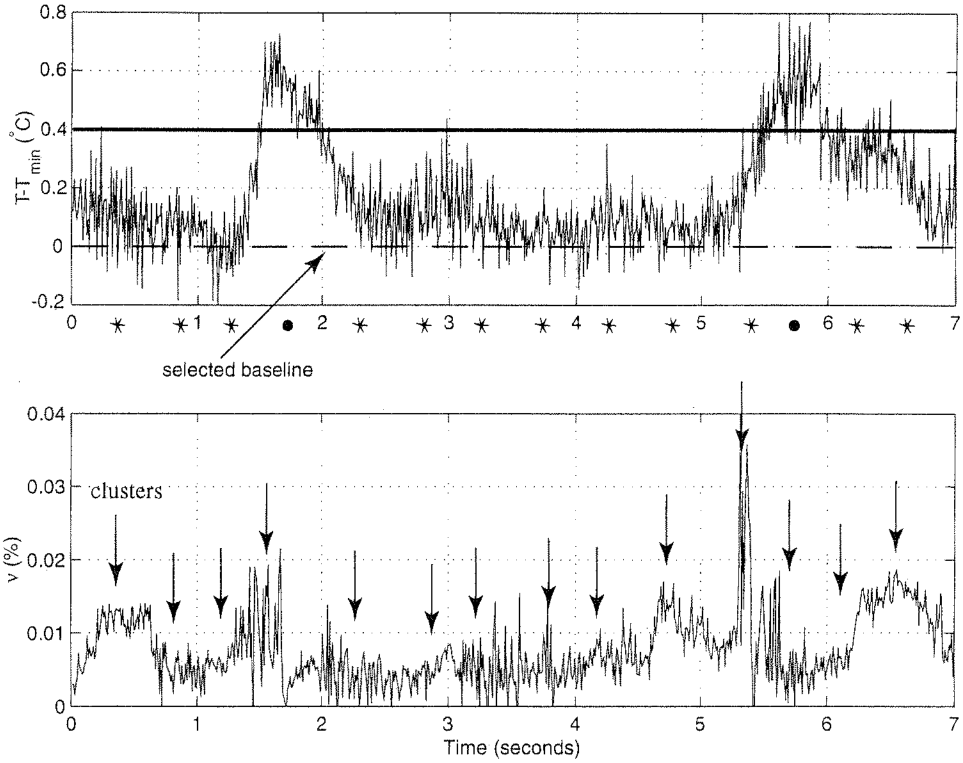

Figure 4.12. Simultaneous traces of solid fraction and measured temperature fluctuation, from the capacitance-thermocouple probe. Here, the spacing, $L_0$, was 34" (corresponding to the standard runs), the inventory was 102 μm glass, and the run conditions were $Fr^2/L = 5.5$, $U_0/U_t = 8.6$, $M/R = 0.0015$, and $R = 1675$.

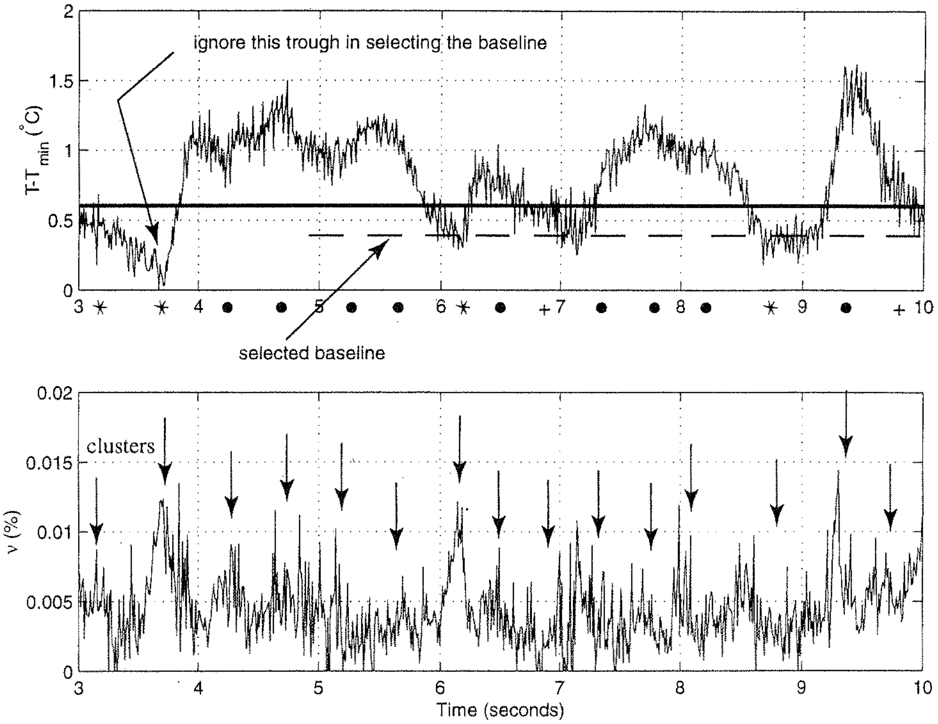

Figure 4.13. Simultaneous traces of solid fraction and measured temperature fluctuation, from the capacitance-thermocouple probe. Passing clusters are identified as hot or cold according to the guidelines on the previous page. Here, the spacing, $L_0$, was 7" (small spacing), the inventory was 102 μm glass, and the run conditions were $Fr^2/L = 5.5$, $U_0/U_t = 8.6$, $M/R = 0.0015$, and $R = 1675$.

Figures 4.12 and 4.13 illustrate typical traces from the standard and small spacing runs, respectively. As shown in Figure 4.13, the signals from the small spacing runs did not always return to a clear baseline. A likely reason for this is that a high proportion of clusters are ‘contaminated’ by the region of gradually decreasing wall temperature. These signals, which are associated with only the shorter spacings, elicit a different data reduction technique. The selected baseline is defined relative to the rest of the signal. For example, in Figure 4.13, we ignore the single trough that results from a rare, completely cool cluster. We deem that the baseline level is representative of numerous clusters that were contaminated by the higher temperature wall region. In any trace of 10 seconds, we disqualify no more than one such trough for selecting the baseline. However, note that this properly cooled cluster is indeed counted as cold.

Examination of these traces reveals that there is a higher signal to noise ratio (S/N ratio) for smaller spacing ($L_0$) runs. Figure 4.12 shows that while the 34" runs have a high enough S/N ratio for this analysis, signals from larger spacings between the heater and the probe would probably be unusable.

The guidelines provide clear identification of most heated clusters. After categorizing the clusters according to the above rules, we have about 20 identified clusters per 10 second trace. To achieve a meaningful representation of the data, we use at least 50 seconds from each spacing, which totals 360 traces for all of the run conditions.

To obtain a fraction of hot clusters representative of the data for each spacing, we tally the number of hot clusters and divide by the total number of clusters in all the traces. Finally, we compare the fraction of heated clusters as a function of the spacing between the heaters and the probe.

As a check of the cluster identification procedure, an undergraduate student independently followed the guidelines and analyzed data from three runs, or a total of 18 spacings, that is, 90 traces. This independent check yielded very close agreement to our own results, and gave residence lengths within 3% of our own values, by using the analysis described in the next subsection and shown in Section 5.2.

### *4.2.6 Analysis*

We now describe the analysis to extract the residence length of clusters from results of the thermal marking experiment. The analysis involves several assumptions. First, we assume that the flow is hydrodynamically fully developed, one-dimensional (along the axis of the riser) and at steady state. Next, we treat the heaters, the probe, and the passing clusters as points. We assume that clusters have a uniform deposition to the wall and travel downward at constant speed. Finally, we assume that all clusters passing the heater location are thoroughly heated and that clusters retain their heat long enough to be detected at the probe.

We denote the flux of clusters that arrive at a height z above the probe as F, as illustrated in Figure 4.14. Here F is a one-dimensional flux with units of number of clusters per time per length, and is constant because of our fully developed flow assumption. The number of clusters arriving per unit time between z and z+dz is Fdz.

The random variable in the analysis is the residence length of clusters, $\ell$. Physically, as explained before, this is the distance that a cluster travels near the wall before being ejected back into the core. We define a Probability Distribution Function (PDF) so that the probability for a cluster to have residence length $\ell$ is $f_r(\ell)$, and

$$\int_0^\infty f_r(\ell)d\ell = 1, \tag{4.18}$$

since the probability that a cluster has a residence length between zero and infinity is unity. Similarly, the probability for a cluster to have a residence length greater than or equal to z can be written as

$$(\text{Probability for cluster to have residence length} \geq z) = \int_z^\infty f_r(\ell)d\ell\,. \tag{4.19}$$

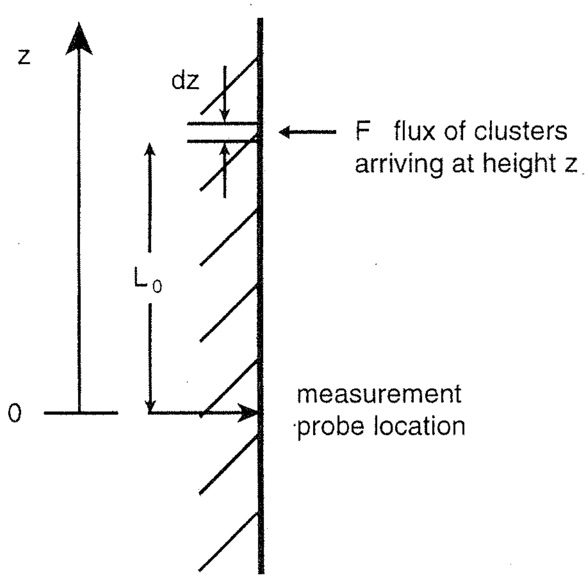

Figure 4.14. Analysis for the extraction of the residence length from the thermal marking experiment.

The next step is to calculate the number of clusters passing the probe per unit time. This will be all of the clusters arriving above the probe whose residence length is sufficient for them to stay at the wall and pass by z = 0. This is given by

$$\text{Number of clusters passing the probe per time} = \int_0^\infty \left( \int_z^\infty f_r(\ell)d\ell \right) F dz. \tag{4.20}$$

Next we seek the number of heated clusters passing by the probe per time. This quantity is obtained by selecting only clusters that arrived above z = $L_0$ in the double integral, so that

$$\text{Number of heated clusters passing the probe per time} = \int_{L_0}^\infty \left( \int_z^\infty f_r(\ell)d\ell \right) F dz. \tag{4.21}$$

Finally, the fraction of heated clusters, f, passing in front of the probe is the number of heated clusters over the total number of clusters,

$$f = \frac{\int_{L_0}^\infty \left( \int_z^\infty f_r(\ell)d\ell \right) dz}{\int_0^\infty \left( \int_z^\infty f_r(\ell)d\ell \right) dz}, \tag{4.22}$$

and is a function of the spacing between the heater and the probe, $L_0$. Equation 4.22 relates the Probability Density Function $f_r$ to the fraction of heated clusters that we measure in the thermal marking experiment, f.

The exponential decay of f with spacing suggests that

$$f_r(\ell) = \frac{1}{\lambda} e^{-\frac{\ell}{\lambda}}, \tag{4.23}$$

which yields a fraction of heated clusters of the form

$$f(L_0) = e^{-\frac{L_0}{\lambda}}. \tag{4.24}$$

Using a different thermal marking technique, Noymer (1997) also measured a similar exponential decay of $f(L_0)$. However, following a heuristic proof in his Appendix C, he derived an alternative expression for Equation 4.22, namely

$$f(\tau) = \int_{\tau}^{t_{max}} \frac{f_r(t)}{t} dt, \tag{4.25}$$

where his random variable $\tau$ represents the contact time of clusters at the wall and is simply related to our random variable for cluster residence length $\ell$ by $\ell = U_{cl}\tau$. Then, to be consistent with the observed exponential form of f, Noymer (1997) was led to postulate that $f_r$ conforms to a Gamma distribution. Because Noymer's Equation 4.25 is likely in error, his expression for $f_r$ is also questionable.

# CHAPTER FIVE:
# RESULTS

We begin by presenting axial pressure profile data in dimensionless form as an indicator of hydrodynamic similarity between runs. Then we show results of the cluster residence length as measured by the thermal marking experiment. Finally, we present trends of measured h and $Nu_d$ as a function of the ratio of time constants.

## *5.1 Pressure Profiles*

Vertical pressure profiles in the riser provide a cross-sectional representation of the hydrodynamics in the riser. As shown by Chang and Louge (1992), the appropriate dimensionless forms of static pressure and elevation are $p^+ \equiv (p-p_{top})/(\rho_p g D)$ and $z^+ \equiv z/H$, respectively. The dashed lines in the figures indicate the axial position of the heat transfer probe.

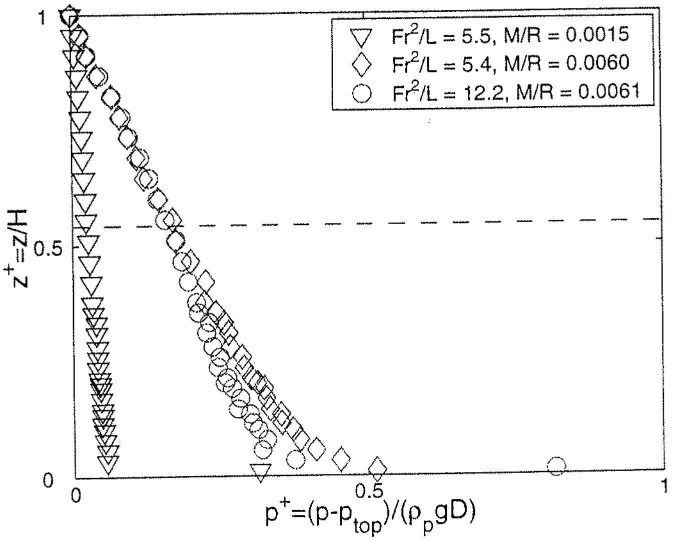

Figure 5.1. Effect of varying operating conditions with the 107 μm glass inventory and SF6/CO2/He gas mixture. See table 5.1 for the complete list of dimensionless numbers corresponding to these runs.

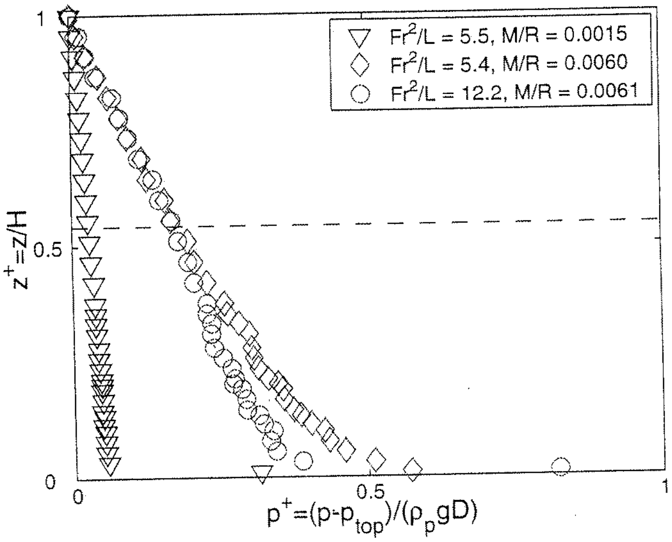

Figure 5.2. Effect of varying operating conditions with the 102 μm glass inventory and CO2/air gas mixture. See table 5.1 for the complete list of dimensionless numbers for these runs.

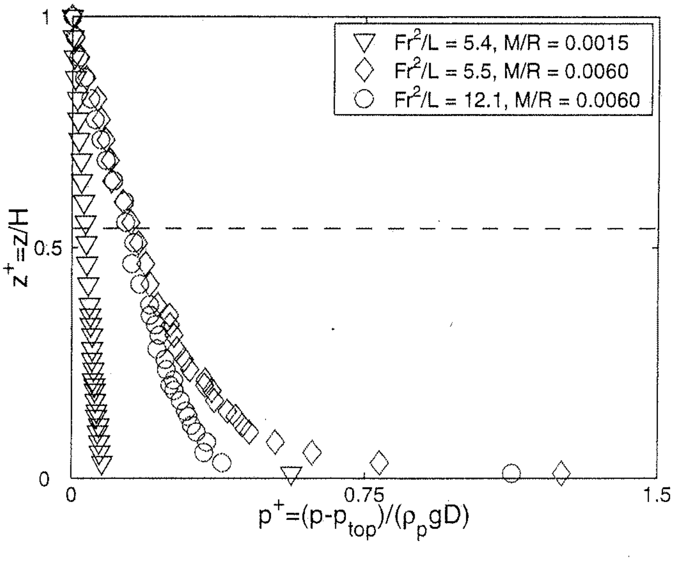

Figure 5.3. Effect of varying operating conditions with the 104 μm (hydrodynamic diameter) plastic inventory and air/He gas mixture. See table 5.1 for the complete list of dimensionless numbers for these runs.

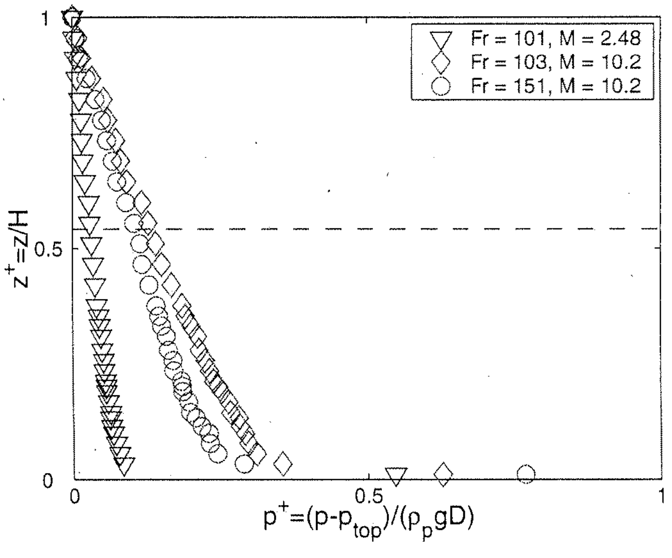

Figure 5.4. Effect of varying operating conditions with the 64 μm glass inventory and $CO_2$/air gas mixture. See table 5.1 for the complete list of dimensionless numbers for these runs.

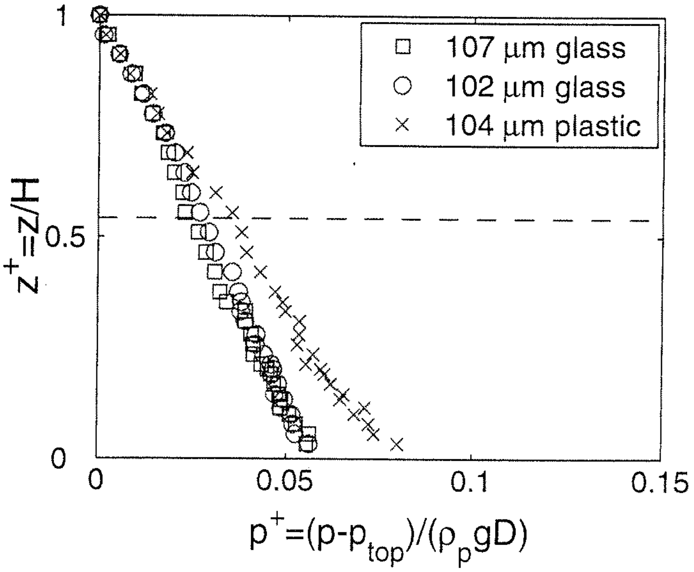

Figure 5.5. Dimensionless pressure profiles of three runs matched using the reduced set. These are the low Fr, low M runs.

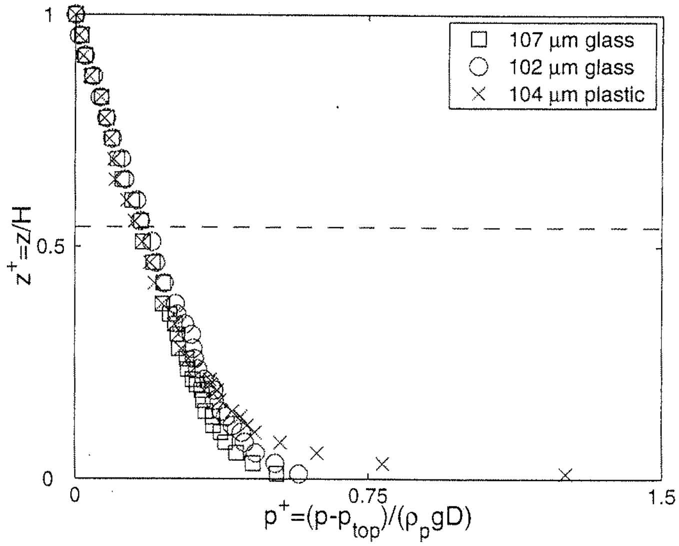

Figure 5.6. Dimensionless pressure profiles of three runs matched using the reduced set. These are the low Fr, high M runs.

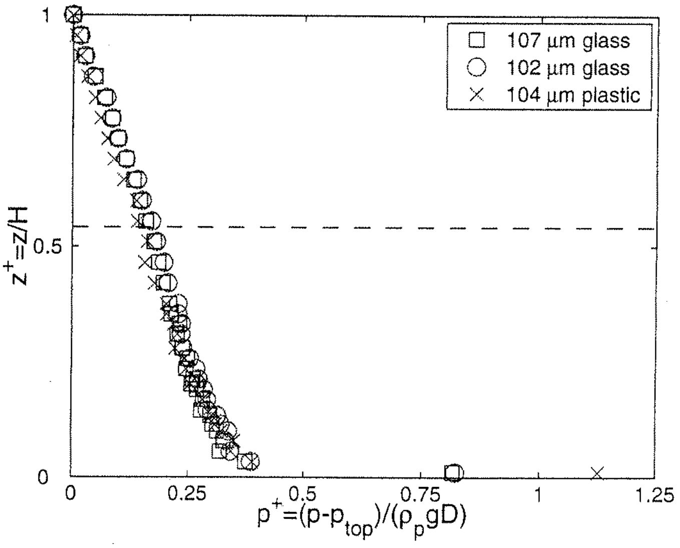

Figure 5.7. Dimensionless pressure profiles of three runs matched using the reduced set. These are the high Fr, high M runs.

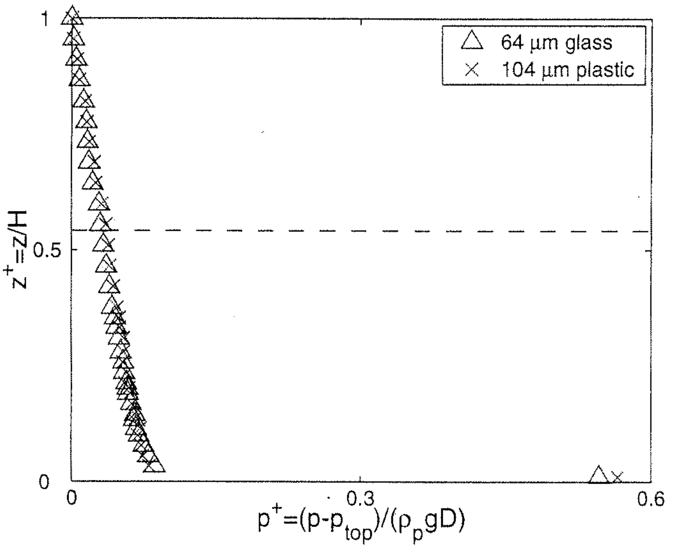

Figure 5.8. Effect of varying L, but holding the other full set numbers constant. See table 5.1 for all the dimensionless numbers of these low Fr, low M runs.

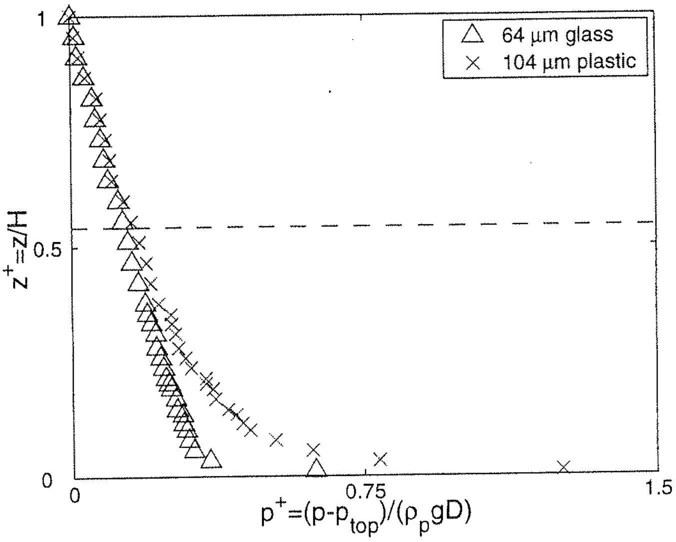

Figure 5.9. Effect of varying L, but holding the other full set numbers constant. See table 5.1 for all the dimensionless numbers of these low Fr, high M runs.

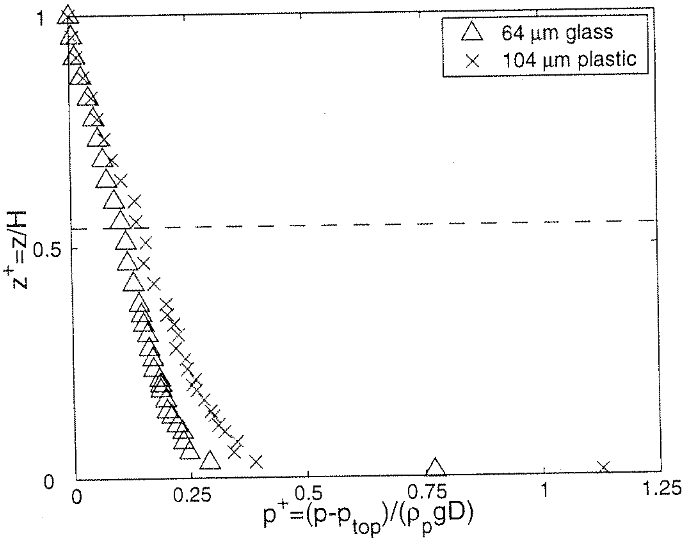

Figure 5.10. Effect of varying L, but holding the other full set numbers constant. See table 5.1 for all the dimensionless numbers of these high Fr, high M runs.

Figures 5.1-5.4 illustrate the effects of varying $Fr^2/L$ and M/R (or Fr and M) on the pressure profiles. For all material sets, the low Fr, low M runs have the least solids hold up in the riser, and their pressure is fully developed from very near the riser base. The other two runs show that increasing M causes a dramatic increase in solids hold up, but increasing the Froude number tends to stabilize the profile, and assist in the overall transport of solids out of the riser. Also, the high M runs show the much larger acceleration region at the base of the riser.

Figures 5.5-5.7 demonstrate the overall hydrodynamic similarity of runs matched using the reduced set of numbers. Figure 5.5 shows excellent agreement between the glass inventory runs, but a little deviation compared to the plastic runs, especially at the base of the riser. Figures 5.6 and 5.7 show relatively robust agreement between the three runs. However, there is some deviation at the base of the riser in the acceleration region for the low Fr, high M runs, where the profiles are the least stable.

Figures 5.8-5.10 illustrate the effect of varying L, while holding R, Ar, Fr and M constant. These experiments allow us ~~allows us~~ to investigate the effect of scale on the hydrodynamics. Figure 5.8 clearly shows that there is little effect of L on the pressure profiles at low Fr and low M. So these runs are quite similar.

Figure 5.9 shows that varying L at low Fr and high M has a strong impact on the suspension, with the plastic going to incipient collapse more quickly. However, at the probe location, the dimensionless pressure profiles are nearly the same. Figure 5.10

shows that increased deviation between the profiles occurs at high Fr and high M. The collapse of the plastic now extends above the probe location. The deviations of the pressure profile observed with the plastic powder under low Froude, low loading conditions (Figure 5.5) are consistent with the previous observations of Bricout. For the plastic powder, Bricout (2000) also noticed instabilities in the suspension at the riser base. From a simple model of the flow acceleration near the distributor, Bricout (2000) speculated that the instabilities are directly responsible for the higher acceleration region with the plastic powder.

Table 5.1. Dimensionless Numbers for All Runs

| Operating Conditions | solid inventory | Full Set | | | | Reduced Set | | | |
|---|---|---|---|---|---|---|---|---|---|
| | | L | Ar | Fr | M | R | $U_0/U_t$ | $Fr^2/L$ | M/R |
| Low Fr, low M runs | 107 µm | 1840 | 140 | 100 | 2.50 | 1675 | 5.8 | 5.5 | 0.0015 |
| | 102 µm | 1930 | 153 | 103 | 2.52 | 1675 | 5.8 | 5.5 | 0.0015 |
| | 104 µm | 1902 | 37 | 101 | 2.50 | 1678 | 5.8 | 5.4 | 0.0015 |
| | 64 µm | 3102 | 37 | 101 | 2.48 | 1675 | 9.7 | 3.3 | 0.0015 |
| Low Fr, high M runs | 107 µm | 1840 | 140 | 101 | 9.95 | 1675 | 5.9 | 5.6 | 0.0059 |
| | 102 µm | 1930 | 153 | 102 | 10.1 | 1675 | 5.8 | 5.4 | 0.0060 |
| | 104 µm | 1902 | 37 | 102 | 10.1 | 1678 | 5.8 | 5.5 | 0.0060 |
| | 64 µm | 3102 | 37 | 103 | 10.2 | 1675 | 9.9 | 3.4 | 0.0061 |
| High Fr, high M runs | 107 µm | 1840 | 140 | 149 | 10.2 | 1675 | 8.6 | 12.1 | 0.0061 |
| | 102 µm | 1930 | 153 | 154 | 10.2 | 1675 | 8.7 | 12.2 | 0.0061 |
| | 104 µm | 1902 | 37 | 152 | 10.1 | 1678 | 8.6 | 12.1 | 0.0060 |
| | 64 µm | 3102 | 37 | 151 | 10.2 | 1675 | 14.5 | 7.3 | 0.0061 |

## *5.2 Residence Length*

The thermal marking technique maintains a region of the riser at a high temperature to transfer heat to passing clusters. Figure 5.11 shows the steady state temperature profile of the riser wall created by judicious application of heaters and cooling water wrapped around the riser. The dark and white rectangles indicate the positions of the heaters and cooling water coils, respectively.

The wall beneath the heaters is labeled the “heat zone”. Here the temperature of the wall rises over 90 °C above ambient to communicate heat to the descending clusters. Although the wall beneath the “heat zone” is cooled, conduction through the metallic riser blurs the lower edge of the heat zone and, consequently, the distance $L_0$ is not precisely defined. Clearly, the relative uncertainty in $L_0$ is greater when $L_0$ is small. Thus, to limit this uncertainty, we employ a cooling region of sufficient height, and we prudently avoid measurement with $L_0$ below 18 cm.

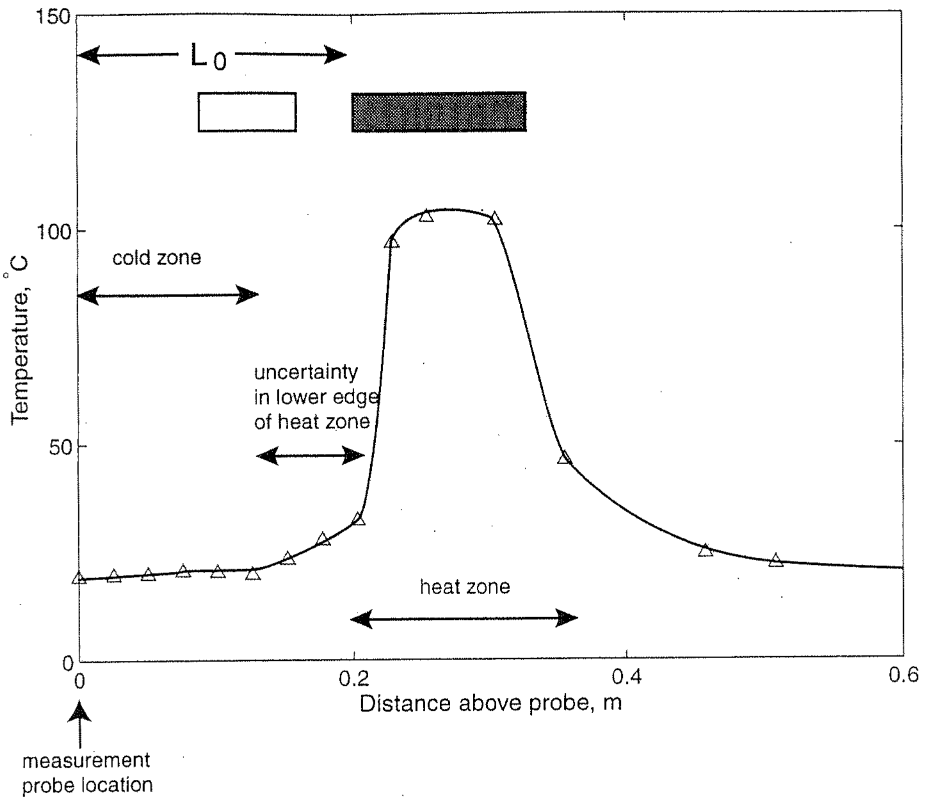

Figure 5.11. Temperature profile along the riser wall at the smallest heater spacing for these runs. The data are from thermocouples attached to the riser, and illustrate the heated zone required for thermal marking. The curve is a visual fit. The data is typical of the temperature profiles, and is taken from 104 µm plastic runs at high Fr and high M. Since the spacing $L_0$ for this run is 20 cm, the data reduction for this trace follows the rules for the small spacing runs.

The wall temperature profile shown in Figure 5.11 exhibits several interesting features. Above the heaters, the exponential profile is characteristic of the temperature of an infinite fin immersed in a medium of constant bulk temperature and heat transfer coefficient. Below them, the presence of the cooling water increases the temperature gradient under the heated zone. This corresponds to the steeper sinh-shaped temperature profile that is created when both ends of a fin are held at constant temperature.

Figure 5.12 displays measured temperature profiles of the riser wall for several values of $L_0$, but with the same CFB run condition. As expected, the temperature profiles are similar in shape, but shifted along the abscissa.

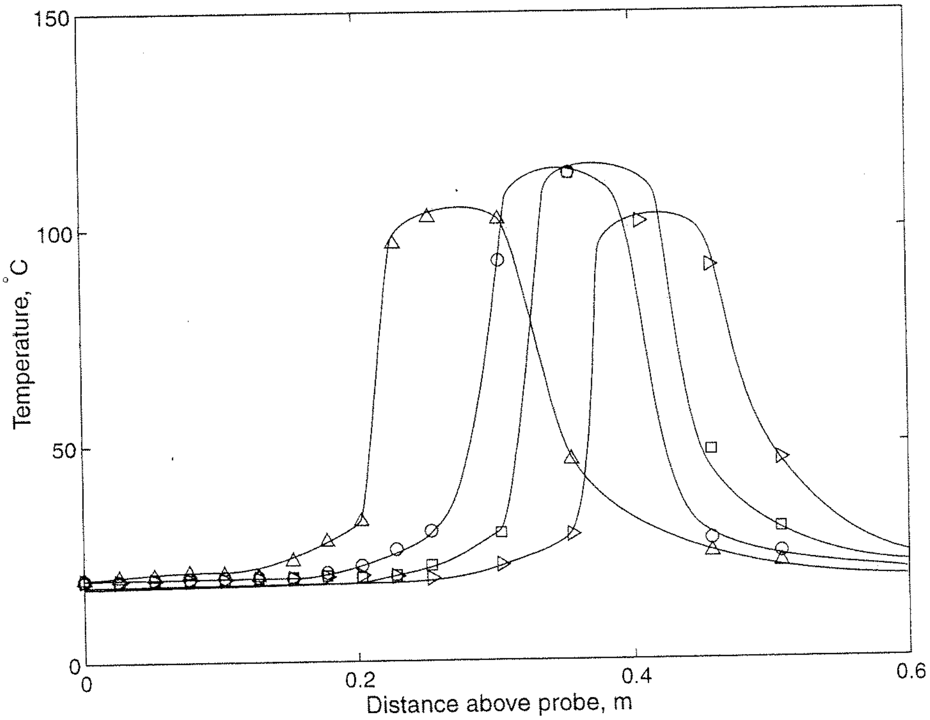

Figure 5.12 Temperature profiles along the riser wall for the four closest nominal heater locations from the probe: 20 and 26 cm (small spacing runs) and 31 and 36 cm (standard runs). All profiles are from 104 μm plastic runs at high Fr and high M. The curves are visual fits.

To extract the residence length of clusters at the wall, we follow the procedure of Section 5.3. We first plot the measured fraction of heated clusters versus the nominal spacing between the probe and the heaters.

Figure 5.13 shows the data, and an exponential fit to $e^{-z/B}$, where B is a characteristic length of the decay. The data gathered in this way from all runs fit exponential curves well. To obtain a robust measure of the residence length, we seek a measure of the exponential decay. Figure 5.14 shows a plot of the natural log of the fraction of heated clusters versus the nominal spacing between the probe and the heaters. Then the slope of this figure is related to the length $\lambda$. Because this method relies on the slope but not the y-intercept, it yields a more robust measure of the residence length. In particular, this method avoids problems associated with the uncertain location of the origin due to the blurring of the wall temperature near the lower edge of the heaters (shown graphically in Figure 5.11).

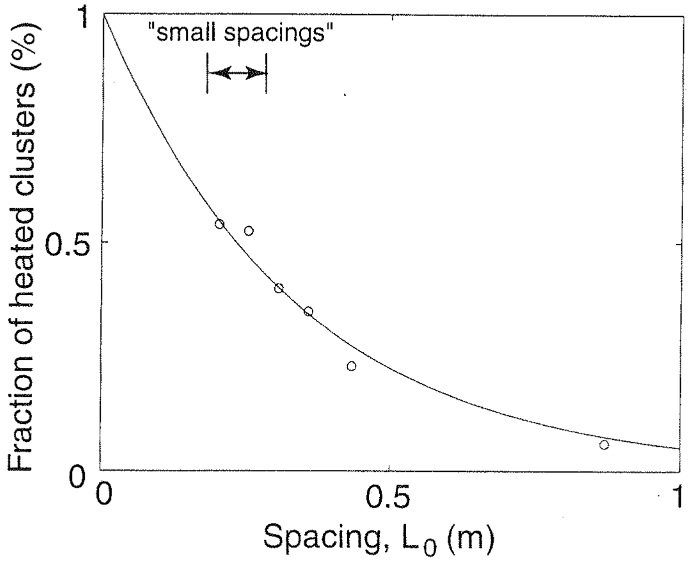

Figure 5.13. Fraction of heated clusters versus the heater spacing for 107 μm glass low Fr and low M run. The region of "small spacings" shown in this figure elicits a special set of rules to define the temperature baseline, as described in this section.

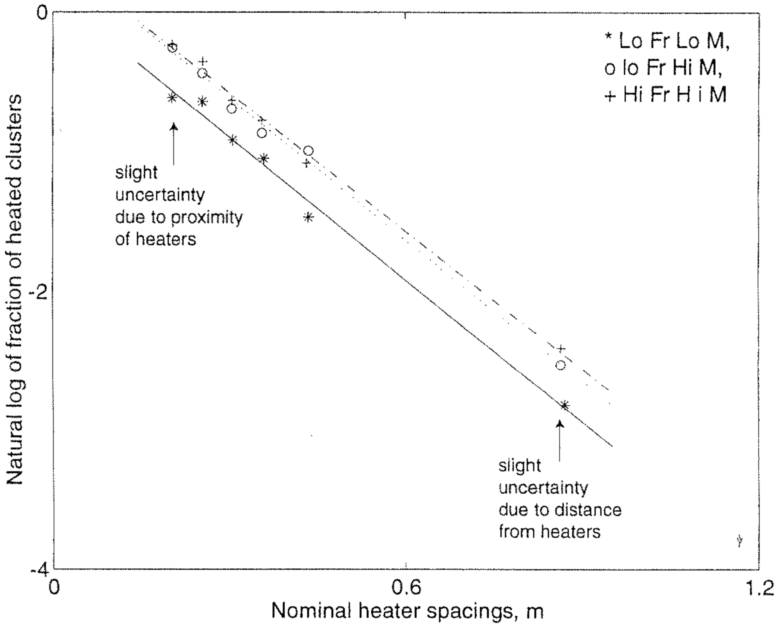

Figure 5.14. Natural log of fraction of heated clusters versus the heater spacing for 107 μm glass runs. Lines are least-square fits to the data.

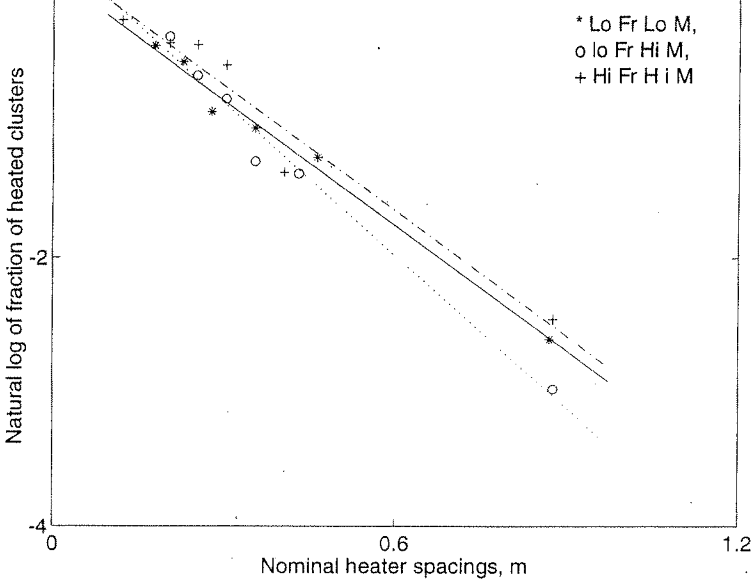

Figure 5.15. Natural log of fraction of heated clusters versus the heater spacing for 102 μm glass runs. Lines are least-square fits to the data.

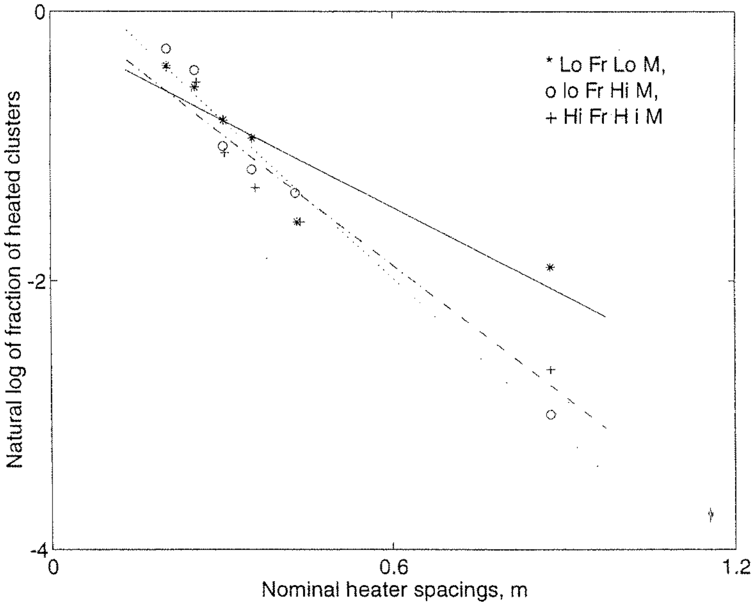

Figure 5.16. Natural log of fraction of heated clusters versus the heater spacing for 104 μm plastic runs. Lines are least-square fits to the data.

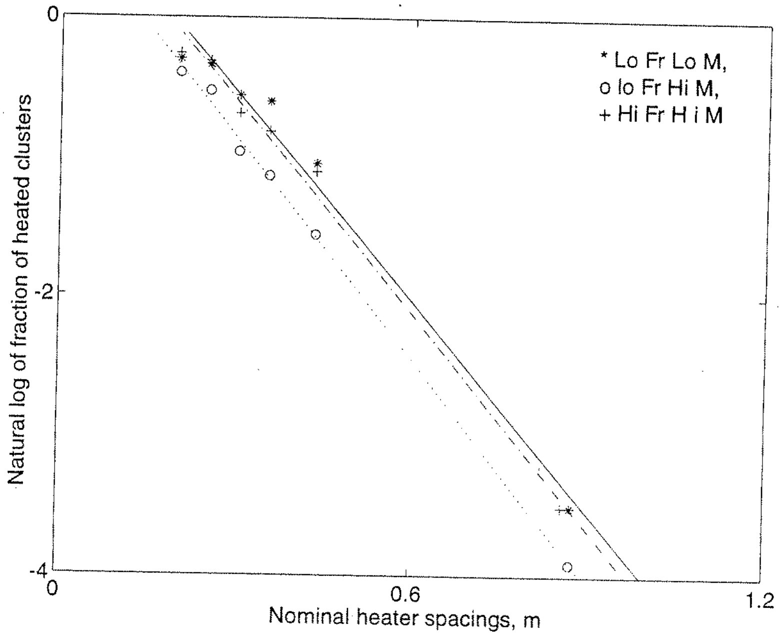

Figure 5.17. Natural log of fraction of heated clusters versus the heater spacing for 64 μm glass runs. Lines are least-square fits to the data.

Using the procedure outlined above, we obtained representative measurements of the residence length, λ, for each run. Table 5.2 summarizes the results for all run conditions. The experiments using the first three material sets, labeled as experiments 1 through 3 in Table 3.1, are the runs matched via the reduced set. From Table 5.2 it is clear that the measured residence length λ is roughly constant over these runs. The only significant deviation is with the low Fr and low M run of the 104 μm plastic, which also exhibited substantially different pressure profiles (Figure 5.5). We believe that these changes of the pressure profiles and λ for this run condition are associated with instabilities of the plastic suspension in the lower riser under these operating conditions. Bricout (2000) noted a comparable effect for similar operating conditions with the plastic material. Because the corresponding residence length λ differed substantially from those measured in the other runs with matched hydrodynamics, it is clear that the thermal tagging measurement technique does not always yield the same result, an observation that can only lend confidence to its validity.

Table 5.2. Measured residence length results.

| Solids | Operating Conditions | Measured λ (m) |
|---|---|---|
| 107 µm glass<br>L = 1840 | $Fr^2/L = 5.5$, $M/R = 0.0015$ | 0.29 |
| | $Fr^2/L = 5.6$, $M/R = 0.0059$ | 0.30 |
| | $Fr^2/L = 12.1$, $M/R = 0.0061$ | 0.30 |
| 102 µm glass<br>L = 1930 | $Fr^2/L = 5.5$, $M/R = 0.0015$ | 0.32 |
| | $Fr^2/L = 5.4$, $M/R = 0.0060$ | 0.26 |
| | $Fr^2/L = 12.2$, $M/R = 0.0061$ | 0.32 |
| 104 µm plastic<br>L = 1902 | $Fr^2/L = 5.4$, $M/R = 0.0015$ | 0.46 |
| | $Fr^2/L = 5.5$, $M/R = 0.0060$ | 0.25 |
| | $Fr^2/L = 12.1$, $M/R = 0.0060$ | 0.31 |
| 64 µm glass<br>L = 3100 | $Fr^2/L = 3.3$, $M/R = 0.0015$ | 0.20 |
| | $Fr^2/L = 3.4$, $M/R = 0.0061$ | 0.19 |
| | $Fr^2/L = 7.3$, $M/R = 0.0061$ | 0.20 |

The last three runs in the table, the 64 μm glass runs, were fully matched to the 104 μm plastic (by Ar, Fr, M and R) except for the effect of scale, given by the ratio of bed to particle diameter L, which was increased by about 39%. The smaller diameter glass runs with 64 μm particles had a measured residence length that was lower than the others by approximately 33%, as shown in Figure 5.15. Based on these observations, we suggest that the residence length of clusters at the wall scales with particle diameter, d.

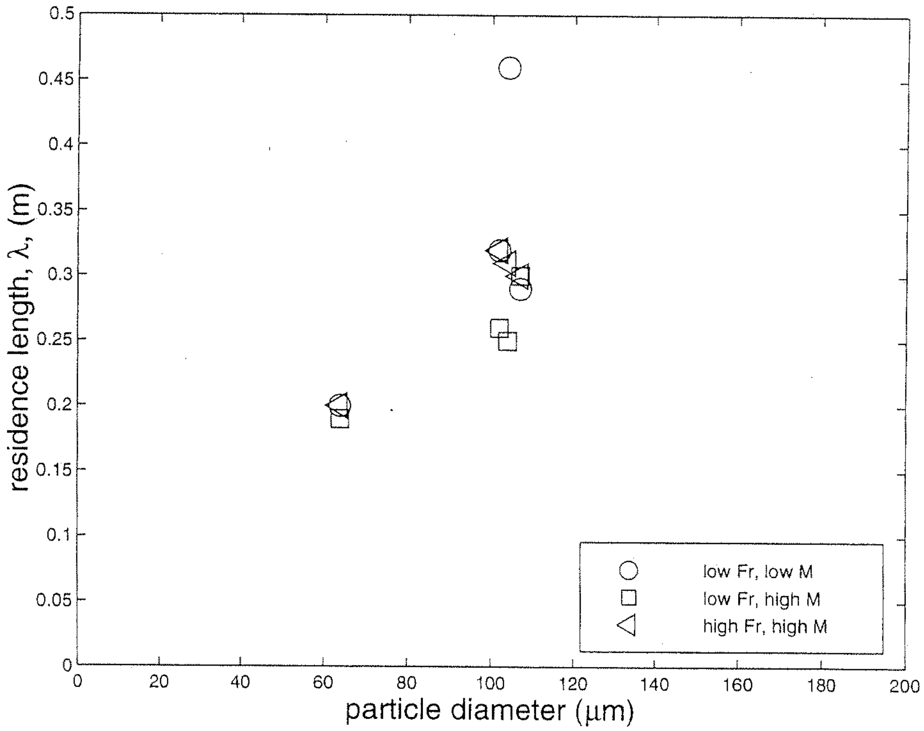

Figure 5.15. Measured cluster residence lengths from the thermal marking experiment.

Noymer (1997) measured the residence time of clusters at the wall using a different thermal technique. He found a trend of residence length increasing with R, across runs in which both R and L were varied. For this reason, it is difficult to isolate the dependence of residence length from these runs.

In the same study, Noymer ran experiments that were hydrodynamically similar via the reduced set, and he found a slight trend of residence length increasing with particle diameter.

In summary, our suggestion that residence length scales with particle diameter agrees with Noymer's finding and clarifies the possible scaling dependence.

The apparent insensitivity of our cluster residence length measurements to operating conditions was somewhat surprising. The correlation by Wu et al. (1991), Equation 2.37, suggested that runs with different $\rho_{susp}$ could yield varying residence lengths. Yet, runs that were matched via the reduced set exhibited substantial variations in cross-sectional solid concentration, as shown in the pressure profiles, but did not exhibit a significant change in the residence length.

It is interesting to note that Noymer's measurements of residence length (1997) revealed a similar insensitivity to operating conditions.

### *5.3 Fractional Wall Coverage*

The fractional wall coverage, described in Section 2.2.7, is a critical input parameter for the phenomenological model represented by Equation 2.33. Since we measure the time-dependent solid concentration using our combination probe, we are able to extract the fractional wall coverage, $f_h$, from the data obtained from each run condition.

To estimate the fractional wall coverage, Lints and Glicksman (1993) defined clusters using an absolute cutoff of 5% local solid volume fraction at the wall. They then calculated $f_h$ by dividing the time when clusters are present by the total time of the trace. Figure 5.19 shows the fractional wall coverage inferred from our runs matched with the reduced set, using that cutoff. Clearly, this absolute cutoff yields very low values of $f_h$ for the most dilute runs. Similarly, a 1.5% cutoff yields a low value of $f_h$ (Figure 5.20). Clearly, neither of these absolute cutoffs provide a consistent method valid for the range of loadings investigated here. In particular, these two cutoffs are so large that virtually no clusters are detected in the most dilute runs, although it is evident that they exist there, too, as shown in the data traces of Appendix C.

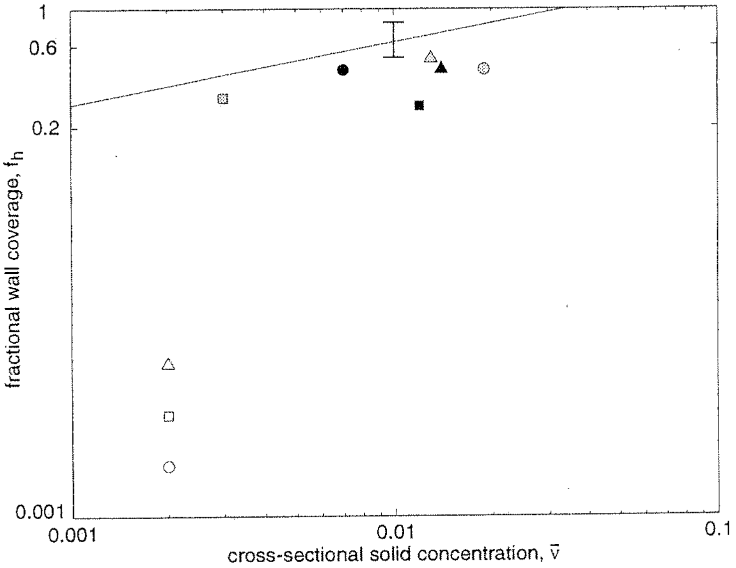

Figure 5.19. Fractional wall coverage determined by an absolute cutoff of 5% versus the cross-sectional solid concentration obtained from the pressure profiles. The line is the model of Lints and Glicksman (1993). White, gray, and black symbols are for the low Fr low M runs, low Fr high M runs and high Fr high M runs, respectively. Squares, circles and triangles are for the glass 107 μm, glass 102 μm, and plastic 104 μm runs, respectively.

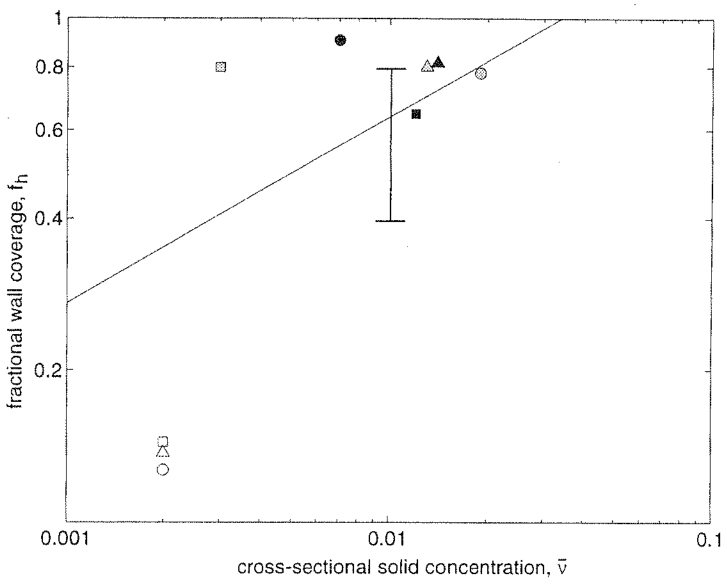

Figure 5.20. Fractional wall coverage determined by an absolute cutoff of 1.5% versus the cross-sectional solid concentration obtained from the pressure profiles. The line is the model of Lints and Glicksman (1993). The symbols are defined according to the caption of Figure 5.15.

Instead, because clusters are present even in the most dilute runs, it is more consistent to employ a relative means of defining them. Figure 5.21 shows the resulting $f_h$ when clusters are defined as having local solid fractions above the mean solid fraction measured at the wall. Because clusters rise and fall quickly, the resulting measure of $f_h$ is now relatively insensitive to the actual threshold, as long as the latter is positioned to capture most clusters. With this relative measure, it is evident that the fractional wall coverage is about 40% for all runs, except the data with the largest excursion from the mean, namely, the plastic low Fr and low M run, denoted by the white triangle in Figure 5.21. In Figures 5.16 to 5.18, the line indicates the model of Lints and Glicksman (1993) and the error bar represents the distribution of the data from the seven investigators mentioned in Section 2.2.7. Our data in Figure 5.21 agrees well with their model. Overall, we observe that, while the fractional wall coverage is relatively constant, the solid volume fraction in clusters depends primarily on solid loading.

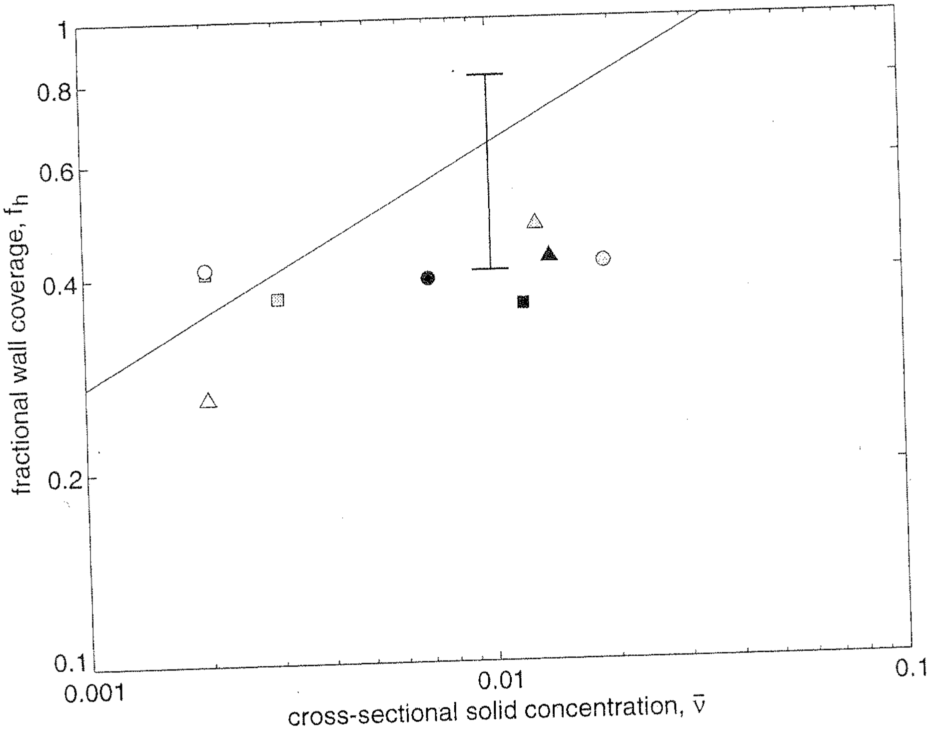

Figure 5.21. Fractional wall coverage determined by a relative cutoff (the mean local solid volume fraction at the wall) versus the cross-sectional solid concentration obtained from the pressure profiles. The line is the model of Lints and Glicksman (1993), that was suggested with the use of an absolute cutoff for cluster definition. The symbols are defined according to the caption of Figure 5.15.

## *5.4 Cluster Solid Concentration*

To be consistent with the method described in the previous subsection for the extraction of the relative fractional wall coverage, we use the same definition of clusters to calculate their average solid fractions. Figure 5.22 thus shows the cluster solid fraction $\nu_c$ where we define clusters as having a mean solid volume fraction above the mean local solid fraction at the wall. As this figure illustrates, the agreement with the correlation of Lints (1992) for cluster solid fraction versus average solid concentration is reasonable.

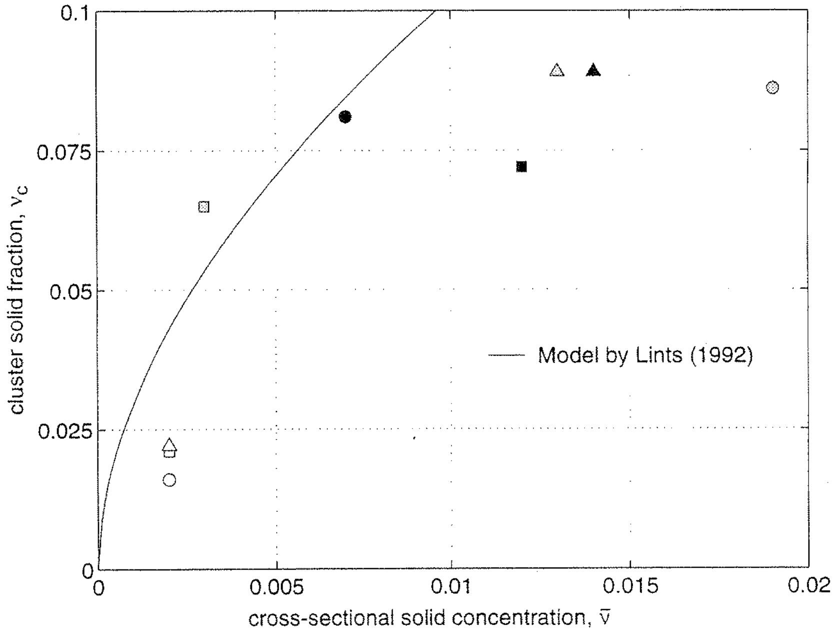

Figure 5.22. Extracted cluster solid volume fraction, using a relative means of identifying clusters, versus the cross-sectionally averaged solid fraction estimated from the pressure profiles. The symbols are defined according to the caption of Figure 5.15.

### *5.5 Heat Transfer Coefficient*

Using the experimental approach outlined in Chapter Four, we conducted measurements of the heat transfer coefficient that incorporated guard heaters and accounted for conduction losses.

Appendix C presents actual traces of simultaneous measurements of the heat transfer coefficient and solid fraction for varying operational conditions. Figure 5.23 shows the measured dimensionless heat transfer coefficient, $Nu_d$, versus the square root of the ratio of time constants, $(\tau_p/\tau_c)^{1/2}$. The cluster residence time at the wall, $\tau_c$, is given by $\lambda/U_{cl}$, where $\lambda$ is the measured residence length at each run condition and $U_{cl}$ is obtained from the scaling of Equation 2.26.

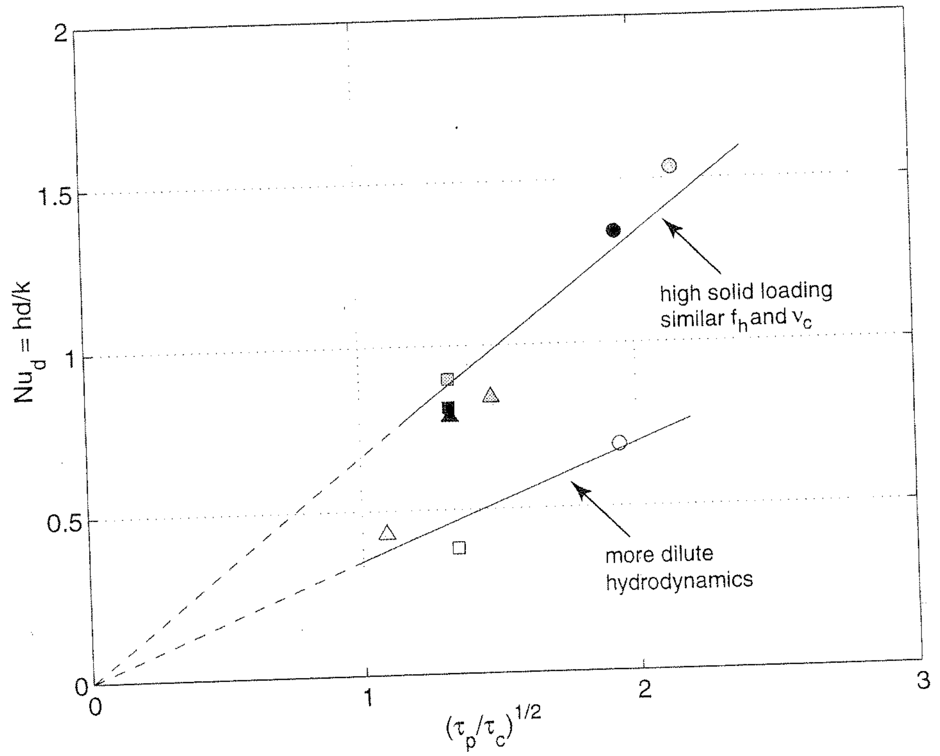

Figure 5.23 Measured Nusselt number based on particle diameter versus the square root of the ratio of time constants, for runs matched via the reduced set. White, gray and black symbols are for the low Fr low M runs, low Fr high M runs and high Fr high M runs, respectively. Squares, circles and triangles are for the glass 107 μm, glass 102 μm, and plastic 104 μm runs, respectively.

Figure 5.23 suggests a linear dependence of the measured Nusselt number on $(\tau_p/\tau_c)^{1/2}$, as was suggested in Equation 2.42. However, it is clear that the high solid loading runs have a different slope and intercept than the dilute runs with combined low Froude and low M.

Figure 5.24 shows $Nu_d$ as a function of the quantity $f_h(\nu_c\tau_p/\tau_c)^{1/2}$, as suggested by Equation 2.41. Here, $\tau_p$ can be written in terms of Equation 2.28 and $\tau_c$ is given by $\lambda/U_{cl}$. Another way to interpret the abscissa of Figure 5.24 is to regard it as a dimensionless $h_H$, according to Equation 2.29, where we use the simplification that $h_{overall}$ is proportional to $f_h h_H$. Figure 5.24 thus differs from Figure 5.23 by the inclusion of the measure of the fractional wall coverage and cluster solid fraction based on a relative cutoff for cluster definition for each run, as described in Sections 5.3 and 5.4. It can be seen that including these two parameters now groups the data onto a single line. This demonstrates that $f_h$ and $\nu_c$ are critical for proper convective heat transfer scaling. However, from these experiments, it is unclear whether there is a non-zero value of the intercept. We suspect that the presence of the dilute phase heat transfer coefficient would cause a relatively small, but non-zero intercept.

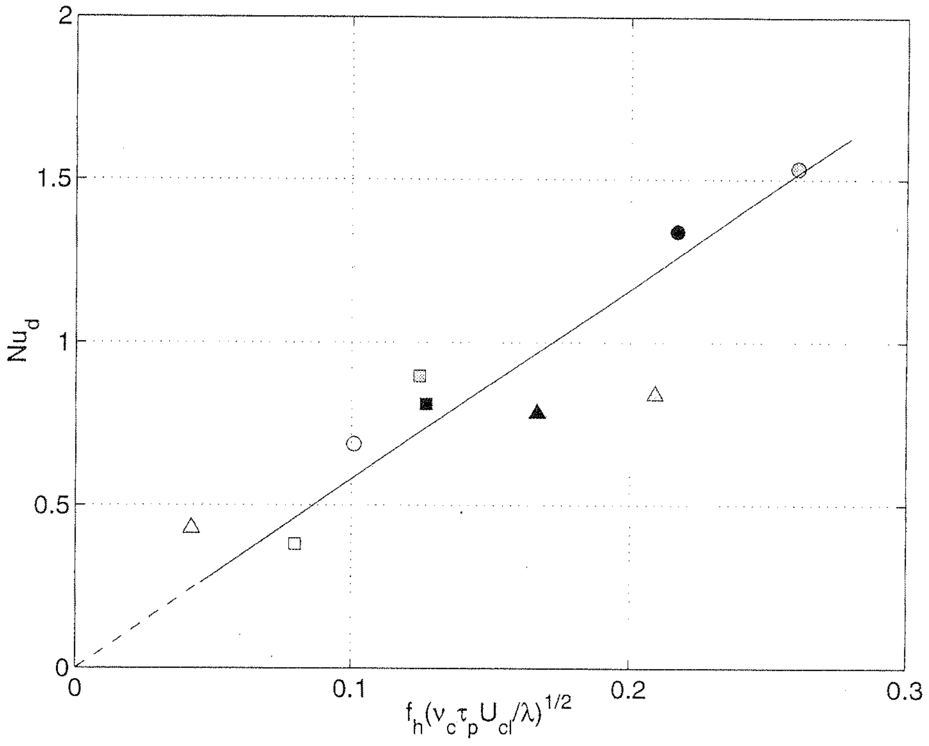

Figure 5.24 Nusselt number based on particle diameter versus the product $f_h(\nu_c\tau_pU_{cl}/\lambda)^{1/2}$ for runs matched via the reduced set. White, gray and black symbols are for the low Fr low M runs, low Fr high M runs and high Fr high M runs, respectively. Squares, circles and triangles are for the glass 107 μm, glass 102 μm and plastic 104 μm runs, respectively.

Next we utilize Glicksman's correlation for $\delta$ (Equation 2.35), and approximate $h_g$ by using single phase correlations for $Nu_D$ based on pipe Reynolds number for hydrodynamically and thermally fully developed flow. Consistent with Lints and Glicksman (1993), we also employ our measurements of $\nu_c$ and $f_h$ in this model. This allows us to calculate $h_{overall}$ using the complete five-parameter model of Equation 2.33, where we have replaced the emulsion conductivity $k_e$ by that of the fluid k.

Figure 5.25 shows the measured Nusselt number versus predicted $h_{overall}$, non-dimensionalized by hydrodynamic diameter, d, and gas conductivity, k. Unfortunately, the magnitude of the measured Nusselt number is consistently higher than the predicted one by over a factor of four. While the model of Lints and Glicksman (1993) captures the trend of the dependence of $Nu_d$ on the five parameter model described in Section 2.2.7, it fails to predict the absolute magnitude, at least for the conditions of our experiments.

An analysis of the model of Lints and Glicksman (1993) reveals that, under our operating conditions, the predicted heat transfer coefficient is primarily sensitive to the magnitude of $f_h$, while it is less influenced by $\delta$. Therefore, because $f_h$ is necessarily less than 1, we cannot bring our results into agreement with the model by invoking experimental error in $f_h$ alone. Consequently, the discrepancy must arise from the form of $h_H$ that Lints and Glicksman assumed (Equation 2.29). However, our results of Figure 5.23 and 5.21 clearly demonstrate that the trend of $Nu_d$ versus $f_h(\nu_c\tau_p/\tau_c)^{1/2}$ follows the model of Lints and Glicksman (1993), albeit within a numerical constant.

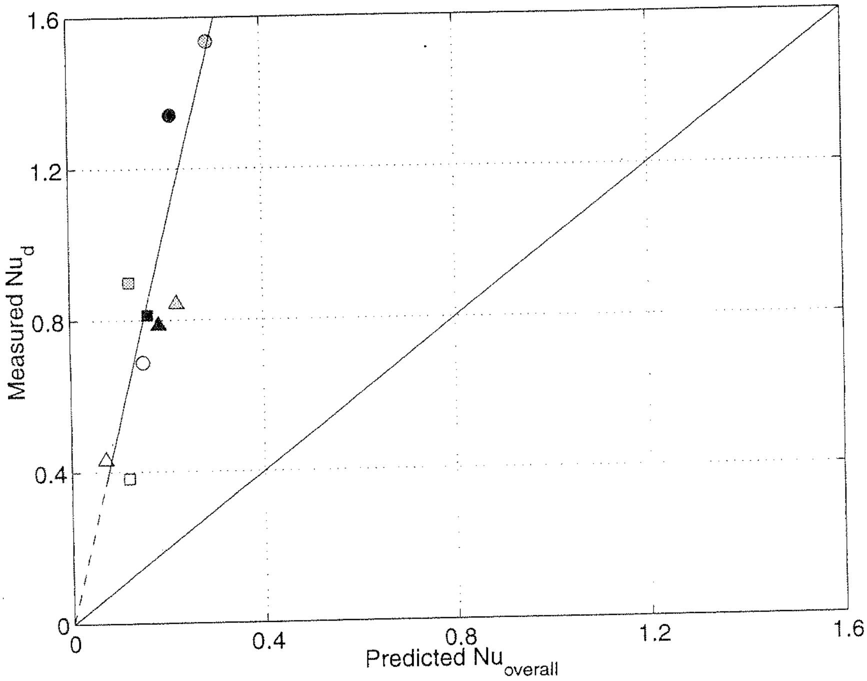

Figure 5.25 Measured Nusselt number based on particle diameter versus predicted $Nu_{overall}$ from Equation 2.33, where h is non-dimensionalized by the particle diameter, for runs matched via the reduced set. White, gray and black symbols are for the low Fr low M runs, low Fr high M runs and high Fr high M runs, respectively. Squares, circles and triangles are for the glass 107 μm, glass 102 μm and plastic 104 μm runs, respectively.

# CHAPTER SIX:
# CONCLUSIONS

The goals of this thesis have been to develop scaling laws for convective heat transfer rates and to design and test useful instrumentation. We have presented two new measurement systems, new scalings for cluster velocity and residence length at the wall, and confirmed the dependence of the Nusselt number on parameters of the phenomenological model proposed by Lints and Glicksman (1993).

A new instrument for local, instantaneous, non-invasive, simultaneous measurement of solid volume fraction and convective heat transfer coefficient at the wall of a CFB riser is demonstrated. The measurement includes guard heaters for thermal development of the flow. The analysis for the measurement of convective heat transfer coefficient accounts for conduction losses. Rapid time-dependent traces of solid fraction and heat transfer coefficient show that h is a strong function of the local solid fraction. Tests of the heat transfer sensor demonstrated a system response time of about 25ms. This time constant is significantly faster than the 45 or 85 ms reported for heat transfer sensors used in earlier studies (Wu et al., 1989a; Dou et al., 1992).

A novel thermal marking technique based on rather simple tools is used to measure the residence length of clusters at the wall of the CFB riser. Heaters upstream of the probe tag passing clusters with heat. A thermocouple sensor located at the center of a guarded capacitance probe, flush with the riser wall, measures the fraction of heated clusters near the wall. By comparing traces from varying heater-to-probe spacings and utilizing a statistical analysis, we extract the probability distribution function of the residence length of clusters and their mean residence length.

Measurements of the cluster residence length at the wall were achieved for runs that were hydrodynamically matched via the reduced set scaling laws, and then for conditions matched to the full set, but with a significantly different riser diameter to particle diameter ratio. All runs had R = 1675, corresponding to a simulated combustor under pressure of 0.64 MPa. The results suggest that the cluster residence length scales with particle diameter, but is independent of operational conditions. This trend is shown in Figure 5.15. This scaling of cluster residence length agrees with limited data by Noymer (1997), who saw a slight increase of cluster residence time with particle diameter.

The fraction of the wall covered by clusters was extracted from local, instantaneous solid volume measurements. In Figures 5.16-5.18, we compare results based on absolute and relative cluster definitions to the model by Lints and Glicksman (1993a). We find that agreement with their model is dependent on the choice of cluster definition. Since clusters in dilute flows are less dense than those in denser flows, we propose the use of a relative cutoff for cluster definition, whereby clusters are defined as having solid volume fractions above the local mean at the wall. We obtain results for cluster solid fractions, shown in Figure 5.22, by using the same relative means for cluster definition. Cluster solid fraction results agree well with the model by Lints (1992) for cross-sectionally averaged solid fractions less than 1%.

A literature review of measurements of the cluster velocity at the wall of CFB risers suggests that cluster velocity scales as $36\sqrt{gd}$ (Figure 2.1), independent of operating conditions. The scaling trends of cluster velocity and residence length at the wall of the riser indicate that cluster motion near the wall is dominated by local interactions, not overall CFB hydrodynamics.

The Nusselt number based on particle diameter is shown in Figure 5.23 to be strongly influenced by the square root of the ratio of time constants. However, this ratio alone cannot predict the Nusselt number at the wall. Instead, we show that the fractional wall coverage, $f_h$, and cluster solid fraction, $v_c$, need to be included in a model that holds for varying hydrodynamic conditions. Thus, we suggest a dependence of the Nusselt number on the product of fractional wall coverage and the non-dimensionalized heat transfer coefficient due to the cluster phase, $h_H$. Here, we use a form of the cluster phase heat transfer coefficient, described in Section 2.2.5, given by $h_H \propto (k\rho_s c_p v_c/\tau_c)^{1/2}$. This dependence of measured Nusselt number on the product of fractional wall coverage and non-dimensionalized cluster phase heat transfer coefficient holds even for runs with dramatically different hydrodynamic conditions, e.g., dilute versus dense flows, as demonstrated in Figure 5.24.

Finally, we compared our measured Nusselt number at the CFB wall to a predicted Nusselt number based on the phenomenological model proposed by Lints and Glicksman (1993). Although we found a linear relation between the measured Nusselt number and the predicted value, the model underpredicted the Nusselt number by over a factor of four, as shown in Figure 5.25.

In this investigation, we have performed successful trials of two new diagnostics, namely the combination heat transfer and capacitance probe and the thermal marking technique. Finally, we have demonstrated a proper hydrodynamic scaling framework that allows us to investigate the dependence of the convective heat transfer coefficient on suggested thermal parameters of the flow.

# APPENDIX A:
# ESTIMATION OF BIOT NUMBER

In calculating the thermal time constant of a particle near the wall using the discrete particle model, described in Section 2.2.4, we used the lumped capacitance method to write the differential equation governing the heat transfer from the particle. The condition for using such a model is that the particle Biot number, defined as $hd/k_s$, must be less than 0.1. Thus, we need to estimate a typical value of the Biot number for our CFB experiments.

To evaluate a typical Biot number for particles in our CFB flows, we use the typical mean hydrodynamic diameter, 100 μm. The thermal conductivity of the glass and plastic particles are 1.4 and 0.35 W/mK at ambient temperature, respectively. In order to determine a typical value for the heat transfer coefficient, we first need to calculate the Nusselt number, which in turn is dependent on the Reynolds, $Re_d$, and Prandtl, Pr, numbers of the flow. The Prandtl number for air is 0.71. To calculate $Re_d = \rho U_{slip} d/\mu$, we use a worst-case estimate of the slip velocity, given by 1 m/s, or approximately 1/2 to 1/4 of the superficial gas velocity through the riser. Then using the properties of air at ambient temperature, $\rho = 1.16$ kg/m$^3$ and $\mu = 185 \times 10^{-7}$ Ns/m$^2$, we find that $Re_d$ is about 6. We use the correlation by Whitaker for flow past spheres (Incropera and Dewitt, 1990) to determine the corresponding Nusselt number. Using the hydrodynamic particle diameter, $Nu_d$ is approximately 3, and solving for h gives 800 W/m$^2$K.

To calculate Biot numbers for spheres, Incropera and Dewitt (1990) recommend using a lengthscale of one third of the particle radius. Then, for glass beads and plastic in air, the Biot numbers are 0.01 and 0.03, respectively. These values are well below the $Bi < 0.1$ cutoff necessary for using the lumped capacitance approach, in which the temperature of the particle is treated as spatially uniform at any instant.

# APPENDIX B

## DERIVATION OF EQUATION 2.29.

In this Appendix we summarize the calculation of Mickley and Fairbanks (1955) which leads to Equation 2.29 in Section 2.2.5.

Mickley and Fairbanks argue that any complete physical description of the heat transfer mechanisms in a fluidized bed would be extremely complex. Instead, to derive an analytical model, they consider the heat transfer rate from a heated surface at temperature $T_1$ to a packet of the emulsion phase at bed temperature $T_b$

$$q_m = A_m(T_1 - T_b)\sqrt{\frac{k_m \rho_m c_p}{\pi\tau}}, \tag{B.1}$$

where $A_m$ is the area of contact of the packet with the surface, $k_m$, $\rho_m$ and $c_p$ are the thermal conductivity, density and heat capacity of the packet, respectively, and $\tau$ is the contact time. Equation B.1 corresponds to the heat transfer rate into a semi-infinite slab which is initially at temperature $T_b$, and whose exposed surface is at temperature $T_1$. By using Equation B.1, Mickley and Fairbanks (1955) assume that the packet can be treated as a homogeneous medium with constant effective properties $k_m$, $\rho_m$ and $c_p$, and that heat has diffused into the packet a distance less than the size of the packet.

Based on Equation B.1, the local instantaneous heat transfer coefficient, $h_i$, is given by

$$h_i = \frac{q_m}{A_m(T_l - T_b)} = \sqrt{\frac{k_m \rho_m c_p}{\pi \tau}} . \qquad (B.2)$$

However, a measured, or observed, local heat transfer coefficient is actually the time average of all the local, instantaneous coefficients occurring during a period of time at a particular point on the heated surface. Therefore, by applying temporal and spatial averaging over an isothermal surface area, and assuming that all clusters have the same residence time at the wall, they obtain

$$h = \frac{1}{L_x} \int_0^{L_x} h_{av} dL_x = 2\sqrt{\frac{k_m \rho_m c_p}{\pi \tau_c}} , \qquad (B.3)$$

which is identical to Equation 2.29, where in our study, we have renamed this temporally and spatially averaged heat transfer coefficient $h_H$, and in place of $k_m$ we use the gas conductivity k (as described in Section 2.2.5), $\rho_m$ becomes the product $\rho_s v_c$ that is equal to the solid density of the cluster, and $\tau_c$ represents the cluster contact time with the wall.

It is clear that to capture the trends of a heat transfer coefficient that is measured over a large constant temperature surface, the analytical approach requires a temporal and spatial averaging method that must be similar in form to the one presented by Mickley and Fairbanks (1955).

# APPENDIX C:
# ACTUAL DATA TRACES

## *C.1 Simultaneous heat transfer coefficient and solid volume fraction*

In this section, we present results from the combination probe that was described in Section 4.1.

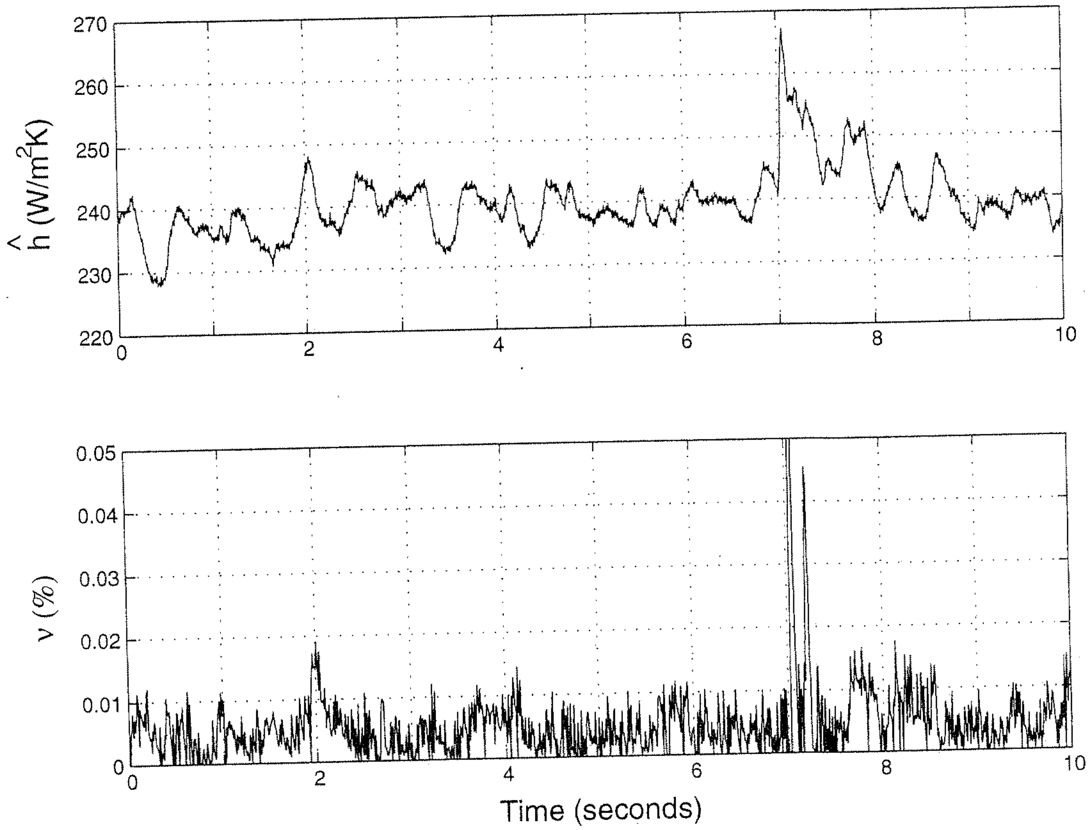

Figure C.1. Simultaneous traces of heat transfer coefficient and solid fraction measured by the combination probe. The inventory in this case is 107 μm glass, and the operating conditions are low Fr and low solids loading, M. For the complete list of dimensionless numbers, see Table 5.1. For all data shown in this appendix, the acquisition frequency is 100 Hz.

The capacitance signals may exhibit sudden voltage spikes extending above the voltage in the absence of particles or below that expected for close packing. These spikes are not associated with the flow structure, but rather are the result of amplifier instabilities from passing electrostatics. When the electrostatics are not excessive, most of the signal can be exploited by merely removing the spikes. Because the signature is obvious, these spikes may easily be removed manually from the traces. However, sanitizing signals in this way is time consuming. Instead, to this end, we employed the Butterworth low pass filter shown in Figure C.2. This suppresses the spikes by reducing the high frequency noise of the solid fraction traces presented in this appendix. To preserve the phase of the signals, we consistently apply the Butterworth filter of Figure C.2 both forward and backward on the data, as executed by the Matlab “filtfilt” function (Mathworks, 1999).

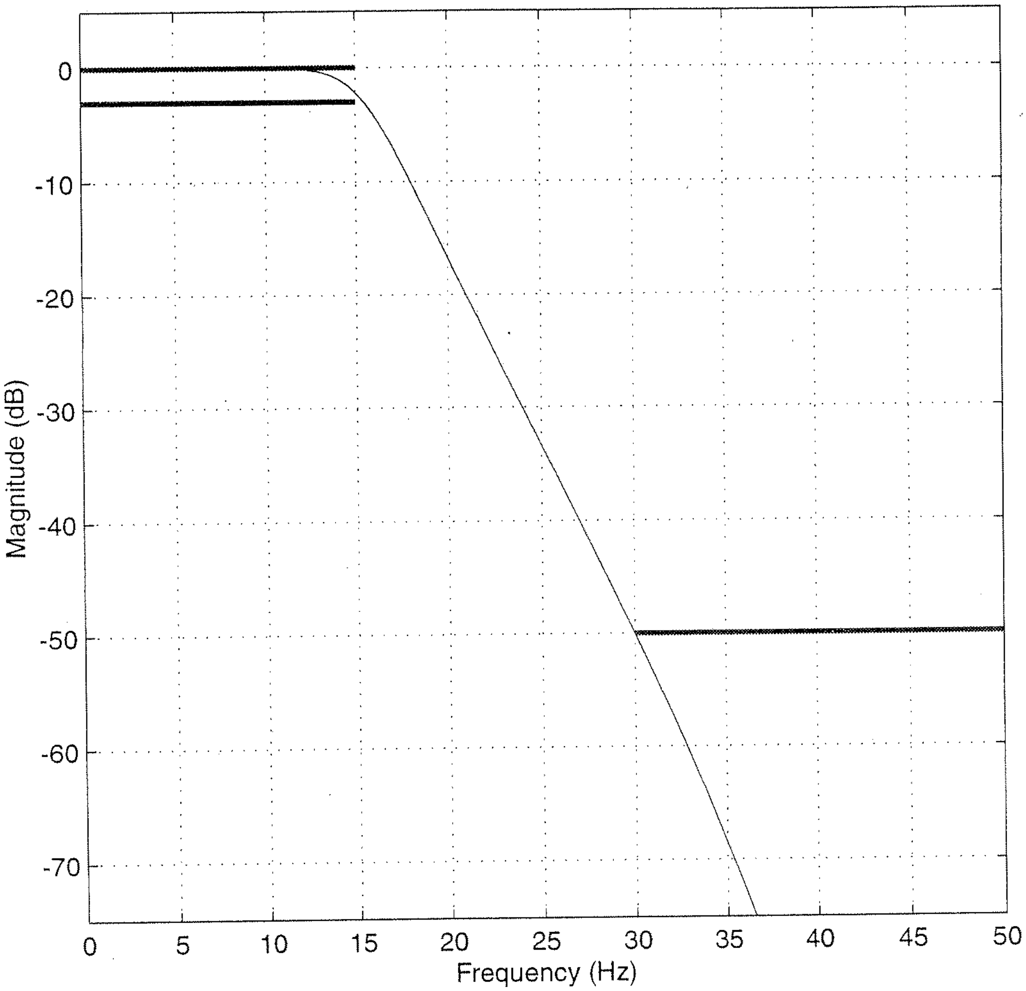

Figure C.2. Butterworth low pass filter of order 6. The passing and stop frequencies are 15 and 30 Hz, respectively.

The following 9 traces show simultaneous heat transfer coefficient and solid fraction traces obtained during the experiments.

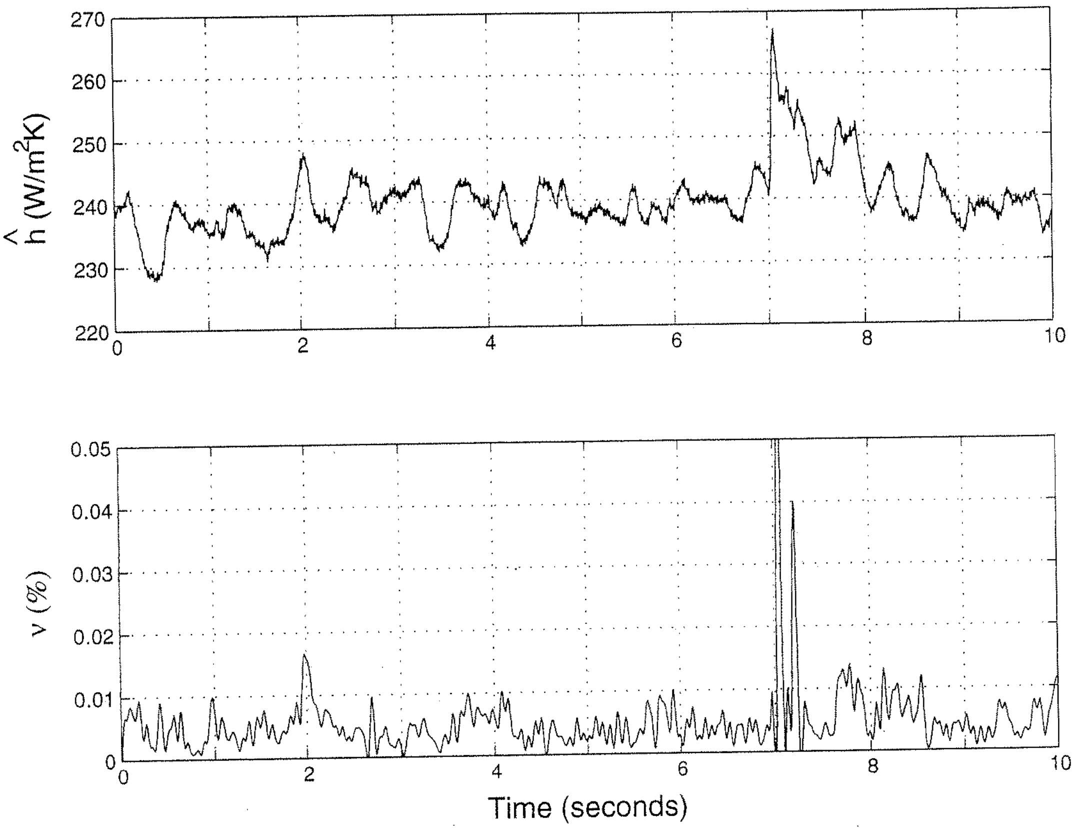

Figure C.3. Simultaneous heat transfer coefficient and solid fraction measured by the combination probe at the wall. The inventory in this case is 107 μm glass, and the operating conditions are low Froude and low solids loading, M. Here, the solid fraction trace has been filtered by the Butterworth filter of Figure C.2.

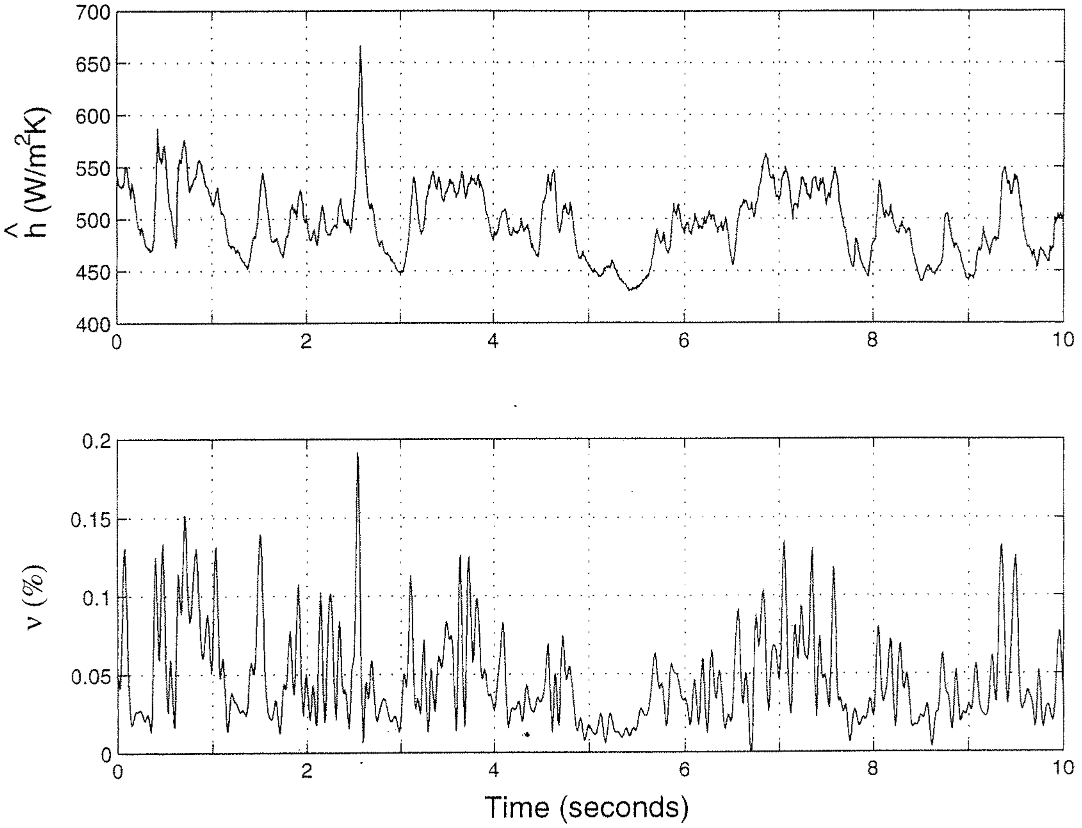

Figure C.4. Simultaneous heat transfer coefficient and solid fraction measured by the combination probe at the wall. The inventory in this case is 107 μm glass, and the operating conditions are low Froude and high solids loading, M. Here, the solid fraction trace has been filtered by the low pass filter shown in Figure C.2.

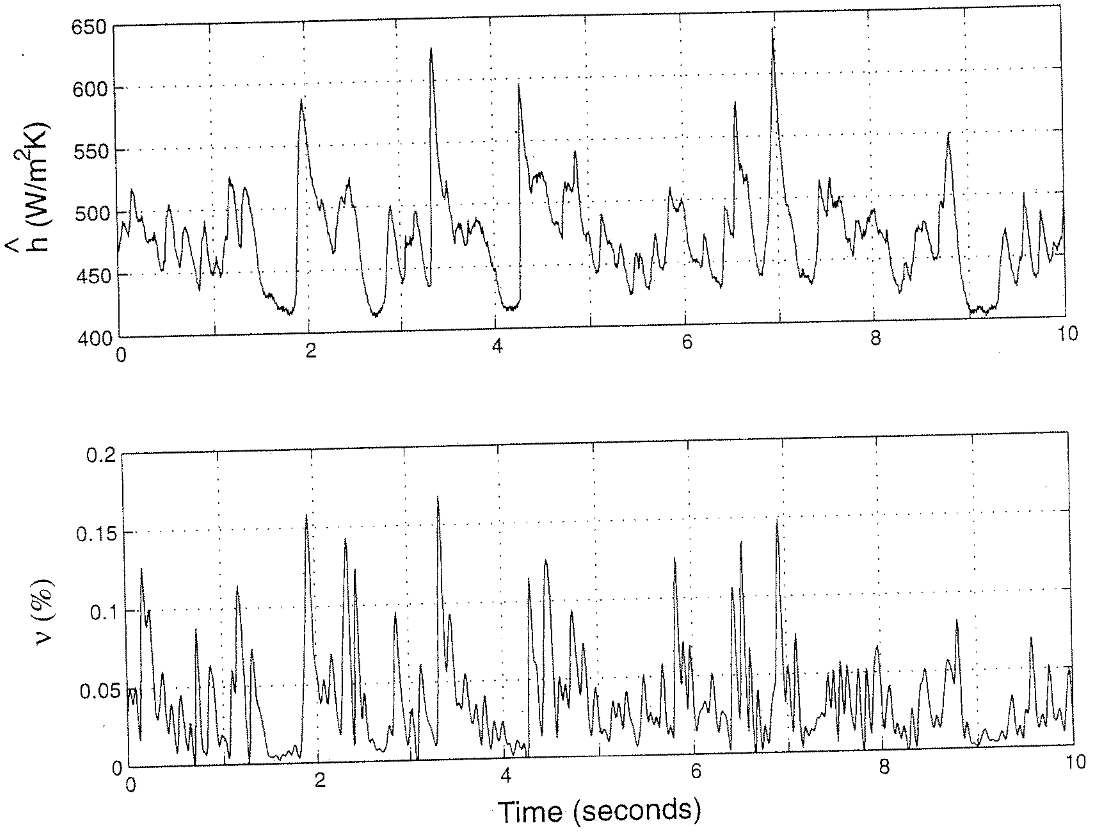

Figure C.5. Simultaneous heat transfer coefficient and solid fraction measured by the combination probe at the wall. The inventory in this case is 107 μm glass, and the operating conditions are high Froude and high solids loading, M. Here, the solid fraction trace has been filtered by the low pass filter shown in Figure C.2.

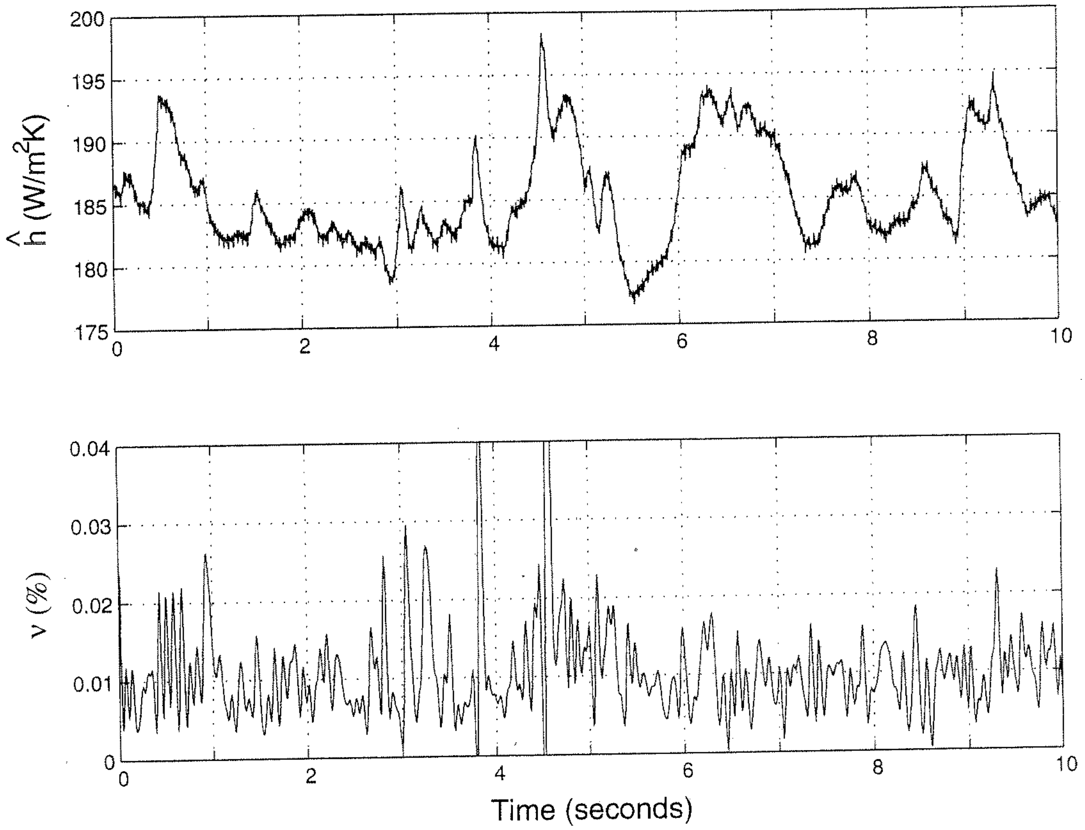

Figure C.6. Simultaneous heat transfer coefficient and solid fraction measured by the combination probe at the wall. The inventory in this case is 102 μm glass, and the operating conditions are low Froude and low solids loading, M. Here, the solid fraction trace has been filtered by the low pass filter shown in Figure C.2.

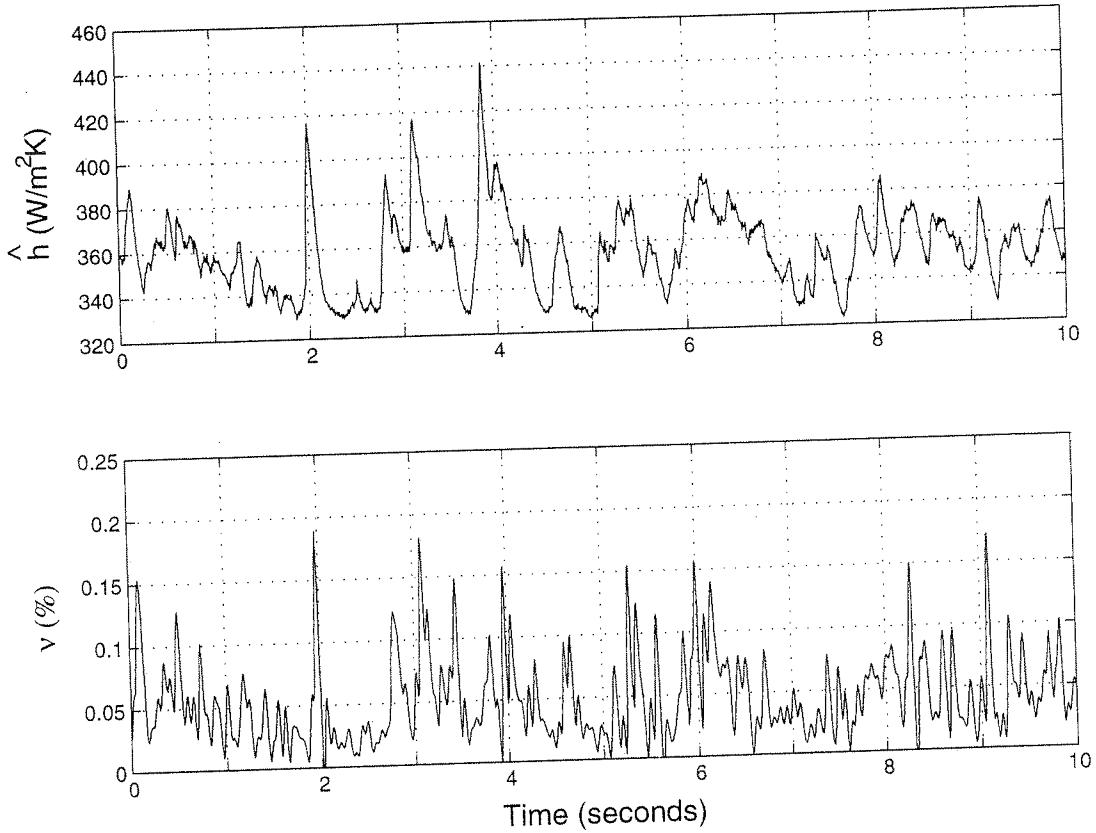

Figure C.7. Simultaneous heat transfer coefficient and solid fraction measured by the combination probe at the wall. The inventory in this case is 102 μm glass, and the operating conditions are low Froude and high solids loading, M. Here, the solid fraction trace has been filtered by the low pass filter shown in Figure C.2.

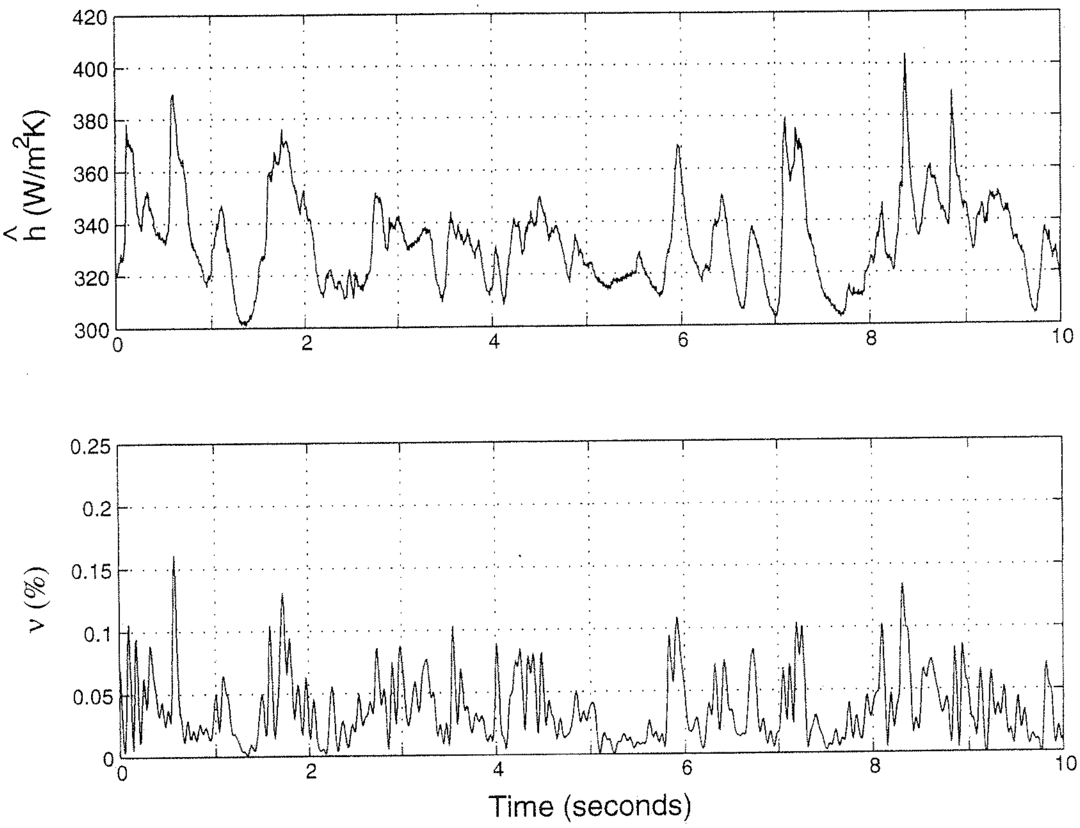

Figure C.8. Simultaneous heat transfer coefficient and solid fraction measured by the combination probe at the wall. The inventory in this case is 102 μm glass, and the operating conditions are high Froude and high solids loading, M. Here, the solid fraction trace has been filtered by the low pass filter shown in Figure C.2.

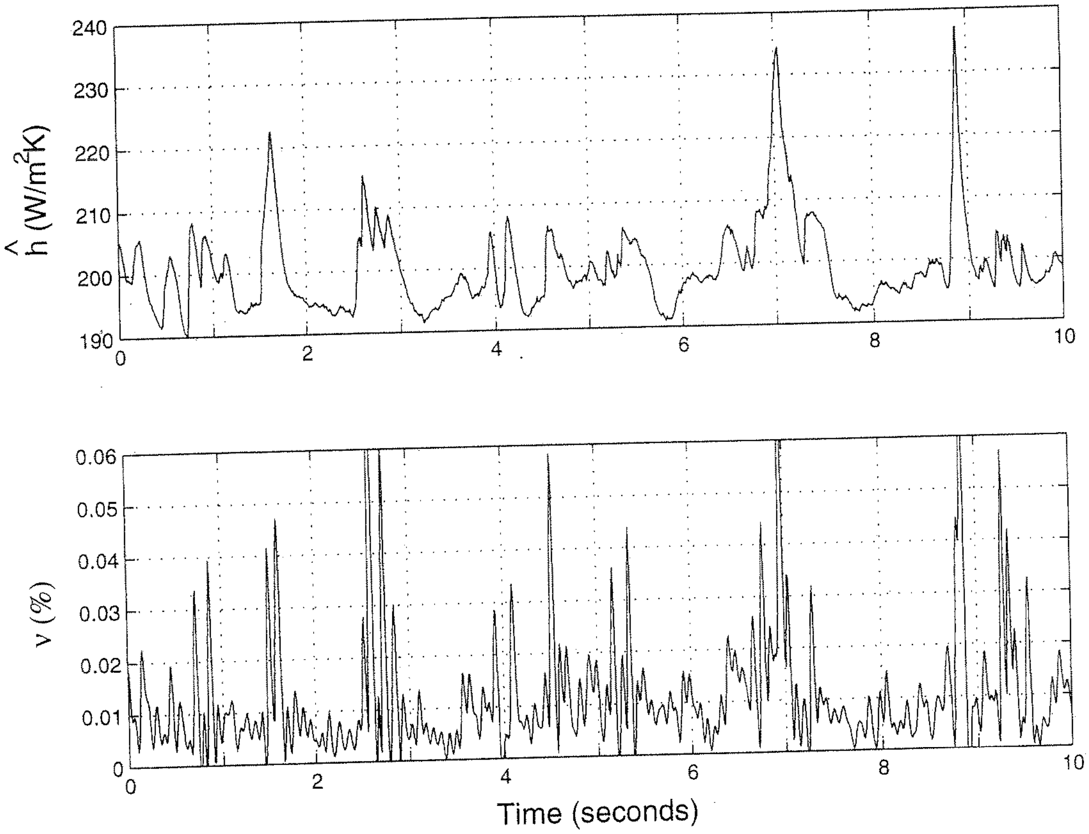

Figure C.9. Simultaneous heat transfer coefficient and solid fraction measured by the combination probe at the wall. The inventory in this case is 104 μm plastic, and the operating conditions are low Froude and low solids loading, M. Here, the solid fraction trace has been filtered by the low pass filter shown in Figure C.2.

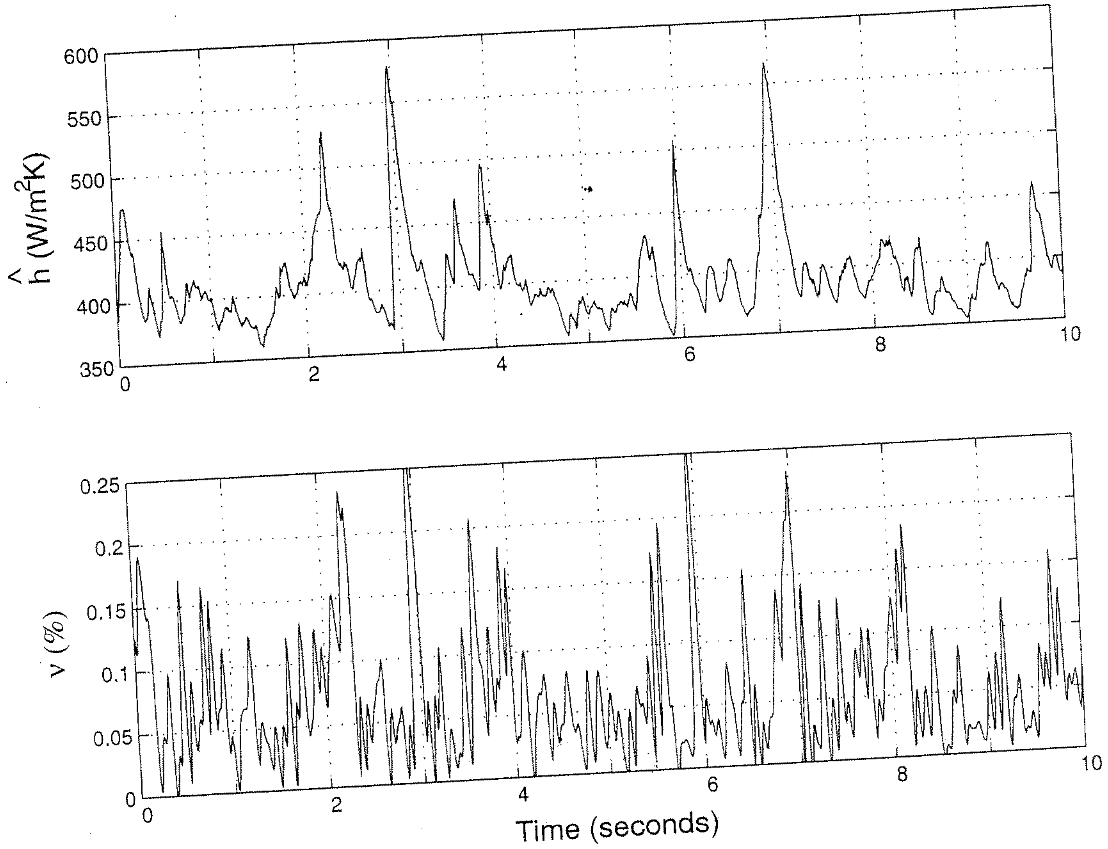

Figure C.10. Simultaneous heat transfer coefficient and solid fraction measured by the combination probe at the wall. The inventory in this case is 104 μm plastic, and the operating conditions are low Froude and high solids loading, M. Here, the solid fraction trace has been filtered by the low pass filter shown in Figure C.2.

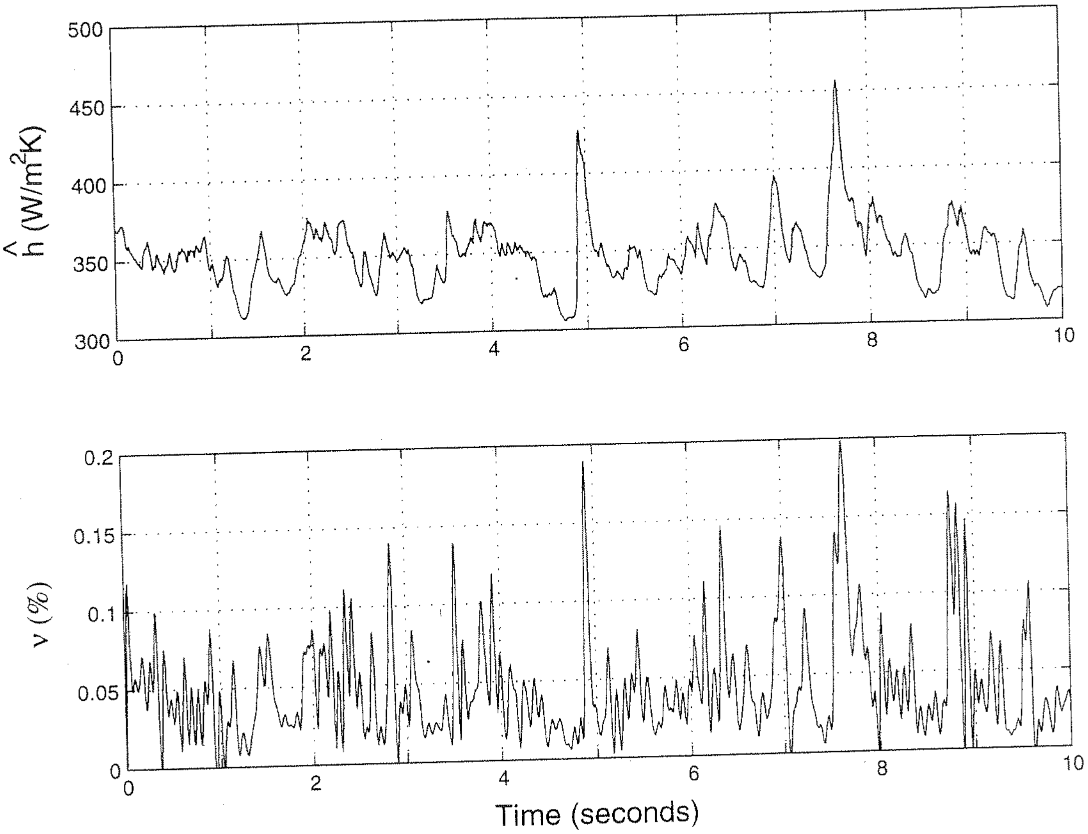

Figure C.11. Simultaneous heat transfer coefficient and solid fraction measured by the combination probe at the wall. The inventory in this case is 104 μm plastic, and the operating conditions are high Froude and high solids loading, M. Here, the solid fraction trace has been filtered by the low pass filter shown in Figure C.2.

## *C.2 Simultaneous temperature fluctuation and solid volume fraction*

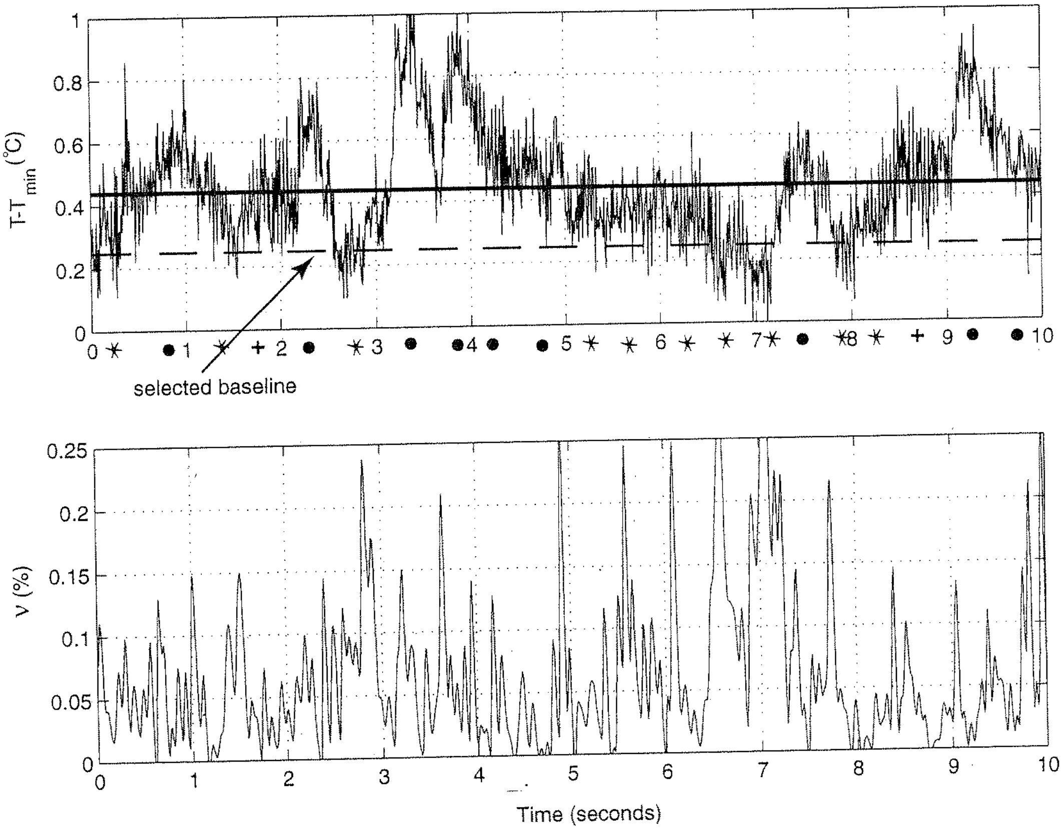

Figure C.12. Simultaneous traces of solid fraction and measured temperature fluctuation, from the capacitance-thermocouple probe. Here, the spacing, $L_0$, was 8" (corresponding to the small spacing runs), the inventory was 102 μm glass, and the run conditions were $Fr^2/L = 5.4$, $U_0/U_t = 8.6$, $M/R = 0.0060$, and $R = 1675$. Here, the solid fraction trace has been filtered by the low pass filter shown in Figure C.2.

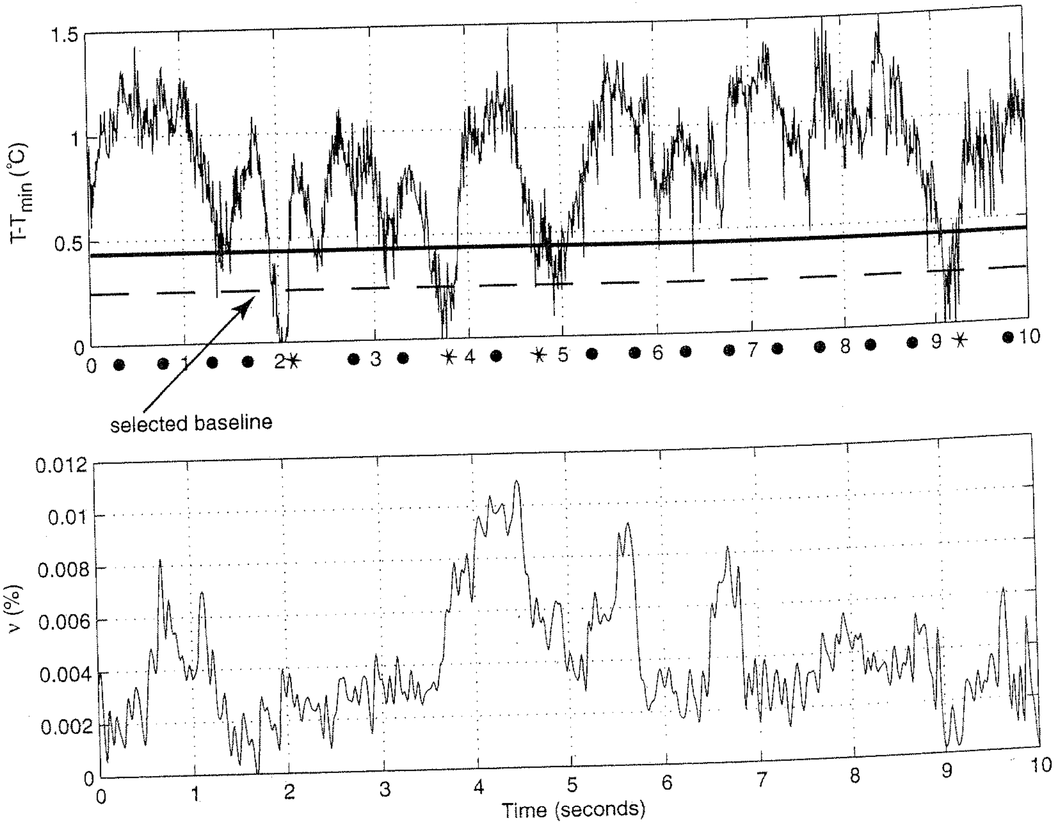

Figure C.13. Simultaneous traces of solid fraction and measured temperature fluctuation, from the capacitance-thermocouple probe. Here, the spacing, $L_0$, was 8" (corresponding to the small spacing runs), the inventory was 64 μm glass, and the run conditions were $Fr^2/L = 3.3$, $U_0/U_t = 9.7$, $M/R = 0.0015$, and $R = 1675$. Here, the solid fraction trace has been filtered by the low pass filter shown in Figure C.2.

# REFERENCES

Acree-Riley, C., Louge, M.Y.: "Quantitative capacitance measurements of voidage in gas-solid flows", Particulate Sci. and Tech., **7** (1989) p.51

Anderson, T.B., Jackson, R.: "A fluid mechanical description of fluidized beds – equations of motion", Ind. Eng. Chem. Fundamentals, **6** (1967) p.527

Bader, R., Findlay, J., Knowlton, T.M.: "Gas/solid flow patterns in a 30.5-cm-diameter circulating fluidized bed", Circulating Fluidized Bed Technology II, Basu, P., Large, J.F. (eds.), Pergamon Press, Oxford, U.K. (1988) p.123-137

Basu, P., Nag, P.K.: "An investigation into heat transfer in circulating fluidized beds", Int. J. Heat Mass Transfer, **30** (1987) p.2399

Bejan, A.: *Advanced engineering thermodynamics*, Wiley and Sons, New York, 1997

Bi, H., Jin, Y., Yu, Z., and Bai, D.: "An investigation on heat transfer in circulating fluidized bed", Circulating

Fluidized Bed Technology III, Basu, P., Horio, M. and Hasatani, M. (eds.), Pergamon Press, Oxford, U.K. (1991).

Böttcher, C.J.F.: "The dielectric constant of crystalline powders", Rev. Trav. Chim., **64** (1945) p.47

Brereton, C.: "Combustion Performance", Chapter 10 of *Circulating Fluidized Beds*, Grace, J.R., Avidan, A.A., Knowlton, T.M. (eds.), Blackie Academic and Professional, London, U.K. (1997) p.369-416

Bricout, V.G.: "Hydrodynamic scaling and cyclone performance of pressurized circulating fluidized beds", Ph.D. Thesis, Cornell University, Ithaca, NY (2000)

Burki, V., Hirschberg, B., Tuzla, K., et al., "Thermal development for heat transfer in CFBs", Annual AIChE Meeting, Paper 66f, St. Louis, Missouri, Nov. 7-13 (1993)

Chang, H.: "Experimental investigation of circulating fluidized bed scale-up", Ph.D. Thesis, Cornell University, Ithaca, NY (1991)

Chang, H., Louge, M.Y.: "Fluid dynamic similarity of circulating fluidized beds", Powder Technology, **70** (1992) p.259-270

Dasgupta, S., Jackson, R., Sundaresan, S.: "Gas-particle flow in vertical pipes with high mass loading of particles", Powder Technology, **96** (1998) p.6-23

Dasgupta, S., Jackson, R., Sundaresan, S.: "Developing flow of gas-particle mixtures in vertical ducts", Ind. Eng. Chem. Res., **36** (1997) p.3375-3390

Decker, N. and Glicksman, L.R.: "Conduction heat transfer at the surface of bodies immersed in gas fluidized beds of spherical particles", AIChE Symposium Series, **77** (1981).

Dou, S.: "Experimental study of heat transfer in circulating fluidized beds", Doctoral Thesis, Lehigh University, Bethlehem, Pennsylvania (1990).

Dou, S., Herb, B., Tuzla, K., Chen, J.C.: "Dynamic variation of solid concentration and heat transfer coefficient at wall of Circulating Fluidized Bed", Proceedings of the Seventh Engineering Foundation Conference on Fluidization, Australia, (1992) p.793

Ebert, T.A., Glicksman, L.R., Lints, M.: "Determination of particle and gas convective heat transfer components in a CFB", Chem. Eng. Sci., **48**, (1993) p.2179-2188

Fang, Z.H., Grace, J.R., Lim, C.J.: "Local particle convective heat transfer along surface in CFBs", Int. Journal Heat and Mass Transfer, **38** no.7 (1995) p.1217-1224

Foscolo, P.U., Gibilaro, L.G.: "A fully predictive criterion for the transition between particulate and aggregate systems", Chem. Eng. Sci., **39** (1984) p.1637

Geldart, D., Rhodes, M.J.: "From minimum fluidization to pneumatic transport – a critical review of the hydrodynamics", Circulating Fluidized Bed Technology, Basu, P. (ed.), Pergamon Press, New York (1986) p.21

Gelperin, N.I. and Einstein, V.G.: "Heat transfer in fluidized beds", Fluidization, Davidson, J.F. and Harrison, D. (eds.), Academic Press, New York, Chapter 10 (1971) p. 471

Glicksman, L.R.: "Scaling relationships for fluidized beds", Chemical Engineering Science, vol. **39**, no. 9, (1984) p.1373-1379

Glicksman, L.R.: "Circulating fluidized bed heat transfer", Circulating Fluidized Bed Technology II, Basu, P., Large, J.F. (eds.), Pergamon Press, New York (1988) p.13-29

Glicksman, L.R., Westphalen, D., Woloshun, K., Ebert, T., Roth, K., Lints, M., Brereton, C.M.H., Grace, J.R., “Experimental scale models of circulating fluidized bed combustors”, Proc. of the Clean Energy for the World Intern. Conf. on Fluidized Bed Combustion, Apr 21-24, 1991, **3** (1991) p.1169-1175.

Glicksman, L.R., Hyre, M., Woloshun, K.: “Simplified scaling relationships for fluidized beds”, Powder Technology, **77** (1993) p.177

Glicksman, L., Hyre, M., Farrell, P.: “Dynamic similarity in fluidization”, Int. J. Multiphase Flow, **20** (supp.), (1994) p.331

Glicksman, L.R., Noymer, P.D.: “Measurements of the velocity and acceleration of clusters at the wall of a circulating fluidized bed”, Preprints: Fluidization and Fluid-Particle Systems, Arastoopour, H., Chen, Y.M., Guttilla, T. (eds.), AIChE, New York (1996) p.45-52

Glicksman, L.R.: “Heat transfer in circulating fluidized beds”, Chapter 8 of *Circulating Fluidized Beds*, Grace, J.R., Avidan, A.A., Knowlton, T.M. (eds.), Blackie Academic and Professional, London, U.K. (1997) p.261-311

Golriz, M., Leckner, B.: "Experimental studies of heat transfer in a circulating fluidized bed boiler", Proceedings International Conference on Engineering Applications of Mechanics, **3,** Sharif University of Technology, Teheran, Iran, (1992) p.167-174

Gore, R.A., Crowe C.T.: "Effect of particle size on modulating turbulent intensity", Int. J. Multiphase Flow, **15**, (1989) p.279-285

Grace: "Contacting modes and behaviour classification of gas-solid and other two-phase suspensions", Can. J. Chem. Eng., **64**, (1986) p.353-363

Griffith, A.E., Louge, M.Y.: "The scaling of cluster velocity at the wall of circulating fluidized bed risers", Chem. Eng. Sci., **53** (1998) p.2475-2477

Griffith, A.E., Louge, M., Mohd-Yusof, J.: "Simultaneous, non-invasive measurements of convective heat transfer and solid volume fraction at the wall of an entrained gas-solid suspension", Review of Scientific Instruments, accepted for publication (2000)

Haider, A., Levenspiel, O.: “Drag coefficient and terminal velocity of spherical and nonspherical particles”, Powder Technology, **58** (1989) p.63

Hartge, E.-U., Rensner, D., Werther, J.: “Solids concentration and velocity patterns in circulating fluidized beds”, Circulating Fluidized Bed Technology II, Basu, P., Large, J.F. (eds.), Pergamon Press, Oxford, U.K. (1988) p.165-180

Horio, M., Morishita, K., Tachibana, O., Murata, N.: “Solid distribution and movement in circulating fluidized beds”, Circulating Fluidized Bed Technology II, Basu, P., Large, J.F. (eds.), Pergamon Press, Oxford, U.K. (1988) p.147-154

Incropera, F., DeWitt, D.: *Fundamentals of heat and mass transfer*, John Wiley and Sons, New York, 1990

Kobro, H., Brereton, C.: “Control and fuel flexibility of circulating fluidised bed”, Circulating Fluidized Bed Technology, Basu, P. (ed.) Pergamon Press (1986).

Kunii, D. and Levenspiel, O.: *Fluidization Engineering*, Chapter 3, Robert E. Kreiger Publishing Company, Malabar, Florida, 1984

Li, J., Xia, Y., Tung, Y., Kwauk, M.: "Micro-visualization of two-phase structure in a fast fluidized bed", Circulating Fluidized Bed Technology III, Basu, P., Horio, M. and Hasatani, M. (eds.), Pergamon Press, Oxford, U.K., (1991) p.183-188

Lints, M.: "Particle-to-wall heat transfer in circulating fluidized beds", Doctoral Thesis, Massachusetts Institute of Technology, Cambridge, MA (1992).

Lints, M.C., Glicksman, L.R.: "Parameters governing particle-to-wall heat transfer in a circulating fluidized bed", Circulating Fluidized Bed Technology IV, Avidan, A.A. (ed.), Proceedings of the Fourth International Conference on Circulating Fluidized Beds, AIChE Symposium Series 296, Fluid-Particle Processes: Fundamentals and Applications, **89** 35 (1993a) p.297-304

Lints, M., Glicksman, L.R.: "The structure of particle clusters near the wall of a circulating fluidized bed", AIChE Symposium Series, **89** (1993b) p.35-47

Lockhart, C., Zhu, J., Brereton, C.M.H., et al.: "Local heat transfer, solids concentration and erosion around membrane tubes in a cold model CFB", Int. J. Heat Mass Transfer, **38** n.13, (1995) p.2403

Lorenz, A., Tuozzolo, C., Louge, M.Y.: "Measurements of impact properties of small, nearly spherical particles", Experimental Mechanics, (1997) p.292-298

Louge, M.Y., Lischer, D.J., Chang, H.: "Measurements of voidage near the wall of a CFB riser", Powder Technology, **62** (1990**a**) p.269

Louge. M.Y., Opie, M.: "Measurements of the effective dielectric permissivity of suspensions", Powder Technology, **62** (1990**b**) p.85

Louge, M., Mohd.Yusof, J., Jenkins, J.T.: "Heat transfer in the pneumatic transport of massive particles", Int. J. Heat Mass Trans., **36** (2), (1993) p.265

Louge, M.Y., Tuccio, M., Lander, E., Connors, P.: "Capacitance measurements of the volume fraction and velocity of dielectric solids near a grounded wall", Rev. Sci. Instrum., **67** (1996) p.1869

Louge, M.Y.: "Experimental Techniques", Chapter 9 of *Circulating Fluidized Beds*, Grace, J.R., Avidan, A.A., Knowlton, T.M. (eds.), Blackie Academic and Professional, London, U.K. (1997**a**) p.312-368

Louge, M.Y., Steiner, R., Keast, S., et al.: "Application of capacitance instrumentation to the measurement of density and velocity of flowing snow", Cold Regions Science and Technol., **25** (1997**b**) p. 47

Louge, M.Y., Bricout, V., Martin-Letellier, S.: "On the dynamics of pressurized and atmospheric circulating fluidized bed risers", Chem. Eng. Sci., 54 (1999) p.1811

Massah, H., Shaffer, F., Sinclair, J. Shahnam, M.: "Measurements of specular and diffuse particle-wall collision properties", Fluidization VIII, Lagurie, C., Large, J.F. (eds.), Proceedings of the Eighth International Conference on Fluidization, The Engineering Foundation, New York (1995) p. 641-648

Mathworks, The: Signal Processing Toolbox User's Guide, Matlab 5.3 (1999)

Mickley, H.S., Fairbanks, D.F.: "Mechanisms of heat transfer to fluidized beds" AIChE Journal, **1** (1955) p.374-384

Mohd. Yusof, J.: "Heat transfer in the pneumatic transport of massive particles: modeling and diagnostics", MS Thesis, Cornell University (1992)

Nowak, W., Mineo, H., Yamazaki, R., Yoshida, K.: "Behavior of particles in a circulating fluidized bed of a mixture of two different sized particles", Circulating Fluidized Bed Technology III, Basu, P., Horio, M., Hasatani, M. (eds.), Pergamon Press, Oxford, U.K. (1991) p.219-224

Noymer, P.D.: "Heat transfer by particle convection at the wall of a CFB", Ph.D. Thesis, Massachusetts Institute of Technology, Cambridge MA (1997)

Perry, A.E.: *Hot-wire Anemometry*, Oxford University Press, New York, 1982

Renganathan, K., Turton, R., Clark, N.N.: "Accelerating motion of geometric and spherical particles in a fluid", Powder Technology, **59** (Aug. 1989) p.279-284

Rhodes, M., Zhou, S., Hirama, T., Cheng, H.: "Effects of operating conditions on longitudinal solids mixing in a circulating fluidized bed riser", AIChE J., **37** (1991) p.1450

Rhodes, M., Mineo, H., Hirama, T.: "Particle motion at the wall of a circulating fluidized bed", Powder Technology, **70** (1992) p.207-214

Sekthira, A., Lee, Y.Y., Genetti, W.E.: "Heat transfer in a circulating fluidized bed", Presented at the 25th National Heat Transfer Conference, Houston, Texas (1998).

Soong, C.H., Tuzla, K., Chen, J.C.: "Identification of particle clusters in a circulating fluidized bed", Circulating Fluidized Bed Technology IV, Avidan, A.A. (ed.), AIChE 1994 p. 726

Tsuji, Y., Morikawa, Y., Shiomi, H.: "LDV measurements of an air-solid two-phase flow in a vertical pipe", JFM, **139** (1984) p.417

Wirth, K.E., Seiter, M.: "Solids concentration and solids velocity in the wall region of circulating fluidized beds", Proceedings 11th International Conference on Fluidized Bed Combustion, Anthony, E.J. (ed.) ASME, New York, 1 (1991) p. 311-316

Wirth, K.E., Seiter, M., Molerus, O.: "Concentration and velocities of solids in areas close to the walls in circulating fluidized bed systems", VGB Kraftwerkstechnik, **10** (1991) p.824-828

Wu, R.L., Lim, C.J., Grace, J.R.: "The measurement of instantaneous local heat transfer coefficients in a circulating fluidized bed", The Canadian Journal of Chemical Engineering, **67** (1989**a**) p.301

Wu, R.L., Grace, J.R., Lim, C.J., Brereton, C.M.H.: "Suspension-to-surface heat transfer in a CFB combustor", AIChE Journal, **35** (1989**b**) p.1685

Wu, R.L., Lim, C.J., Grace, J.R., Brereton, C.M.H.: "Instantaneous local heat transfer and hydrodynamics in a circulating fluidized bed", Int. J. Heat Mass Transfer, **34**, (1991) p.2019-2027

Yates, J.G.: "Effects of temperature and pressure on gas-solid fluidization", Chem. Eng. Sci., **51** (1996) p.167